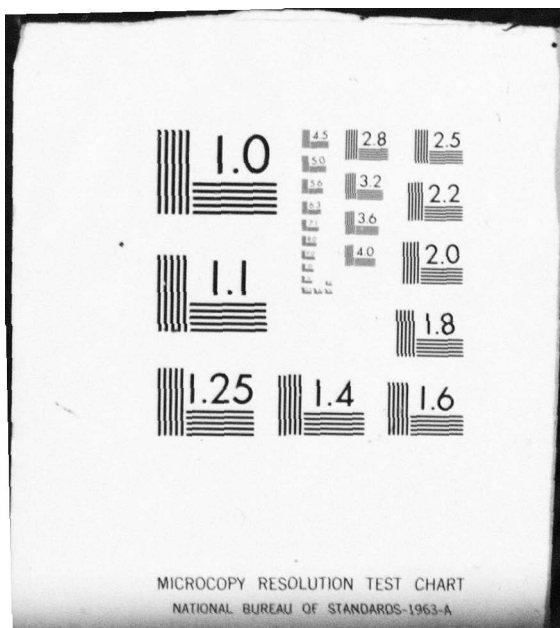


AD-A083 766 GENERAL MOTORS CORP INDIANAPOLIS IN DETROIT DIESEL A--ETC F/G 20/4  
TIME-VARIANT AERODYNAMICS FOR TORSIONAL MOTION OF LARGE-TURNING--ETC(U)  
JAN 80 R L JAY, M D ROTHROCK, R E RIFFEL N00019-79-C-0087  
UNCLASSIFIED DDA-EDR-10192 NL

1 OF 2  
AD  
A083 766





AD A 083766

DDA EDR 10192

12  
b.s.

LEVEL II

# TIME-VARIANT AERODYNAMICS FOR TORSIONAL MOTION OF LARGE-TURNING AIRFOILS

R. L. Jay  
M. D. Rothrock  
R. E. Riffel  
G. T. Sinnet  
Detroit Diesel Allison Division  
General Motors Corporation  
Indianapolis, Indiana 46206

DTIC  
ELECTED  
S D  
APR 29 1980  
E

January 1980

Final Report

Prepared for  
DEPARTMENT OF THE NAVY  
NAVAL AIR SYSTEMS COMMAND  
Washington, D. C. 20361

DDC FILE COPY

APPROVED FOR PUBLIC RELEASE:  
DISTRIBUTION UNLIMITED

80 428 094

## UNCLASSIFIED

SECURITY CLASSIFICATION OF THIS PAGE (When Data Entered)

REPORT DOCUMENTATION PAGE		READ INSTRUCTIONS BEFORE COMPLETING FORM
1. REPORT NUMBER	2. GOVT ACCESSION NO.	3. RECIPIENT'S CATALOG NUMBER
AD-A083 766		
4. TITLE (and Subtitle)	5. TYPE OF REPORT & PERIOD COVERED	
(6) Time-Variant Aerodynamics for Torsional Motion of Large-Turning Airfoils.	(9) Final Report	
7. AUTHOR(s)	10) R. L. Jay M. D. Rothrock R. E. Riffel G. T. Slinet	14) DDA-EDR-10192
8. PERFORMING ORGANIZATION NAME AND ADDRESS	15) N00019-79-C-0087 N	
Detroit Diesel Allison Division of General Motors Corporation Indianapolis, Indiana 46206	10) 1092	
11. CONTROLLING OFFICE NAME AND ADDRESS	12) REPORT DATE	
Department of the Navy Naval Air Systems Command Washington, D.C. 20361	11) January 1980	
13. NUMBER OF PAGES	113	
14. MONITORING AGENCY NAME & ADDRESS (if different from Controlling Office)	15. SECURITY CLASS. (at this report)	
	Unclassified	
16. DISTRIBUTION STATEMENT (of this Report)	15a. DECLASSIFICATION/DOWNGRADING SCHEDULE	
	019200	
APPROVED FOR PUBLIC RELEASE DISTRIBUTION UNLIMITED		
17. DISTRIBUTION STATEMENT (of the abstract entered in Block 20, if different from Report)		
18. SUPPLEMENTARY NOTES		
19. KEY WORDS (Continue on reverse side if necessary and identify by block number)		
Cascades, Unsteady Aerodynamics, Forced Response, Time-Variant Data		
20. ABSTRACT (Continue on reverse side if necessary and identify by block number)		
A cascade of five airfoil sections modelling the hub section of an advanced design turbine featuring a high inlet Mach number and 112 degrees of turning was evaluated at 4 steady-state conditions of varying exit Mach number and expansion ratio. The resulting steady-state airfoil surface pressures were compared to a state-of-the-art analytical prediction.		
(continued)		

UNCLASSIFIED

SECURITY CLASSIFICATION OF THIS PAGE(When Data Entered)

A time-variant investigation was conducted at the 4 operating conditions of the steady-state experiment. Time-variant pressure signals were obtained from a Kulite-instrumented airfoil as the cascade was torsionally oscillated at four values of interblade phase angle per expansion ratio by computer-controlled electromagnetic drive systems. The dynamic pressure signals were evaluated in amplitude and phase lag (referenced to blade motion) and correlated with a state-of-the-art analytical prediction based on a flat-plate cascade.

A quasistatic experiment was performed to relate the dynamic surface pressure amplitudes to those obtained by resetting the cascade to various temporal positions in the torsional cycle of oscillation.

APPROVED FOR PUBLIC RELEASE  
DISTRIBUTION UNLIMITED

UNCLASSIFIED

SECURITY CLASSIFICATION OF THIS PAGE(When Data Entered)

## SUMMARY

A cascade of five airfoil sections modeling the hub section of an advanced-design turbine featuring a high inlet Mach number and over 100 degrees of turning was evaluated in the Detroit Diesel Allison rectilinear turbine cascade facility. The cascade was first investigated at four steady-state conditions of varying exit Mach number and expansion ratio. During this phase, the center airfoil of the cascade was instrumented with static pressure taps to obtain surface pressure distributions. Inlet and exit sidewall taps, exit cone probe surveys, and schlieren flow visualization in the two transonic-exit cases were used to establish cascade periodicity and aerodynamic performance. The resulting steady-state airfoil surface pressures were compared with state-of-the-art analytical predictions.

A quasi-static investigation was made in which the cascade airfoils were reset to various setting angles representing positions in the torsional cycle of 0 degree interblade phase angle cascade oscillation. The static pressure distributions on the center airfoil were again obtained for two expansion ratios for later comparison with dynamic data.

The final phase of the experiment involved replacing the center airfoil of the cascade with one instrumented with flush-mounted Kulite miniature pressure transducers. Electromagnetic drive systems were attached to both trunnions of each bearing-supported airfoil so that the cascade could be oscillated at controlled values of frequency and interblade phase angle. This time-variant cascade was run at the same four operating conditions as the steady-state testing and at four values of interblade phase angle per condition. The pressure signals from the Kulites were recorded on magnetic tape, as was a strain-gage reference signal for later off-line data reduction, using a minicomputer. In this manner, the amplitude and phase angle (referenced to blade motion) were obtained for each pressure transducer.

The dynamic results were compared with an existing analysis. Plots of pressure amplitude and phase lag versus percent chord were constructed, and the quasi-static results were compared with the dynamic data obtained as well.

These data are unique in that they are the first of their kind available for a highly cambered airfoil cascade. The unsteady pressure data point to the conclusion that existing analyses need to be extended to include the effects of airfoil thickness, camber, and loading. Another observation was that a quasi-static calculation does not adequately represent the pressures resulting from physical blade motion at the reduced frequencies of this experiment. Moreover, the primary contribution to the dynamic pressure amplitude on the airfoil is shown to be attributable to the motion of the instrumented airfoil itself and the adjacent airfoils while successive airfoils in the cascade contribute very little.

1st	2nd	3rd	4th	5th
Distribution				
Compatibility Codes				
Avail and/or special				
A				

## TABLE OF CONTENTS

	<u>Page</u>
Summary . . . . .	1
List of Illustrations . . . . .	4
List of Tables . . . . .	6
Introduction . . . . .	7
Discussion . . . . .	9
Experimental Facility . . . . .	9
Airfoil Cascade and Instrumentation . . . . .	12
Torsion Mode Drive System . . . . .	15
Calibration Procedures . . . . .	17
Data Acquisition and Analysis . . . . .	20
Results . . . . .	21
Steady-State Operation . . . . .	21
Quasi-Static Experiment . . . . .	24
Time-Variant Testing . . . . .	27
Correlation of Results . . . . .	34
Conclusions and Recommendations . . . . .	55
References . . . . .	58
Appendix. Time-Variant Data . . . . .	60

PRECEDING PAGE BLANK - NOT FILMED

LIST OF ILLUSTRATIONS

<u>Figure</u>	<u>Title</u>	<u>Page</u>
1	Detroit Diesel Allison rectilinear turbine cascade facility . . . . .	9
2	Schematic of turbine rotor cascade hardware . . . . .	10
3	Photograph of turbine rotor cascade hardware . . . . .	11
4	Airfoil cascade in windows. . . . .	12
5	High-turning turbine rotor hub section. . . . .	14
6	Kulite transducer installation - suction surface. . . . .	15
7	Kulite transducer installation - pressure surface . . . . .	16
8	Torsion drive system bench rig. . . . .	17
9	Torsion drive systems on cascade. . . . .	18
10	Torsion drive system bench rig. . . . .	19
11	Schematic of data acquisition system. . . . .	20
12	Torsion cascade geometry. . . . .	22
13	Schlieren at 2.3 expansion ratio. . . . .	23
14	Schlieren at 2.8 expansion ratio. . . . .	23
15	Steady-state cascade wake survey. . . . .	24
16	Steady-state airfoil surface static pressures for 1.5 expansion ratio . . . . .	25
17	Steady-state airfoil surface static pressures for 1.8 expansion ratio . . . . .	26
18	Steady-state airfoil surface static pressures for 2.3 expansion ratio . . . . .	27
19	Steady-state airfoil surface static pressures for 2.8 expansion ratio . . . . .	28
20	Quasi-static surface pressure distributions for 1.5 expansion ratio . . . . .	30
21	Quasi-static surface pressure distributions for 2.8 expansion ratio . . . . .	31
22	Normalized quasi-static surface pressure differentials for 1.5 expansion ratio . . . . .	32
23	Normalized quasi-static surface pressure differentials for 2.8 expansion ratio . . . . .	34
24	Time-variant surface pressure amplitude plot for 1.5 expansion ratio and 0° interblade phase angle . . . . .	35
25	Time-variant surface pressure amplitude plot for 2.8 expansion ratio and 0° interblade phase angle . . . . .	36
26	Time-variant surface pressure phase lag plot for 1.5 expansion ratio and 0° interblade phase angle . . . . .	37
27	Time-variant surface pressure phase lag plot for 2.8 expansion ratio and 0° interblade phase angle . . . . .	37
28	Correlation of calculated results at 90° phase. . . . .	38
29	Correlation of calculated results at 270° phase . . . . .	38
30	Assumed flat-plate cascades . . . . .	39
31	Description of flat-plate cascades. . . . .	39
32	Normalized pressure coefficients for 0° interblade phase angle . . . . .	40
33	Phase lag for 0° interblade phase angle . . . . .	41
34	Normalized pressure coefficients for -45° interblade phase angle . . . . .	41
35	Phase lag for -45° interblade phase angle . . . . .	42

<u>Figure</u>	<u>Title</u>	<u>Page</u>
36	Normalized pressure coefficients for $-90^\circ$ interblade phase angle . . . . .	43
37	Phase lag for $-90^\circ$ interblade phase angle . . . . .	43
38	Normalized pressure coefficients for $180^\circ$ interblade phase angle . . . . .	44
39	Phase lag for $180^\circ$ interblade phase angle . . . . .	44
40	Normalized pressure coefficients for $90^\circ$ interblade phase angle . . . . .	45
41	Phase lag for $90^\circ$ interblade phase angle . . . . .	46
42	Normalized pressure coefficients for $45^\circ$ interblade phase angle . . . . .	46
43	Phase lag for $45^\circ$ interblade phase angle . . . . .	47
44	Normalized pressure as a function of interblade phase angle at 8% meanline station . . . . .	48
45	Normalized pressure as a function of interblade phase angle at 57.8% meanline station . . . . .	48
46	Normalized pressure as a function of interblade phase angle at 71.2% meanline station . . . . .	49
47	Normalized pressure as a function of interblade phase angle at 88.5% meanline station . . . . .	50
48	Comparison of quasi-static and dynamic data on suction surface, $Re = 1.5$ . . . . .	51
49	Comparison of quasi-static and dynamic data on suction surface, $Re = 2.8$ . . . . .	51
50	Comparison of quasi-static and dynamic data on pressure surface, $Re = 1.5$ . . . . .	52
51	Comparison of quasi-static and dynamic data on pressure surface, $Re = 2.8$ . . . . .	52
52	Time-variant pressure phase lag as a function of interblade phase angle at 8% meanline station . . . . .	53
53	Time-variant pressure phase lag as a function of interblade phase angle at 57.8% meanline station . . . . .	54
54	Time-variant pressure phase lag as a function of interblade phase angle at 71.2% meanline station . . . . .	54
55	Time-variant pressure phase lag as a function of interblade phase angle at 88.5% meanline station . . . . .	55

## LIST OF TABLES

<u>Table</u>	<u>Title</u>	<u>Page</u>
1	Description of turbine airfoil cascade. . . . .	13
2	Pressure measurement locations in terms of percent projected chord . . . . .	14
3	Steady-state operating points . . . . .	22
4	Dynamic data airfoil motion summary . . . . .	29
5	Relative contributions of individual airfoils on surface dynamic pressures . . . . .	33
6	Conditions assumed for analytical study . . . . .	36

## INTRODUCTION

Aerodynamically induced vibration of fan, compressor and turbine airfoils is a commonly encountered problem in the development of gas turbine engines. Vibrations occur when a periodic aerodynamic forcing function has a frequency equal to the natural frequency of a blade. These frequency correspondences are typically plotted on a frequency/speed diagram which relates the natural frequencies of a particular blade and its forcing function frequencies at varying rotor speeds.

Current technology is sufficient to predict with a fair degree of accuracy the natural frequencies of bladed disk systems. The knowledge of the source of various aerodynamic stimuli acting on the airfoils is also well substantiated by experience. However, these tools are used only to locate, in terms of rotor speed, the resonant points on a frequency/speed diagram. Design rules are used typically to determine if a particular intersection will be detrimental to engine operation. At present, the actual values of the resonant stresses are unknown until the first testing of the assembled rig or engine. If stresses in excess of a predetermined allowable value are measured, then life requirements dictate that such stresses must be reduced. This reduction can be effected by altering frequencies, changing the magnitude of the forcing function, increasing allowables for the airfoil, and other demonstrated techniques. Systematic as this procedure may seem, it still requires that test iteration be performed until design goals are met. Hence, a predictive methodology for determining the stress levels of a blade in resonance with an aerodynamic forcing function is needed.

The predictive model would include a description of the pressure distribution created by the disturbance being swept past an assumed nonresponding airfoil and of the pressure distribution created by the movement of the airfoil in the aerodynamic field. The first of these effects has been labeled the "gust" loading, the second termed the "aerodynamic damping." An iterative solution which relates the gust loading, the ensuing blade motion, and the generated aerodynamic damping is necessary to properly predict the total response of a particular airfoil.

The aerodynamic "gust" problem has been analyzed by several investigators. Kemp and Sears<sup>(1)\*</sup>, Horlock<sup>(2)</sup>, Naumann and Yeh<sup>(3)</sup>, and Goldstein and Atassi<sup>(4)</sup> considered isolated airfoils acted on by various input gust profiles to determine unsteady or time-variant loadings of the airfoils. These investigators contributed to the overall understanding of the gust problem, yet the results were not amenable for application to turbomachinery blading rows.

D. S. Whitehead<sup>(5)</sup> analyzed a cascade of flat-plate airfoils subjected to a wake resulting from periodic obstructions far upstream and presented the induced gust loading as functions of cascade variables for incompressible flow. Smith<sup>(6)</sup> extended this analysis to include the effects of compres-

\*Numbers in parentheses correspond to references listed at end of this report.

sibility in the subsonic flow regime. Henderson and Daneshyar<sup>(7)</sup> used thin airfoil theory to derive an expression for the unsteady lift acting on a two-dimensional cascade of thin, slightly cambered airfoils moving through a sinusoidal disturbance in an incompressible velocity field. In a later analysis, Henderson and Horlock<sup>(8)</sup> analytically investigated a moving cascade of airfoils experiencing a sinusoidal disturbance in inlet axial velocity. Two-dimensional, inviscid, and incompressible flow was assumed for highly cambered, small-lift-coefficient blading. The purpose of these analyses was to describe analytically the time-variant loading of an airfoil attributable to wake-type disturbances.

Because of the limiting assumptions in these and other analyses, experimental data to validate results and indicate needed improvements in the analytical models were needed. Such investigators as Commerford and Carta<sup>(9)</sup>, Ostdiek<sup>(10)</sup>, Henderson and Franke<sup>(11)</sup>, and Fleeter, Novick, and Riffel<sup>(12)</sup> furnished sets of initial correlative data. More recently, Fleeter, Bennett, and Jay<sup>(13, 14, 15, 16)</sup> have provided measurements of rotor wake-induced time-variant surface pressures on a highly cambered stator vane. The pressures were related to the strength of the incoming velocity defect typifying the rotor wake. Variations of parameters including reduced frequency, solidity, axial spacing, and interblade phase angle have provided an extensive data bank for correlation of gust analyses in the subsonic flow regime.

The aerodynamic damping portion of the overall forced vibration problem has been analytically investigated by several of those mentioned previously. Because the aerodynamic damping analyses are necessary to predict flutter, this area of research has been vigorously attacked. Whitehead<sup>(5)</sup>, Smith<sup>(6)</sup>, and Fleeter<sup>(17)</sup> are but a few of those who have presented analyses for the subsonic flow regime. The common assumption in many of these analyses has been that of a zero-thickness flat plate. Atassi and Akai<sup>(18)</sup> presented an analytical formulation for analyzing oscillating airfoils in cascade in uniform incompressible flows. The theory accounts for the geometry of the airfoils. Experimentally, the efforts of Carta and St. Hilaire<sup>(19)</sup> and Fleeter and Riffel<sup>(20)</sup> in two-dimensional, rectilinear wind tunnels have furnished basic experimental damping for correlations in the low subsonic and supersonic flow regimes.

Platzer<sup>(21)</sup> presented a review of unsteady flows in turbomachinery which included the efforts of investigators in the areas of both gust response and aerodynamic damping. This survey was concluded with an emphasis on the need for evaluation of the various analytical formulations by comparison with experimental data, specifically in the area of highly loaded, transonic cascades.

The purpose of the experimental research program described in this report was to furnish basic time-variant data acquired from controlled torsional oscillations of a cascade of highly cambered airfoils operating transonically. The results of varying operating conditions and interblade phase angles on the measured time-variant surface pressures are presented. Pressures measured during quasi-static motion and dynamic motion of the airfoils are compared, and a complete set of steady-state data regarding the operation of the cascaded airfoils is presented for analyses requiring steady field descriptions. The time-variant and steady-state data are compared with existing analyses. The results and conclusions derived from this investigation are presented along with a list of recommendations.

## DISCUSSION

### EXPERIMENTAL FACILITY

The Detroit Diesel Allison (DDA) rectilinear turbine cascade facility (Figure 1) was conceived and built as a research tool to evaluate the steady and time-variant aerodynamic characteristics of turbine blade sections having high turning. The facility is a continuous-flow, nonreturn, pressure-vacuum-type wind tunnel; the test section is evacuated by two primary steam ejectors. Up to 10 lbm/sec of filtered, dried, and temperature-controlled air can be used.

The major features of this facility include the following:

- o Continuous operation for extended time periods
- o A mechanized test section for changing cascade incidence angle
- o A schlieren optical system for visual observation and photography of the facility in both steady and unsteady operation
- o Bleed systems on all four cascade inlet sidewalls
- o A sophisticated instrumentation system centered around two digital mini-computers

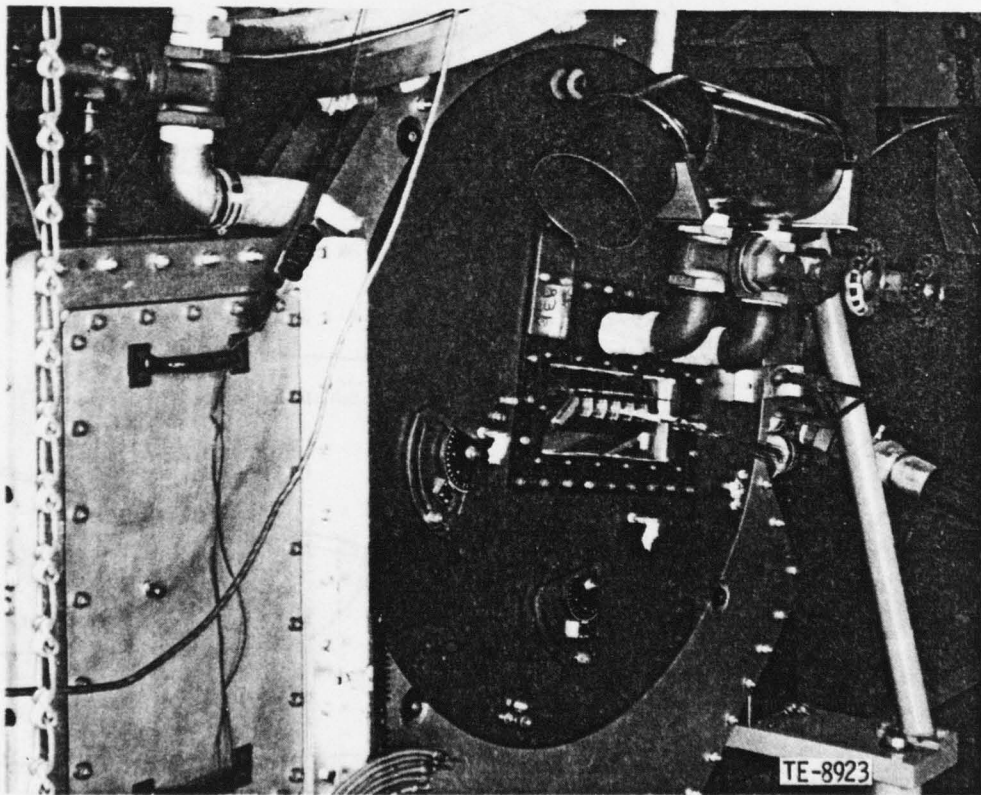


Figure 1. Detroit Diesel Allison rectilinear turbine cascade facility.

In the cascade facility, the entrance flow to the test section is generated by parallel nozzle blocks (Figures 2 and 3) which set the inlet flow direction. The upper nozzle block is movable to ensure that all the flow is directed through the cascade. The cascade inlet Mach number is determined by the cascade geometry under test.

To aid in the establishment of the cascade inlet periodicity, bleed chambers are provided in the upper and lower nozzle blocks. Adjustment of the bleed rate through these chambers allows the inlet flow field to the cascade to be affected.

Active cascade-inlet sidewall boundary-layer control capability to ensure the two-dimensionality of the cascade flow field is effected by the use of suction strips in the cascade sidewalls. Two bleed-hose connections on each

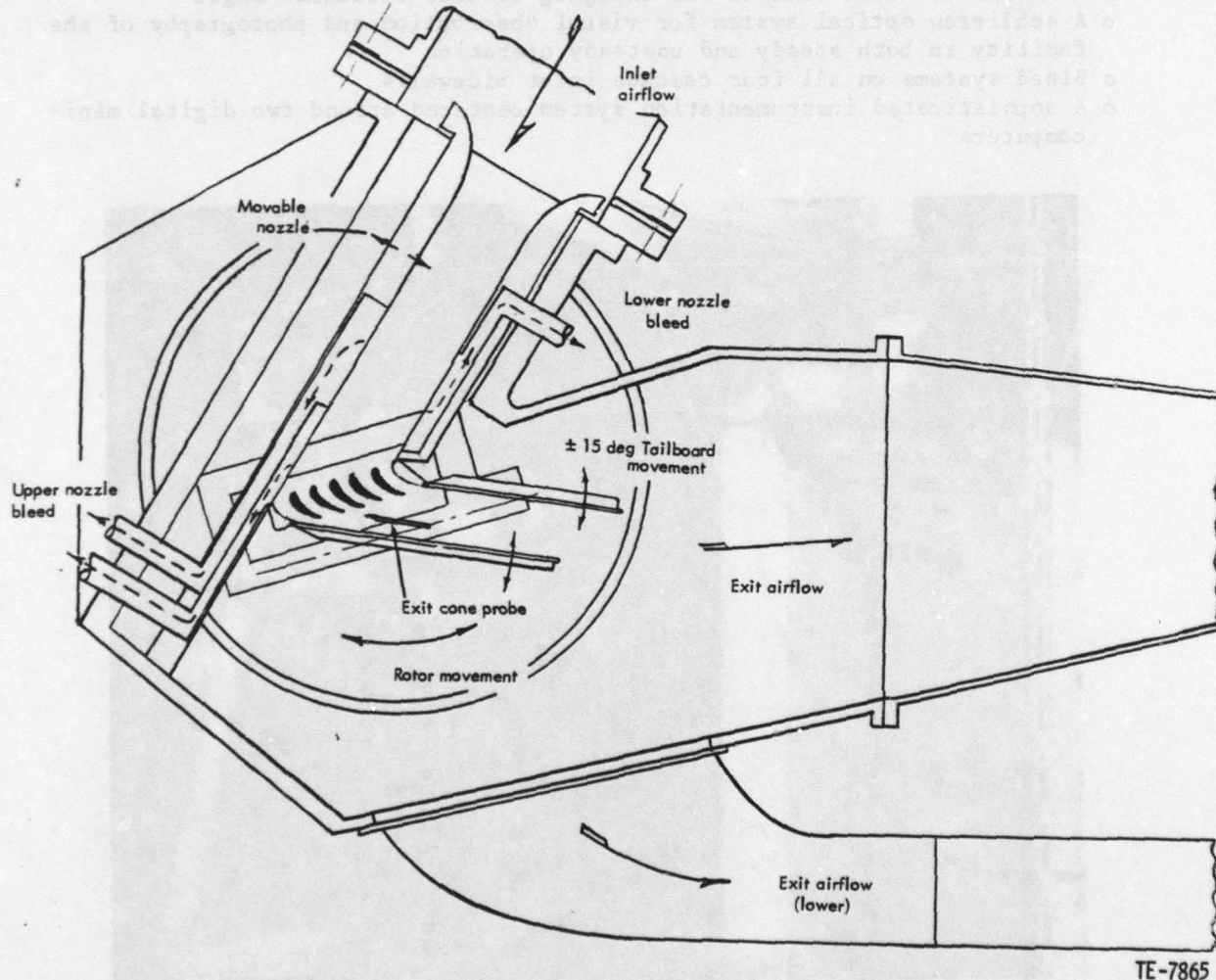


Figure 2. Schematic of turbine rotor cascade hardware.

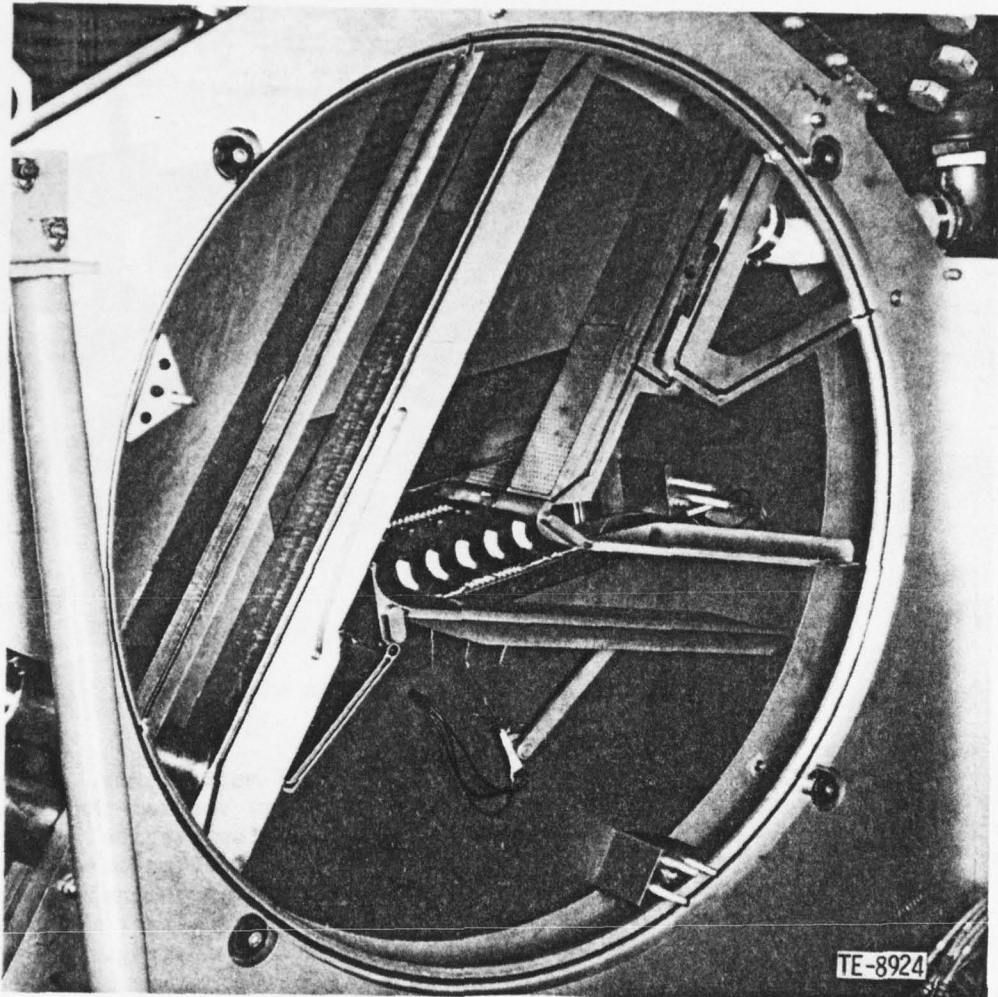


Figure 3. Photograph of turbine rotor cascade hardware.

strip with separately variable valves provide appropriate bleed flows to the front and rear portions of the sidewall. A third, smaller steam ejector is used to evacuate all of the bleed systems used.

The cascade has dummy end blades presenting one surface to the flow, as shown in Figures 3 and 4. The front dummy blade slides along the movable upper nozzle block as the incidence angle is changed. Adjustable porous tailboards are hinged on the aft ends of the dummy blades, serving to set expansion ratio and exit periodicity. The porous tailboards generate a bleed effect because of the lower exit plenum pressure on their outside surfaces. This bleed prevents shock wave reflections back into the cascade during transonic exit operation.

To acquire the steady-state and dynamic data from this facility requires the use of a minicomputer interfaced to both a Scanivalve pressure cabinet and

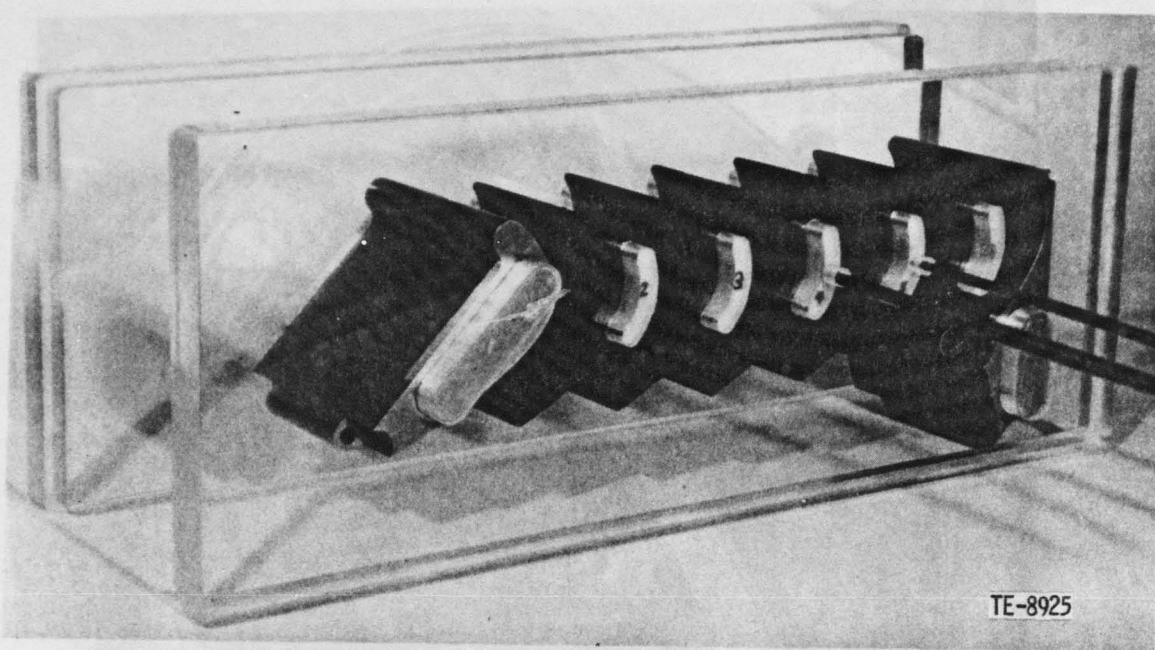


Figure 4. Airfoil cascade in windows.

crossbar scanner and a high-speed analog-to-digital multiplexer. A smaller minicomputer is used in conjunction with the first to control the oscillatory motion of the cascade blades under dynamic test by precisely switching the d-c power supplies which energize the drive system electromagnets. Other facility equipment includes racks of amplifiers and signal conditioners for strain gages and pressure transducers and a 14-channel magnetic tape recorder. This equipment is used for the time-variant testing.

#### AIRFOIL CASCADE AND INSTRUMENTATION

The two-dimensional cascade used in this investigation comprises five airfoils that have the profile of a high-turning turbine rotor hub section, as shown in Figure 5. Trunnions were attached to both ends of each airfoil for support in the cascade sidewalls. The physical dimensions of the airfoils are a 3.00-in. span, a 2.59-in. chord, a maximum thickness of 0.53 in., and 112° of turning. The cascade physical parameters and the manufacturing coordinates are listed in Table 1.

The cascade airfoils consist of injection-molded fiberglass with a Kevlar outer wrap. Steel trunnions were attached to both ends of each airfoil with screw clamps and pins. These trunnions were supported in bearings, and the airfoil setting angle was maintained by the clamps of the cascade drive system. Paths for the instrumentation wires and pressure tubes were machined into the blade surface, and the trunnions of the instrumented blades were hollow to allow the wires and tubes to exit the cascade.

TABLE 1. DESCRIPTION OF TURBINE AIRFOIL CASCADE.

Physical Parameters

Chord	2.59 in.
Solidity	1.891
Setting Angle	25.5 deg
Maximum Thickness/Chord	0.205
Leading Edge Radius/Chord	0.024
Trailing Edge Radius/Chord	0.009
Axial Chord Projection	2.34 in.
Torsion Axis Location	35.5% (From L.E.)

Manufacturing Coordinates

Leading Radius  
0.06323

Trailing Radius  
0.02371

Station	x	y	Station	x	y
1	-0.8429	0.5398	31	1.7245	0.5398
2	-0.7226	0.5671	32	1.7147	0.5206
3	-0.6766	0.4820	33	1.6137	0.4486
4	-0.6218	0.4024	34	1.5116	0.3780
5	-0.5483	0.3241	35	1.4086	0.3090
6	-0.4861	0.2652	36	1.3045	0.2414
7	-0.4070	0.2097	37	1.1995	0.1754
8	-0.3220	0.1637	38	1.0935	0.1109
9	-0.2326	0.1268	39	0.9865	0.0480
10	-0.1401	0.0987	40	0.8786	-0.0132
11	-0.0456	0.0785	41	0.7697	-0.0727
12	0.0502	0.0654	42	0.6600	-0.1306
13	0.1467	0.0590	43	0.5492	-0.1864
14	0.2434	0.0583	44	0.4371	-0.2397
15	0.3400	0.0631	45	0.3234	-0.2893
16	0.4362	0.0727	46	0.2074	-0.3334
17	0.5319	0.0868	47	0.0889	-0.3698
18	0.6268	0.1051	48	-0.0324	-0.3956
19	0.7210	0.1272	49	-0.1559	-0.4075
20	0.8142	0.1530	50	-0.2797	-0.4018
21	0.9064	0.1820	51	-0.4007	-0.3754
22	0.9976	0.2142	52	-0.5145	-0.3264
23	1.0878	0.2492	53	-0.6159	-0.2553
24	1.1768	0.2869	54	-0.7007	-0.1650
25	1.2648	0.3272	55	-0.7663	-0.0599
26	1.3516	0.3697	56	-0.8124	0.0551
27	1.4374	0.4144	57	-0.8404	0.1759
28	1.5220	0.4611	58	-0.8528	0.2992
29	1.6057	0.5097	59	-0.8524	0.4233
30	1.6883	0.5599	60	-0.8425	0.5469

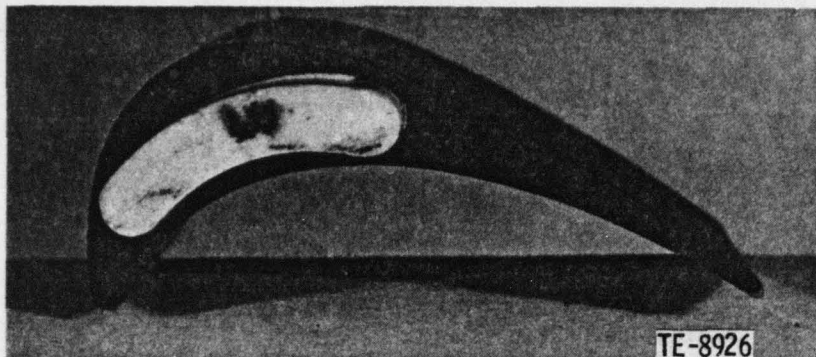


Figure 5. High-turning turbine rotor hub section.

The instrumentation used to describe the steady-state aerodynamic performance of the cascade included sidewall static pressure taps at the inlet and exit, upstream total pressure and temperature probes, and a five-hole conical probe to survey the exit. Schlieren flow visualization was also used to help establish exit periodicity in the transonic cases.

For the steady-state and quasi-static testing, the center blade of the cascade was instrumented with nine static pressure taps per surface for definition of the surface pressure distributions at each operating condition. For the time-variant phase of the experiment, the center blade of the cascade was instrumented with 12 miniature high-response Kulite pressure transducers. These Kulites were staggered across the center 50% span of the airfoil, five on the pressure surface and seven on the suction surface. The locations of the static pressure taps and Kulite dynamic pressure transducers are given in Table 2.

TABLE 2. PRESSURE MEASUREMENT LOCATIONS IN TERMS OF PERCENT PROJECTED CHORD.

Pressure surface		Suction surface	
Static taps	Kulites	Static taps	Kulites
1.3	10	5	5
5	30	10	15
10	60	20	30
20	75	30	55
30	90	45	70
45		60	80
60		70	92.5
80		80	
95		90	

A new installation technique was used on the airfoil of this test to reduce the perpendicular acceleration sensitivity of the Kulite pressure transducers. Each transducer is embedded in the airfoil under a perforated metal screen made flush with the airfoil surface, as shown in Figures 6 and 7. This technique has an advantage over the previous method (in which an

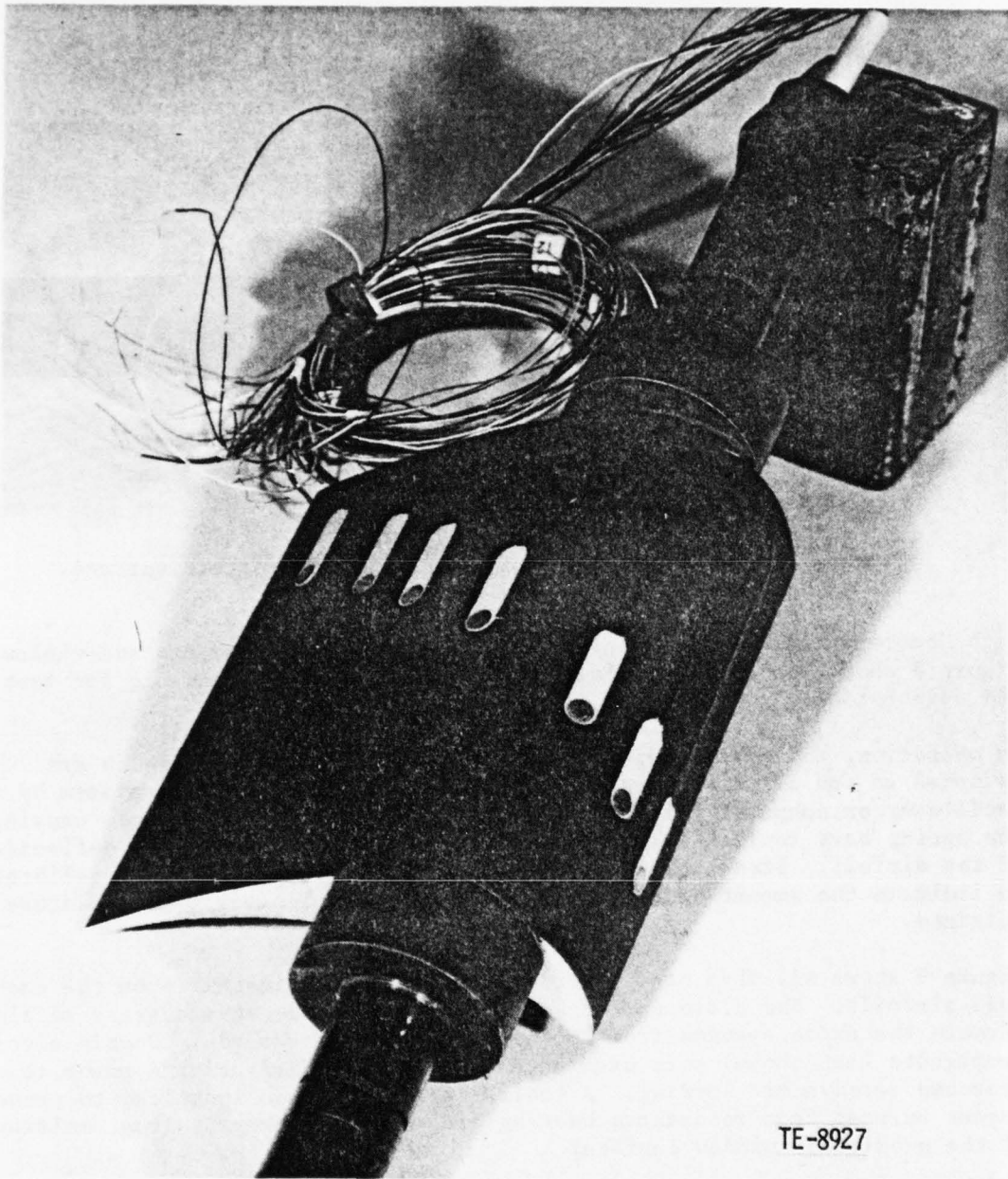


Figure 6. Kulite transducer installation - suction surface.

RTV coating contacted the transducer diaphragm directly) because there is no increase in the effective mass of the diaphragm.

#### TORSION MODE DRIVE SYSTEM

The torsion mode drive system is a spring bar and hammer arrangement with a driving electromagnet. Each airfoil is driven on both ends to ensure rigid-body motion with no spanwise twisting or bending. The trunnions are held

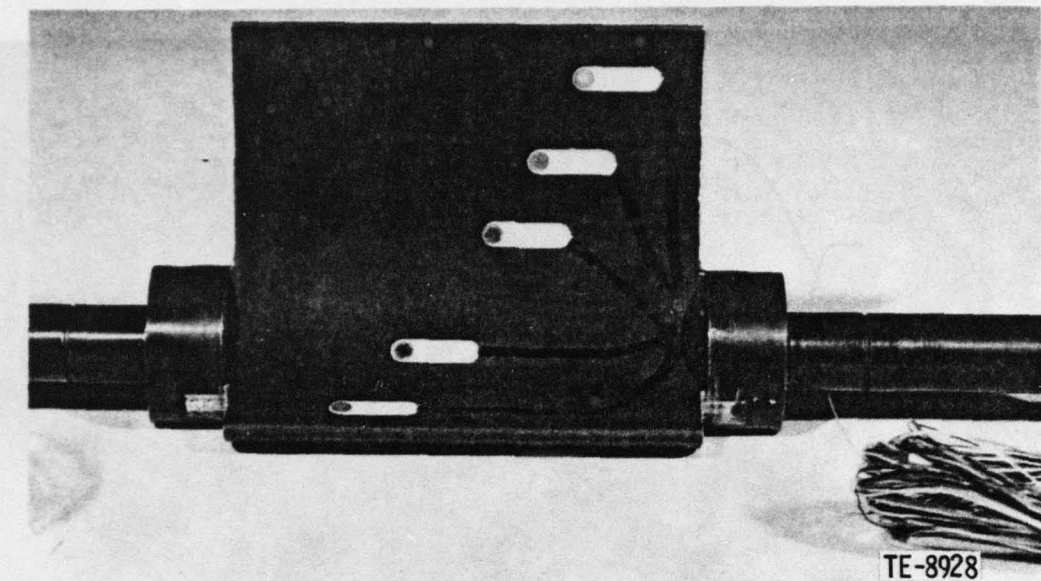


Figure 7. Kulite transducer installation - pressure surface.

with "battery clamps" and are supported by bearings in the cascade windows. Figure 8 shows the torsion drive system assembled on a bench rig for test and calibration.

In operation, the electromagnets are powered by d-c supplies which are switched on and off at the resonant frequency of the torsional system by an oscillator or computer trigger. The hammers swing through an arc, causing the spring bars to flex which results in corresponding torsional deflection of the airfoil. Strain gages are attached to each spring bar and calibrated to indicate the amount of deflection, so that airfoil torsional amplitude is obtained.

Figure 9 shows all five of the torsion drive systems installed on the cascade airfoils. The close spacing of the airfoils made it necessary to alternate the drive systems from top to bottom of the cascade. Double electromagnets (not shown) were used on each side for added driving power to overcome aerodynamic loading. A cooling air system was installed to prevent magnet burnout from resistance heating and, also, to prevent local melting of the plexiglass window surface.

Each of the five drive systems was tuned to a resonant frequency of 345 Hz by small changes in hammer mass and/or spring bar length. Peak amplitudes were obtained for each blade by adjusting the magnet-to-hammer air gap and the d-c power supply voltage. A minicomputer was used to coordinate the switching of the five power supplies so that the desired interblade phase angle could be obtained for each setpoint. Precisely phased square-wave pulse trains were continuously produced by the computer to perform this task in response to keyboard requests for specific phase angles between blades.

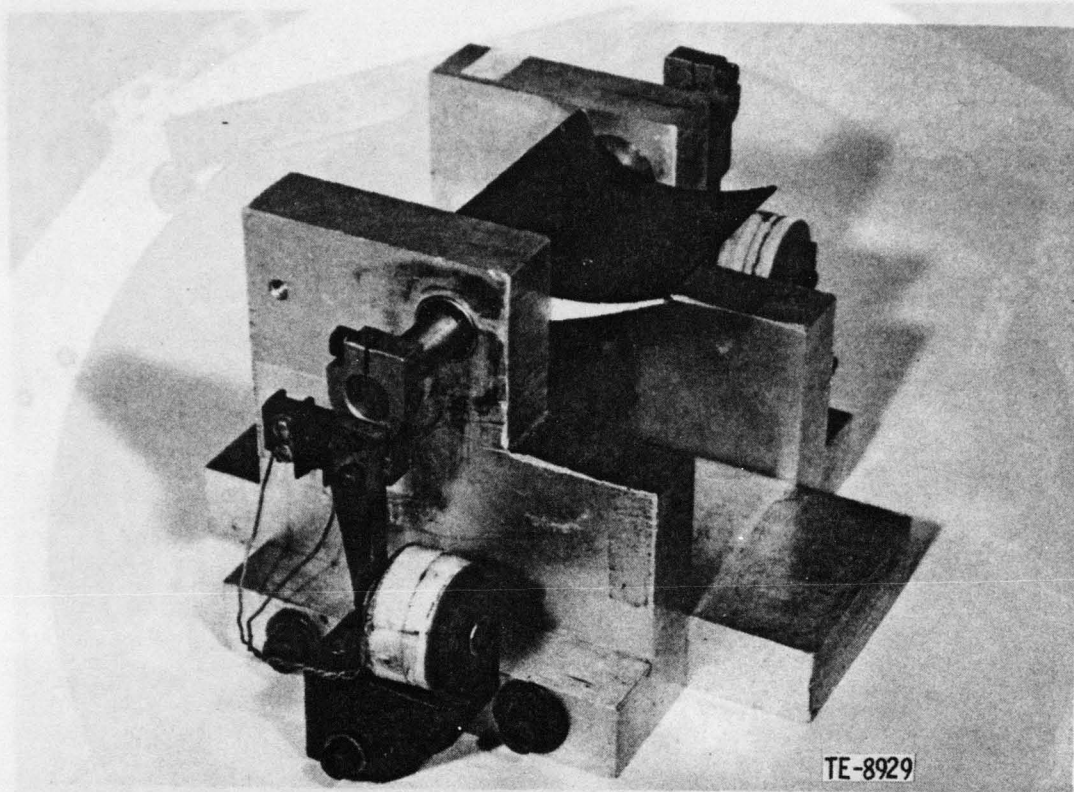


Figure 8. Torsion drive system bench rig.

#### CALIBRATION PROCEDURES

Calibrations were performed before the time-variant data were acquired so that the transfer functions throughout the measurement system could be determined. Included in these calibration measurements were strain gage dynamic sensitivities, Kulite static sensitivities, Kulite amplitude and phase shift components due to oscillation, amplifier and signal conditioner gains and phase shifts, and phase shifts between channels of the magnetic tape recorder.

For the calibration of the strain gages on the spring bars, the torsion drive system bench rig shown in Figure 10 was used. The system was first tuned to the desired frequency with a specific pair of spring bars, and then the amplitude of the strain gage signal was read by the minicomputer. The amplitude of the blade motion was obtained by using a dial indicator and height gage to measure the difference between the upward peak height of the trailing edge and its at-rest position. The difference between the downward peak height and at-rest was similarly obtained. The linear motion at the trailing edge was thus the sum of these measurements, which was converted to torsional amplitude by using the length of the blade from axis to trailing edge. This procedure was repeated for several amplitudes, resulting in a linear plot of voltage versus torsional amplitude. The slope is the

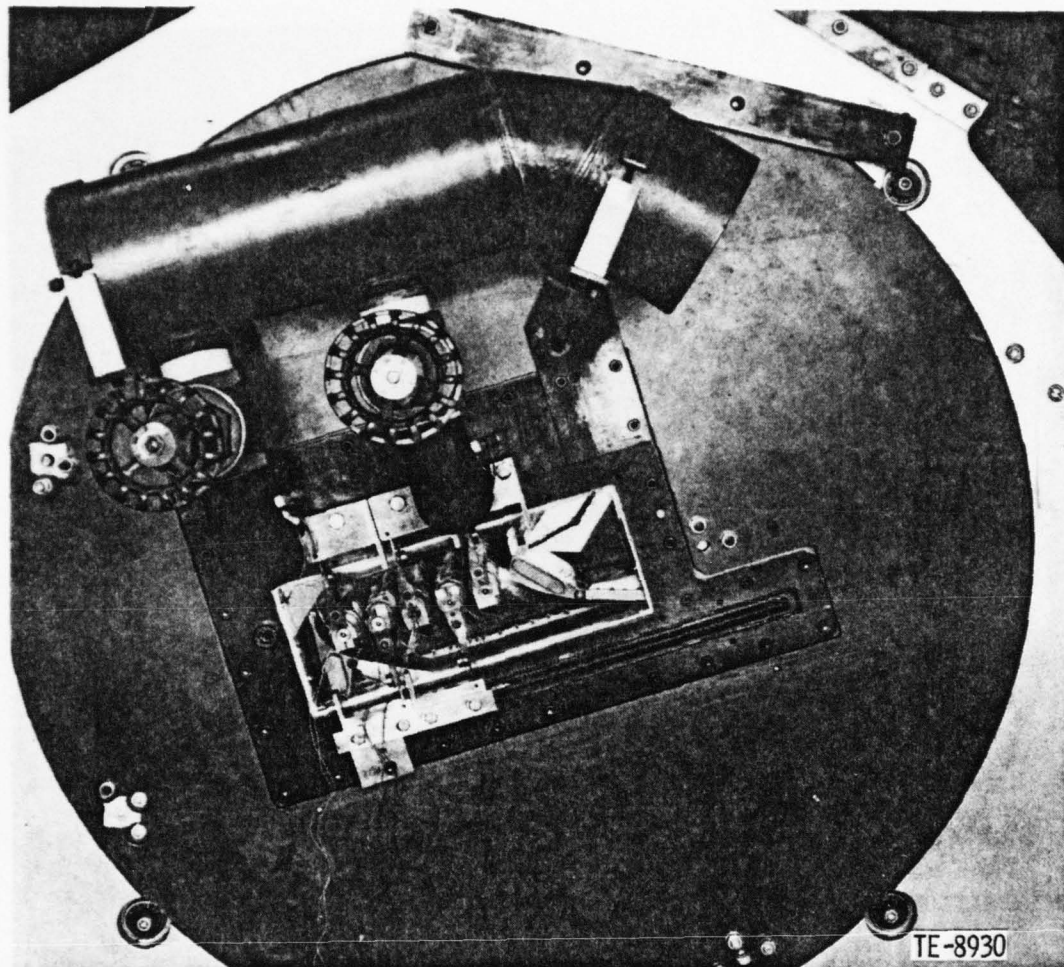


Figure 9. Torsion drive systems on cascade.

sensitivity expressed in  $\text{mV/V/radian}$  when the bridge voltage is divided out. The sensitivity of each pair of spring bars was calibrated in this fashion.

The Kulite pressure transducer static sensitivities were obtained with a vacuum-jar calibration rig. A quartz manometer-controller was used to evacuate the jar containing the Kulite-instrumented blade to the desired pressure. The d-c voltage output of each Kulite was measured over a range of pressures, resulting in plots of voltage versus pressure. The sensitivities in  $\text{mV/psi}$  were the slopes of these linear plots. These sensitivities compared closely with manufacturer-supplied data.

A Kulite pressure transducer mounted on an oscillating airfoil is subjected to forces resulting from acceleration of the transducer diaphragm and strain transmitted to the transducer through its mounting as well as to forces from the pressure to be measured. To determine the acceleration/strain contribution to the Kulite signal, the instrumented blade was oscillated in the bench

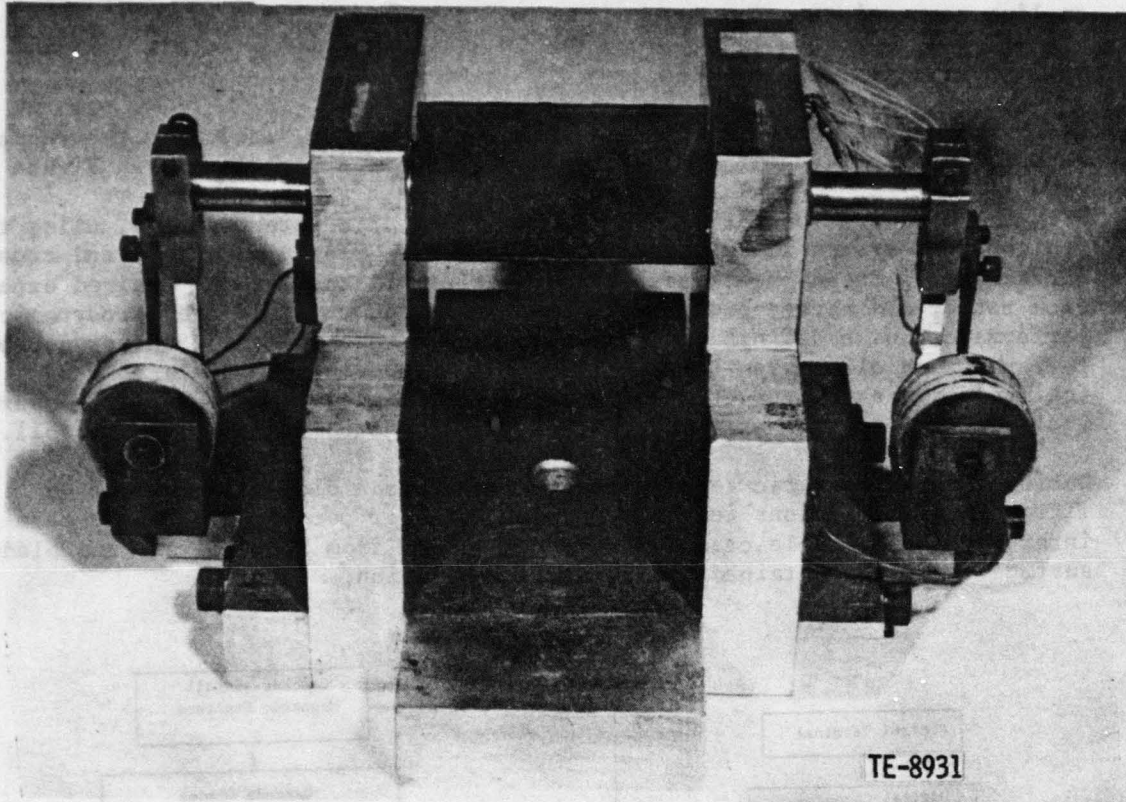


Figure 10. Torsion drive system bench rig.

rig in a vacuum. Under these conditions, no pressure-induced signal was present. The remaining signal was therefore the result of acceleration/strain effects alone. The minicomputer was used to measure the amplitude and phase shift of each Kulite signal over a range of torsional blade amplitudes. The data plots of signal versus torsional amplitude were linear. A calibration of acceleration effects was thus obtained and stored in the computer data analysis program to allow corrections to the final data. These effects were less than 5% of a typical pressure measured during time-variant testing.

The new transducer mounting technique used for this cascade instrumented airfoil featured a perforated metal screen cover over each transducer, made flush with the airfoil surface as shown in Figures 6 and 7. This method demonstrated an acceleration sensitivity of approximately half that obtained with the RTV diaphragm coating previously used for cascade airfoils.

The dynamic response of the blade-mounted Kulites to an oscillating pressure was not obtained. Experience with mounted Kulites has shown that the dynamic characteristics of the Kulites are sufficient for measurements at the frequency used in this testing.

To complete the calibration for the experiment, the gains and phase shifts of all the other electronics were determined and stored in the computer for on-line corrections.

## DATA ACQUISITION AND ANALYSIS

The primary components of the data acquisition system, including the equipment for on-line and off-line analysis, are shown schematically in Figure 11.

With the tunnel in operation, the steady-state data were measured, using the minicomputer system interfaced with a Scanivalve pressure cabinet and cross-bar scanner. Steady-state periodicity was established at the desired expansion ratio, and a cone-probe exit survey was made to yield the aerodynamic performance, wake definition, and mass-averaged properties. Schlieren photographs were also taken at the transonic exit operating points to show trailing edge shock structures. The computer listed each measured pressure, including the surface static pressures of the instrumented center airfoil.

During the quasi-static testing phase, the cascade blades were reset to fixed angular positions in the torsional cycle of oscillation of the zero interblade phase angle case. Steady-state data from the sidewall and blade surface taps were obtained for each reset position.

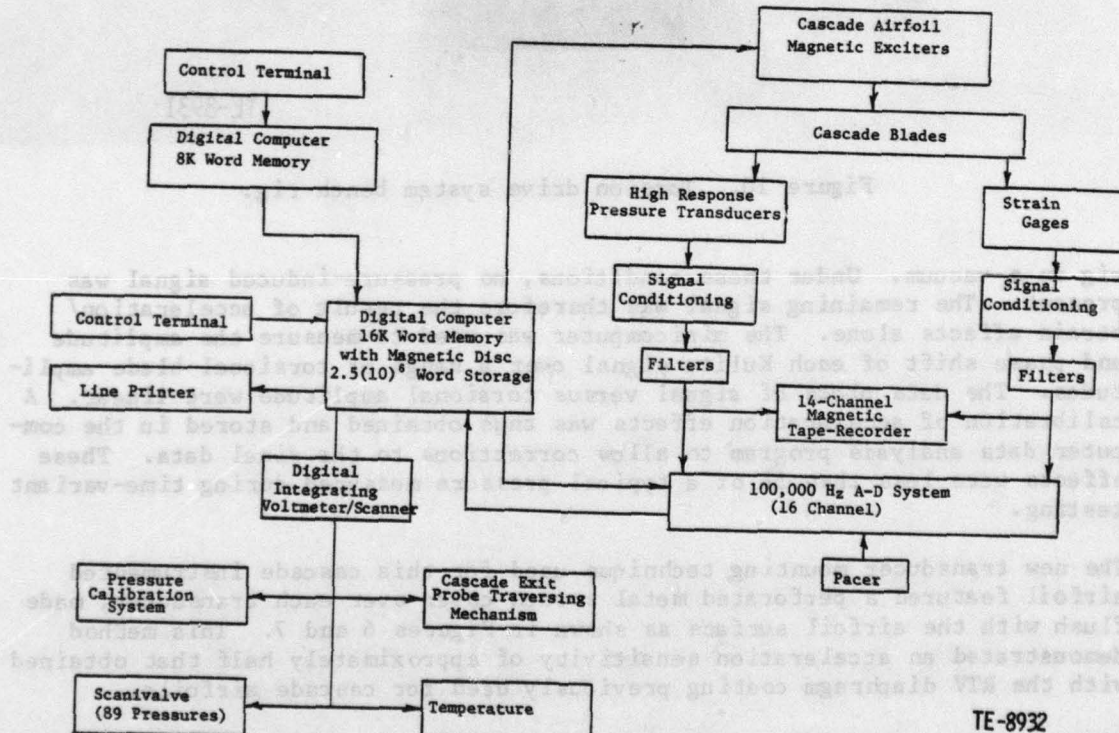


Figure 11. Schematic of data acquisition system.

For the time-variant phase of the experiment, the center blade was instrumented with Kulite high-response miniature pressure transducers. The torsion drive systems were tuned to equal resonant frequencies and maximum amplitudes. An operating condition described by steady-state data was established, and the cascade was then driven at the desired interblade phase angle with the smaller minicomputer. Minor adjustments to the phase were made via the d-c power supply voltage controls. The minicomputer, interfaced to the high-speed analog-to-digital multiplexer, acquired, averaged, and printed out the amplitudes and phase angles of each blade (referenced to the center blade signal) as adjustments in the interblade phase angles were made.

After the desired interblade phase angle was established, the signals from the Kulite pressure transducers were recorded on the magnetic tape recorder with a center-blade strain gage signal for phase reference. This procedure was repeated for six values of cascade interblade phase angle at each of four expansion ratios.

The recorded Kulite signals were analyzed off-line with the aid of the analog-to-digital multiplexer and the minicomputer. An averaging technique was used to establish raw signals. These signals were then corrected as described by calibration information. Pressure amplitude and phase angles were thus obtained for each Kulite in the data set.

The autocorrelation and cross-correlation procedures used in the analysis are described in Reference 20. In the averaging technique, the reference blade square wave driving signal acts as a trigger. Six cycles of oscillation are acquired for each desired signal to represent one coherently triggered sample. One hundred samples are collected and averaged, thus providing an enhanced signal for analysis. This data enhancement technique is similar to that described in Reference 13; the only difference is in the trigger source.

## RESULTS

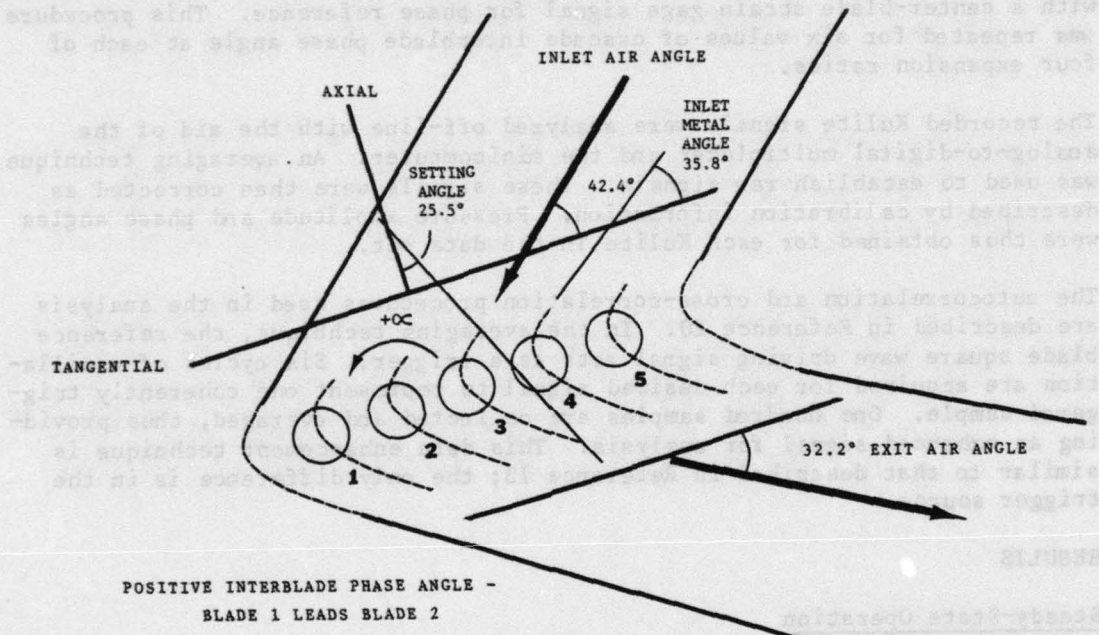
### Steady-State Operation

The steady-state phase of the experimental research program involved the selection of four cascade operating points at a single value of incidence angle so that the inlet Mach number was nearly constant. The cascade inlet static pressure was adjusted to slightly below ambient to reduce the load on the cascade sidewalls and trunnion seals. The inlet temperature was controlled to 100°F. A range of expansion ratios was then run by adjusting the exit tailboards and exit air valve so that two operating conditions of subsonic exit Mach number and two of transonic exit Mach number were investigated. Inlet and exit periodicity, as determined by sidewall static pressure taps and schlieren flow visualization, was closely maintained. A summary of the cascade operating points is presented in Table 3.

The turbine cascade geometry is depicted schematically in Figure 12, which shows the air and metal angles and the airfoil numbering system. Figures 13 and 14 are schlieren photographs from the viewpoint of Figure 12 of the two transonic-exit cases at a 2.3 and 2.8 expansion ratio; the trailing-edge

TABLE 3. STEADY-STATE OPERATING POINTS

Ideal inlet total to exit static expansion ratio	Mass-averaged expansion ratio	Inlet Mach number	Inlet static pressure (psia)	Cascade incidence angle (deg)	Mass-averaged exit Mach number
1.5:1	1.53	0.50	12.74	-6.6	0.78
1.8:1	1.84	0.52	12.16	-6.6	0.95
2.3:1	2.34	0.52	12.05	-6.6	1.13
2.8:1	2.71	0.53	12.30	-6.6	1.25



TE-8933

Figure 12. Torsion cascade geometry.

shock structures are visible in both pictures. The periodicity of the exit flow is evidenced by the identical appearance of each shock structure. As the exit Mach number is reduced from 1.25 (Figure 14) to 1.13 (Figure 13), the shock waves impinging on the suction surface of each airfoil are seen to become more nearly normal. The dynamic data at the 2.8 expansion ratio were affected by the presence of this shock wave on the last Kulite pressure transducer on the suction surface. No schlieren photographs were taken at the two lower expansion ratios because the flow was subsonic throughout the cascade.

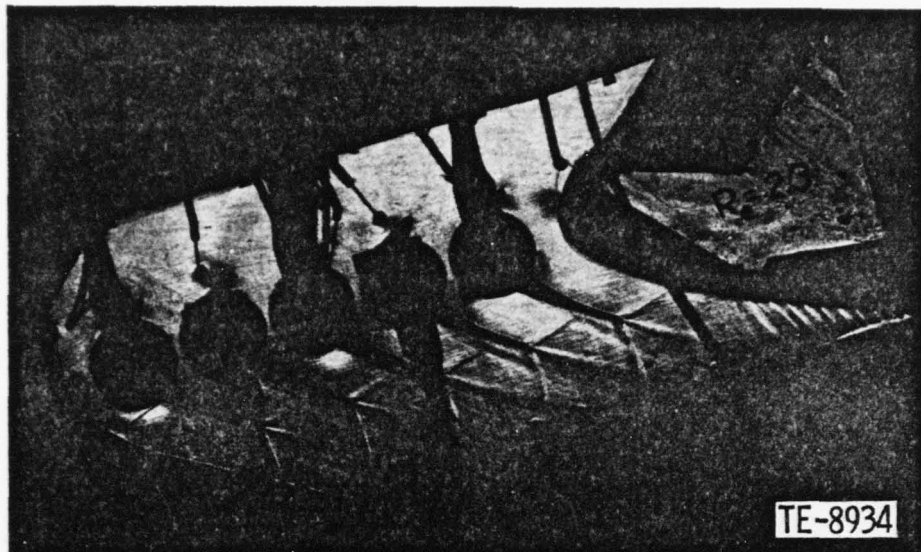


Figure 13. Schlieren at 2.3 expansion ratio.

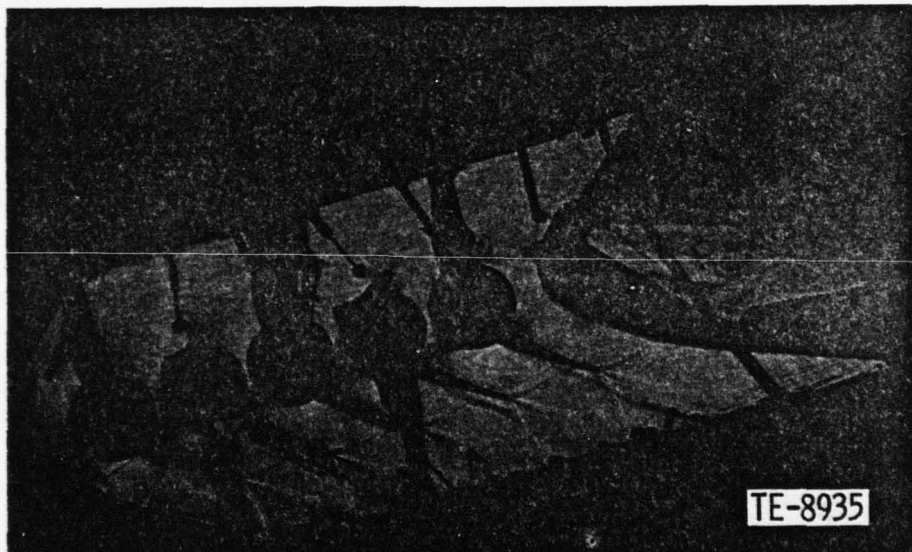


Figure 14. Schlieren at 2.8 expansion ratio.

Exit surveys were made at each operating point with a traversing five-hole cone probe. Figure 15 shows the wake profiles in terms of total pressure ratios as the probe was traversed from halfway between blades 3 and 4 to a point halfway between blades 2 and 3. As expansion ratio was increased, the pressure deficit shifted because of less turning and became more pronounced as the result of increased exit Mach number. The extra peak at about 80% passage in the 2.3 and 2.8 expansion ratio cases is attributable to the presence of a shock wave from the trailing edge of blade 3.

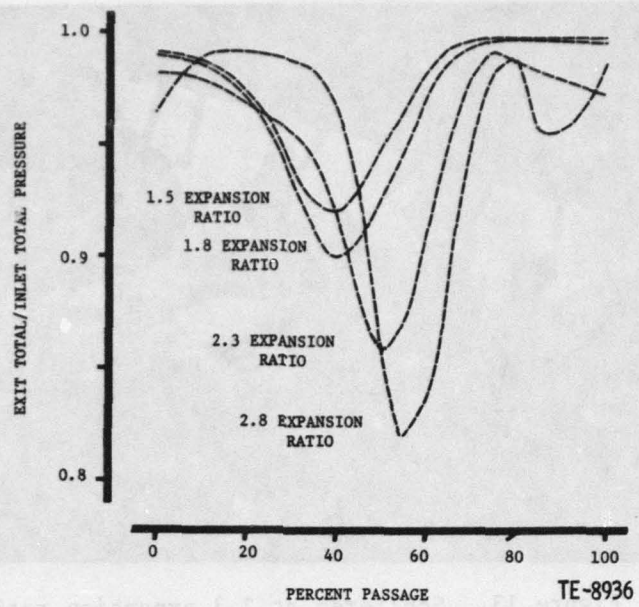


Figure 15. Steady-state cascade wake survey.

Blade 3 was instrumented with 18 surface static pressure taps for the steady-state and quasi-static testing--nine on each surface. The surface static pressure distributions obtained are presented in Figures 16 through 19 for the four steady-state operating conditions. Zero percent projected chord is the airfoil leading edge. A DDA steady-state analysis based on the work of Coustou (22) was performed for each point and is presented for comparison with the experimental data. The analysis is in good overall agreement with the experimental data except for the 5% to 30% projected chord region of the pressure surface leading edge and the 60% to 90% suction surface trailing edge region for the two subsonic exit cases. The suction surface trailing edge region data show a local deceleration trend at about 70% projected chord, which is also demonstrated by the analysis although the predicted level is lower. The transonic exit predictions show an abrupt slope change near 90% chord on the suction surface, which is caused by the impinging shock wave from blade 2. The analysis also misses local acceleration around the leading edge of the pressure surface. Adjustments to the analytical program would improve the correlation somewhat because the analysis has not been tailored to airfoils with extremely high camber and does not include any viscous effects.

#### Quasi-Static Experiment

A quasi-static experiment was conducted at the 1.5 and 2.8 expansion ratio operating points. The purpose of this test was to measure the steady-state static pressures resulting on the center airfoil as the cascade was reset to fixed setting angles representing temporal angular positions in the torsional cycle of oscillation at zero interblade phase angle. Quarter-cycle angular positions at zero interblade phase angle correspond physically to nominal, maximum-open, nominal, and maximum-closed setting angles. A 1° peak

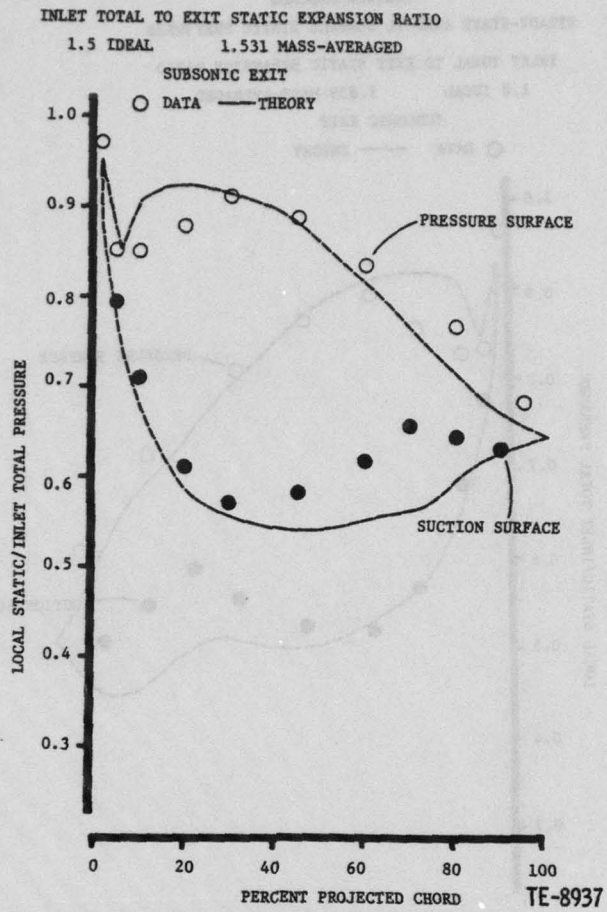


Figure 16. Steady-state airfoil surface static pressures for 1.5 expansion ratio.

torsional amplitude was chosen to create measurable surface static pressure differences resulting from the reset.

Figures 20 and 21 show the quasi-static surface static-pressure distributions for the 1.5 and 2.8 expansion ratios. Zero percent projected chord is the airfoil leading edge. As the cascade setting angle was opened (which corresponds to moving the trailing edges down in Figure 12), the static pressures on the airfoil surfaces were decreased, indicating increased velocities through the cascade. Closing the cascade setting angle resulted in increased surface static pressures from lower velocities through the cascade. The surface trends do not vary dramatically from the nominal setting angle trends on either surface, but more pressure change is observed on the suction surface when the cascade setting is opened.

For later comparison with the dynamic data at zero interblade phase angle, the pressure differentials on each airfoil surface resulting from the quasi-static test were normalized and are presented in Figures 22 and 23. The normalized differential was calculated by subtracting the open-setting

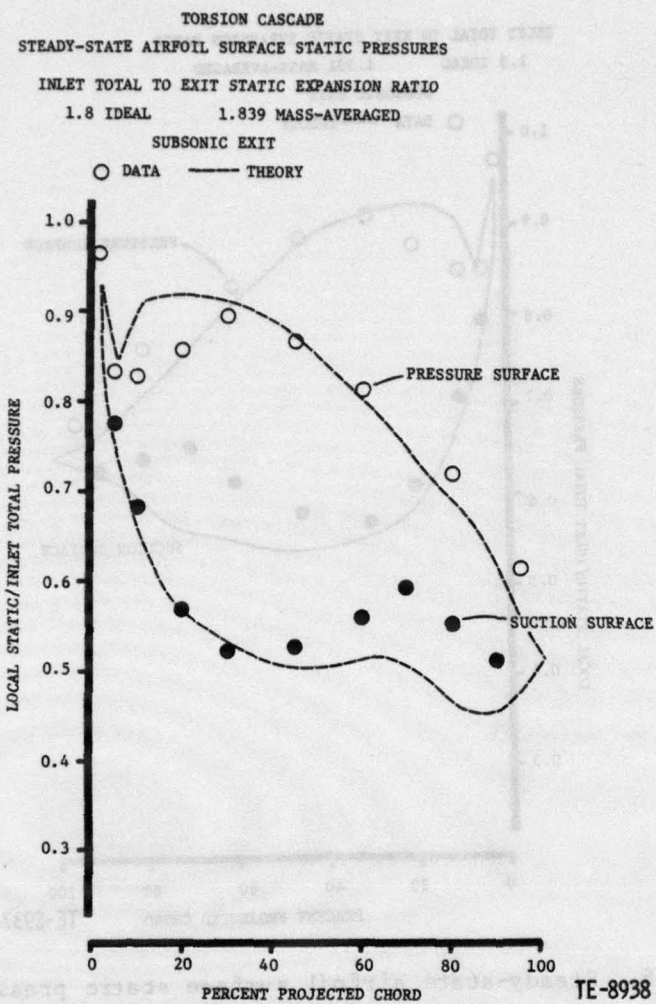


Figure 17. Steady-state airfoil surface static pressures for 1.8 expansion ratio.

pressure from the closed-setting pressure and dividing by twice the product of the dynamic head and the peak angular rotation of the airfoil:

$$\text{Normalized } P = (P_{\text{closed}} - P_{\text{open}})/\rho V^2 a$$

The data points identified by dash marks in Figures 22 and 23 have negative differential values because the closed-setting pressure was less than the corresponding open-setting pressure. The absolute values of these points are plotted. At 90% projected chord (in Figure 23), the effect of an impinging shock wave is seen on the suction surface. These quasi-static data will be compared with the corresponding dynamic results under a subsequent heading.

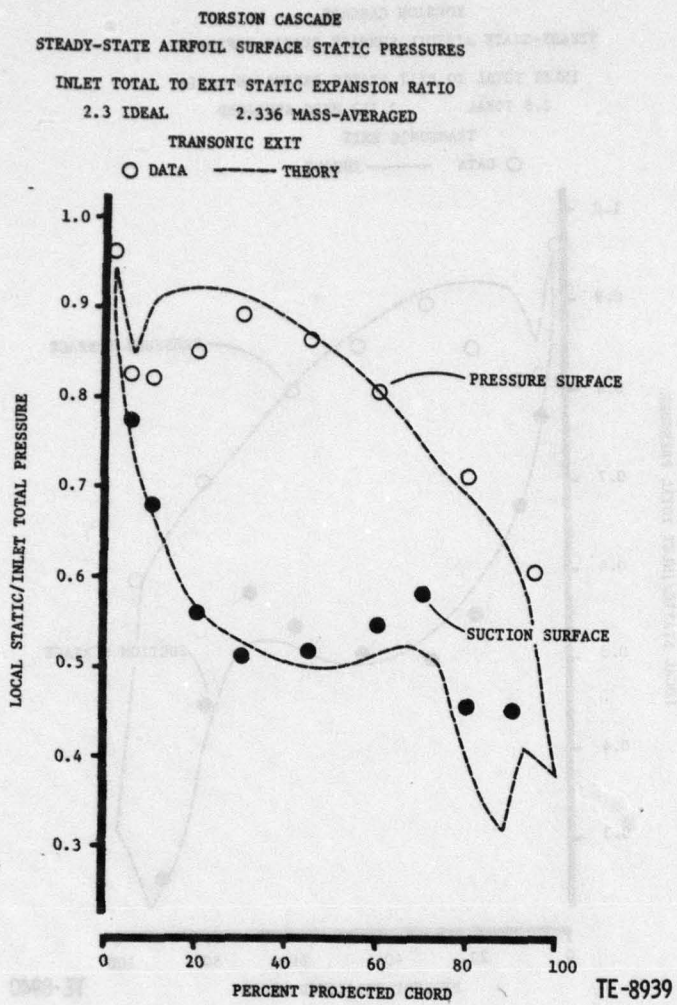


Figure 18. Steady-state airfoil surface static pressures for 2.3 expansion ratio.

#### Time-Variant Testing

The time-variant phase of the experimental research program was conducted by installing the Kulite-instrumented airfoil as blade 3 of the cascade and measuring the dynamic pressures generated on the airfoil surface during controlled cascade torsional oscillation. Pressure phase lag referenced to the motion of blade 3 was obtained, as was peak pressure amplitude. The peak torsional amplitude of each cascade airfoil and the precise phase of its motion with respect to blade 3 was also measured. The effects of four values of interblade phase angle were investigated over the range  $+90^\circ$  to  $-180^\circ$  for each of the four operating conditions described by the steady-state data. The effects of two additional interblade phase angles,  $+45^\circ$  and  $-45^\circ$ , were investigated at each operating condition under Independent Research and Development funding and are included to complement the data set.

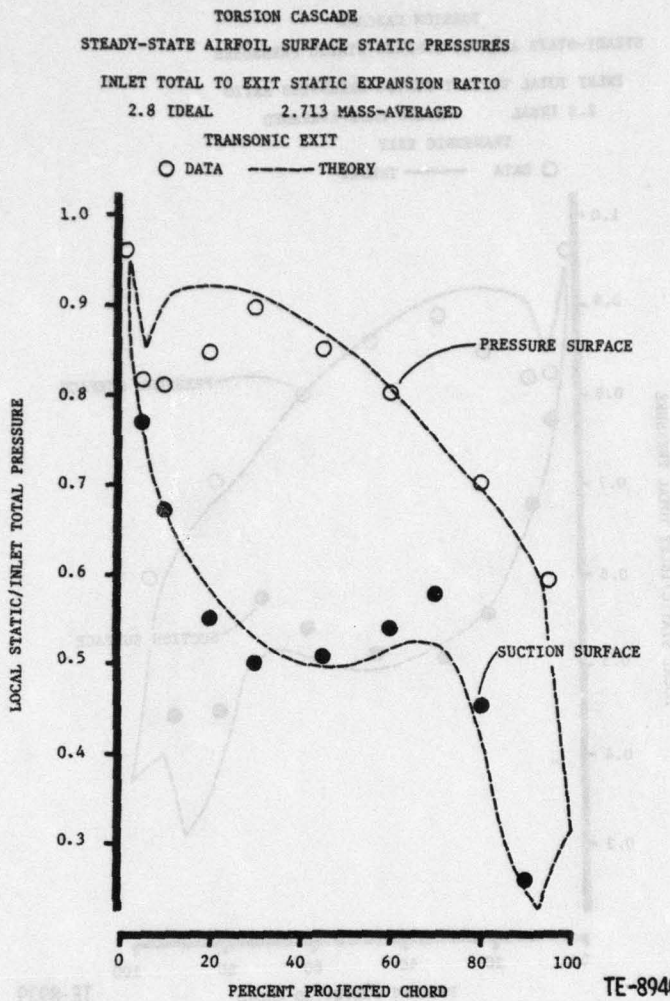


Figure 19. Steady-state airfoil surface static pressures for 2.8 expansion ratio.

A summary of the cascade airfoil motion at each dynamic test condition is presented in Table 4. The interblade phase angle in the first column is positive in sign when the motion of blade 1 is leading the motion of blade 2 as defined in Figure 12.

The frequency of oscillation was nominally 345 Hz for each test point. This value was selected after determination of the amplitude capabilities of the cascade torsional drive system at various frequencies of oscillation.

The torsion drive systems were computer controlled and adjusted to a deviation of less than 5° from the nominal value of interblade phase angle. The resulting phase angles between each of the cascade airfoils are listed in Table 4 along with the average interblade phase angle.

The torsional peak amplitude of blade 3 is listed in column 10 of Table 4, and the amplitude ratios of the other cascade blades with respect to the

TABLE 4. DYNAMIC DATA AIRFOIL MOTION SUMMARY

IDEAL TOTAL TO STATIC EXPANSION RATIO	FREQUENCY	INTERBLADE PHASE ANGLE				DEVIAION	0-P α <sub>3</sub>	BLADE AMPLITUDE	α <sub>4</sub> /α <sub>3</sub>	α <sub>5</sub> /α <sub>3</sub>
		φ <sub>1-2</sub>	φ <sub>2-3</sub>	φ <sub>3-4</sub>	φ <sub>4-5</sub>					
90°	1.5:1	344 Hz	89.1°	93.0°	87.4°	89.5°	89.7°	2.3°	0.093°	0.85
45 (1.531)			49.9	43.8	42.7	43.7	45.0	3.3	0.088	1.25
0 (MASS-AVERAGED)			0.9	-4.1	+4.2	-4.6	-0.9	4.2	0.118	1.73
-45			-44.8	-44.1	-44.6	-43.0	-44.1	0.8	0.124	1.21
-90			-91.0	-87.6	-90.9	-89.9	-89.9	1.6	0.128	1.25
180			180.9	180.1	179.8	174.9	178.9	2.7	0.102	1.21
90	1.8:1	344	92.5	90.6	89.1	93.0	91.3	1.8	0.091	0.85
45 (1.839)			43.8	50.5	46.7	48.4	47.3	2.8	0.100	1.39
0 (MASS-AVERAGED)			1.2	-1.2	1.4	-1.0	0.1	1.4	0.118	1.39
-45			-45.6	-41.8	-43.5	-50.6	-45.4	3.8	0.126	1.39
-90			-89.9	-86.3	-90.0	-86.9	-88.3	1.9	0.098	1.39
180			182.4	177.0	178.6	179.1	179.2	2.3	0.125	1.39
90	2.3:1	344	87.6	92.4	87.5	91.2	89.7	2.5	0.129	0.88
45 (2.336)			49.8	42.4	44.6	43.5	45.1	3.3	0.144	0.88
0 (MASS-AVERAGED)			0.6	-4.1	2.9	1.5	0.2	3.1	0.131	0.88
-45			-47.2	-43.1	-44.9	-44.1	-44.8	1.7	0.156	0.95
-90			-89.4	-87.7	-89.8	-91.3	-89.6	1.5	0.095	1.57
180			344	179.2	177.3	178.1	180.7	1.5	0.123	0.95
90	2.8:1	345	87.3	96.0	86.2	92.4	90.5	4.6	0.104	0.85
45 (2.713)			44.0	50.6	42.0	43.6	45.1	3.8	0.126	0.85
0 (MASS-AVERAGED)			0.9	-3.4	0.7	3.1	0.3	2.7	0.127	0.85
-45			-44.0	-45.5	-44.3	-49.6	-45.9	2.6	0.144	0.85
-90			-89.2	-86.2	-94.4	-87.5	-89.3	3.6	0.105	1.13
180			345	182.5	178.6	177.6	179.0	2.1	0.113	1.13

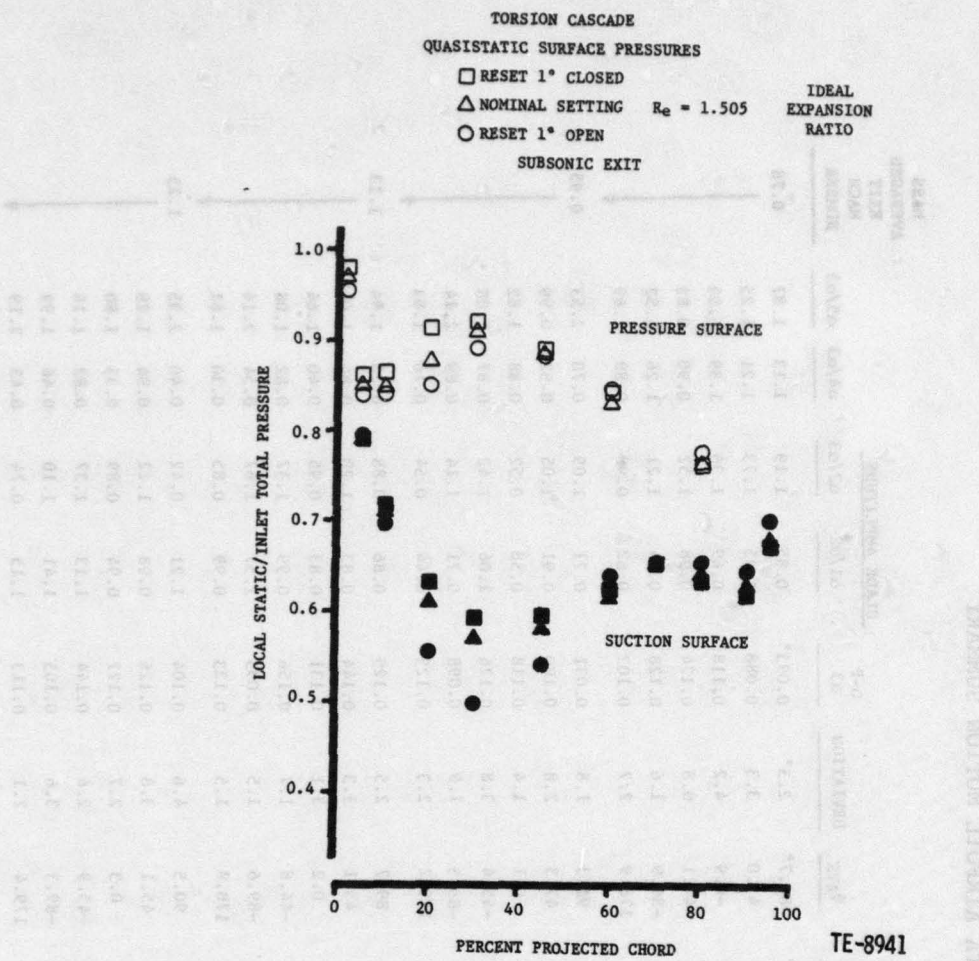


Figure 20. Quasi-static surface pressure distributions for 1.5 expansion ratio.

center blade follow in the next four columns. Constant amplitude for all the cascade blades is very difficult to achieve with the resonant-frequency drive system because of small differences in mechanical damping.

The four aerodynamic conditions are identified in Table 4 by the expansion ratios in column 2 and the cascade exit Mach numbers in the last column.

High-speed color schlieren movies were taken at an expansion ratio of 2.8 for interblade phase angle values of  $0^\circ$  and  $180^\circ$ . In the movies the torsional motion of blades 4 and 5 is clearly visible, and the exit shock structures can also be seen to move. The interblade phase angle is easily identified by observing that blades 4 and 5 move in unison in the  $0^\circ$  movie and in opposition in the  $180^\circ$  movie.

The dynamic airfoil surface pressure data from the Kulite transducers were obtained and analyzed as described earlier. The acceleration/strain contribution to the overall Kulite signal was less than 5%. Unfortunately, the

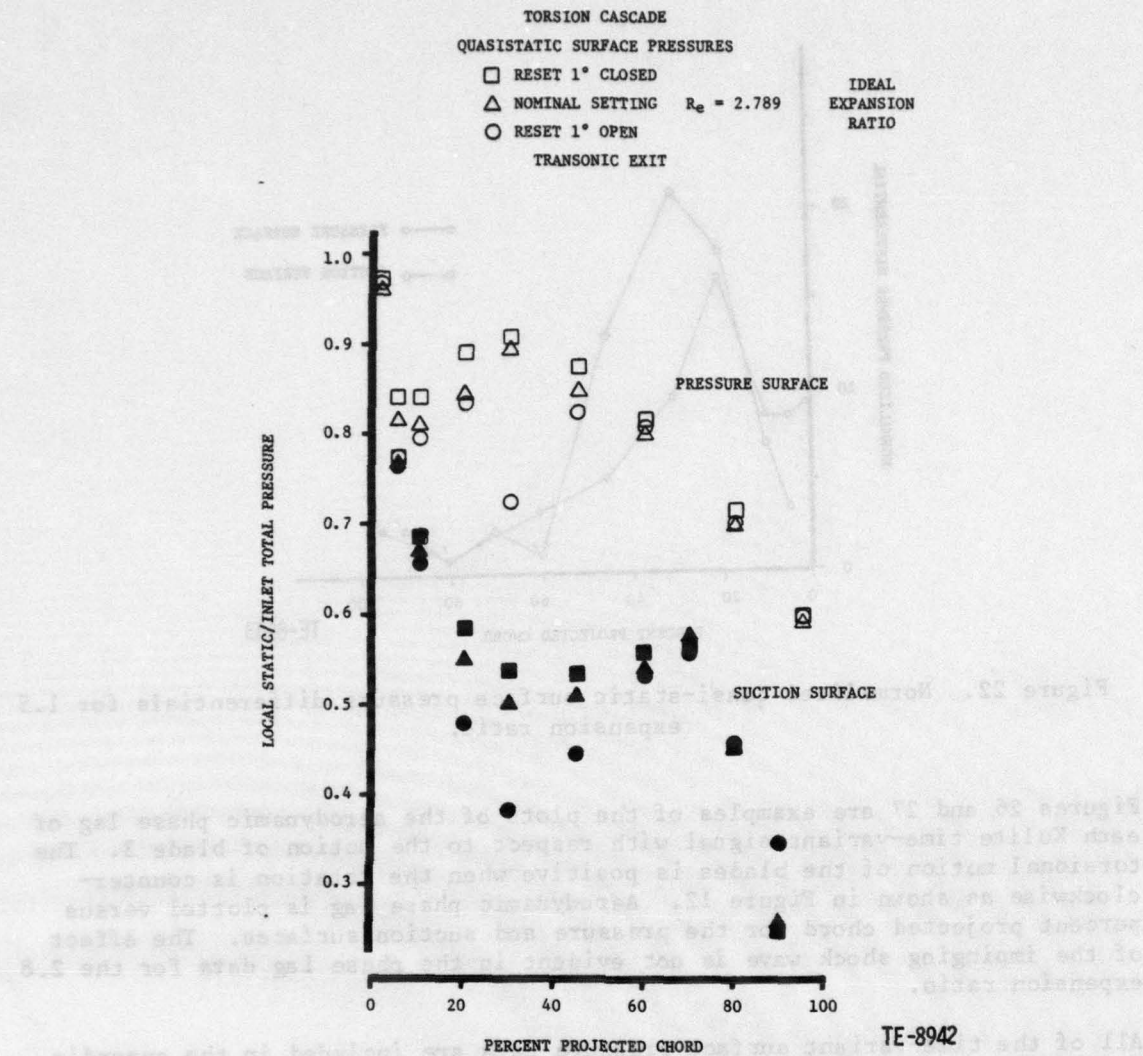


Figure 21. Quasi-static surface pressure distributions for 2.8 expansion ratio.

Kulite transducer at 30% projected chord ceased to function before it could yield any dynamic data.

Figures 24 and 25 are examples of the peak time-variant surface pressure amplitude plots. These two plots are for the 1.5 and 2.8 expansion ratios with the cascade interblade phase angle at zero. Unsteady pressure peak amplitude is plotted versus percent projected chord for the pressure and suction surfaces. The amplitude trends seen in the curves are typical for all the dynamic data and can be related to the quasi-static pressure trends, as will be shown later. The higher amplitude at 92.5% projected chord on the suction surface (Figure 25) is the result of an impinging shock wave from blade 2. This effect is present throughout all of the 2.8 expansion ratio amplitude data.

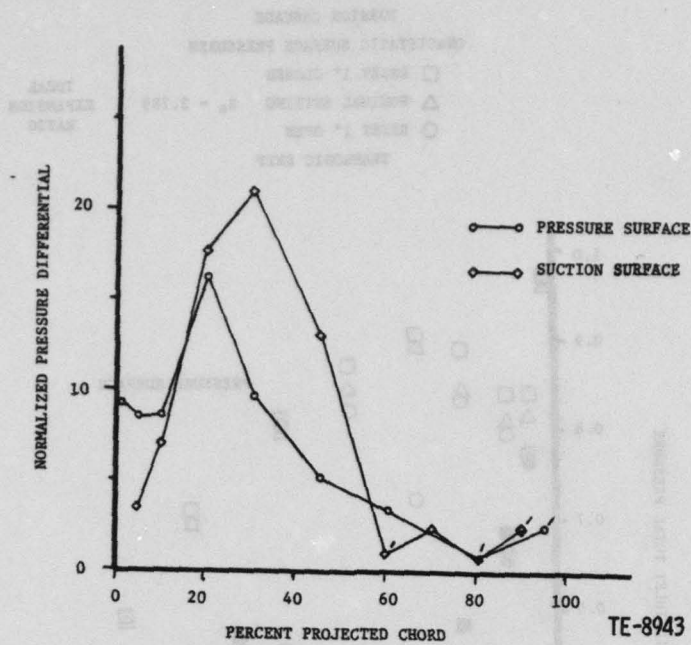


Figure 22. Normalized quasi-static surface pressure differentials for 1.5 expansion ratio.

Figures 26 and 27 are examples of the plots of the aerodynamic phase lag of each Kulite time-variant signal with respect to the motion of blade 3. The torsional motion of the blades is positive when the rotation is counter-clockwise as shown in Figure 12. Aerodynamic phase lag is plotted versus percent projected chord for the pressure and suction surfaces. The effect of the impinging shock wave is not evident in the phase lag data for the 2.8 expansion ratio.

All of the time-variant surface pressure data are included in the appendix. Each point can be paired with its corresponding cascade blade motion in Table 4 by matching interblade phase angle and expansion ratio. The correlation of these data with a state-of-the-art analysis is performed under "Correlation of Results."

A study was made to determine the relative unsteady pressure effects of oscillating each cascade airfoil alone. Blade 3 was first oscillated at 345 Hz while the other cascade airfoils were held stationary. The peak dynamic pressure amplitude of each Kulite transducer was then measured and divided by the torsional amplitude of blade 3. Each of the other cascade airfoils was treated similarly to obtain the Kulite peak amplitudes divided by the amplitude of the single oscillating airfoil in each case. All of these quantities were then normalized to the results of shaking blade 3 alone; the results for each of the expansion ratios of the experiment are presented in Table 5.

As can be seen, the primary unsteady pressure effects came from oscillating blade 3, although the suction surface transducers are substantially affected by oscillating blade 2. It is evident that blade 2 has more effect on the

TABLE 5. RELATIVE CONTRIBUTIONS OF INDIVIDUAL AIRFOILS ON SURFACE  
DYNAMIC PRESSURES.

IDEAL TOTAL TO STATIC EXPANSION RATIO	PRESSURE SURFACE					SUCTION SURFACE				
	SINGLE OSCILLATING AIRFOIL		P1	P3	P4	P5	S1	S2	S3	S4
	1	.065	.098	.098	.143	.349	.291	.153	.050	.167
1.5	1	.052	.077	.046	.091	.523	1.41	1.82	1.07	.758
	2	1.0	1.0	1.0	1.0	1.0	1.0	1.0	1.0	.330
	3	.328	.582	.716	.985	.131	.101	.149	.174	.524
	4	.065	.157	.196	.113	.092	.023	.143	.060	.098
	5									
1.8	1	.055	.091	.080	.095	.436	.347	.101	.123	.221
	2	.044	.044	.039	.047	.574	1.52	2.30	1.41	1.12
	3	1.0	1.0	1.0	1.0	1.0	1.0	1.0	1.0	.523
	4	.287	.507	.589	.703	.150	.082	.079	.067	.1.0
	5	.039	.078	.091	.151	.078	.105	.093	.119	.273
2.3	1	.027	.111	.080	.096	.500	.340	.089	.068	.150
	2	.041	.050	.031	.025	.561	1.63	2.36	1.54	1.35
	3	1.0	1.0	1.0	1.0	1.0	1.0	1.0	1.0	.852
	4	.244	.482	.531	.601	.113	.052	.045	.049	.089
	5	.038	.030	.039	.031	.024	.044	.061	.079	.048
2.8	1	.052	.093	.069	.081	.600	.392	.089	.059	.153
	2	1.0	.028	.047	.031	.024	.554	1.61	2.59	1.57
	3	.215	.423	.489	.520	.102	.073	.067	.043	.055
	4	.065	.063	.092	.065	.065	.094	.087	.037	.036

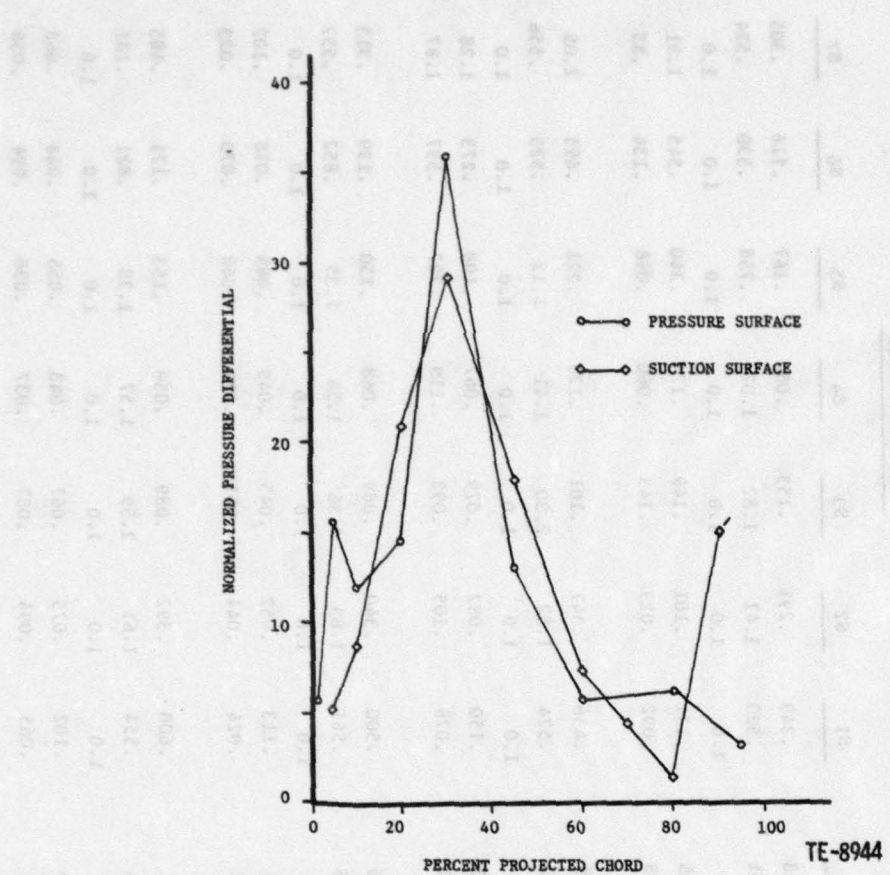


Figure 23. Normalized quasi-static surface pressure differentials for 2.8 expansion ratio.

suction surface of blade 3, whereas blade 4 has the most effect on the pressure surface of blade 3. This finding is consistent with the cascade geometry as shown in Figure 12. The effects of blades 1 and 5 are comparatively small.

#### CORRELATION OF RESULTS

The measured time-variant and calculated data were compared for each condition listed in Table 4. An internally developed computer code based on the method outlined by Smith<sup>(6)</sup> was used for the theoretical calculations. In Figures 28 and 29, comparisons of this code and results obtained by Carstens<sup>(23)</sup> are plotted. The curves indicate substantial agreement over most of the airfoil surface except for local trailing edge effects.

Inasmuch as the analytical code is restricted to flat plates, the turbine airfoil cascade was examined to "best-fit" a flat-plate cascade to the highly cambered airfoils. As shown in Figure 30, two cascades were assumed for analytical purposes. The first of these, labeled the leading edge cascade,

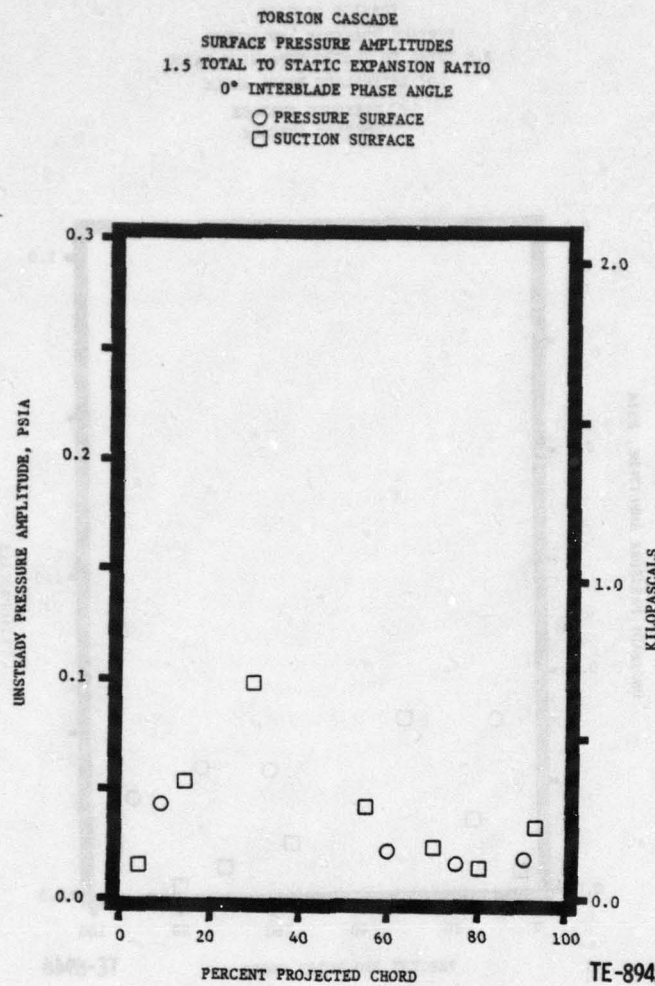


Figure 24. Time-variant surface pressure amplitude plot for 1.5 expansion ratio and 0° interblade phase angle.

was aligned with the inlet velocity vector of the cascade. The parameters necessary to analyze this assumed cascade were based on inlet quantities. The second cascade was formulated so that flat-plate airfoils were aligned with the setting angle of the turbine airfoils. The reduced frequency and Mach number were based on an average velocity of the fluid along the mean-line from the leading to the trailing edge. The parameters used in both cascades are listed in Table 6. Figure 31 depicts the two cascades arranged in a more conventional manner. Although several expansion ratios were investigated, only the calculated data for the 1.5 expansion ratio will be presented.

The correlation between the calculated results as described and the experimental data is presented in terms of normalized pressure coefficients along the meanline of the airfoil. Figures 32 through 43 describe the time-variant behavior of the differential pressure across the instrumented airfoil for the expansion ratios and interblade phase angles investigated. The normalized pressure coefficient is obtained experimentally by dividing the magnitude of time-variant pressure difference across the airfoil by the

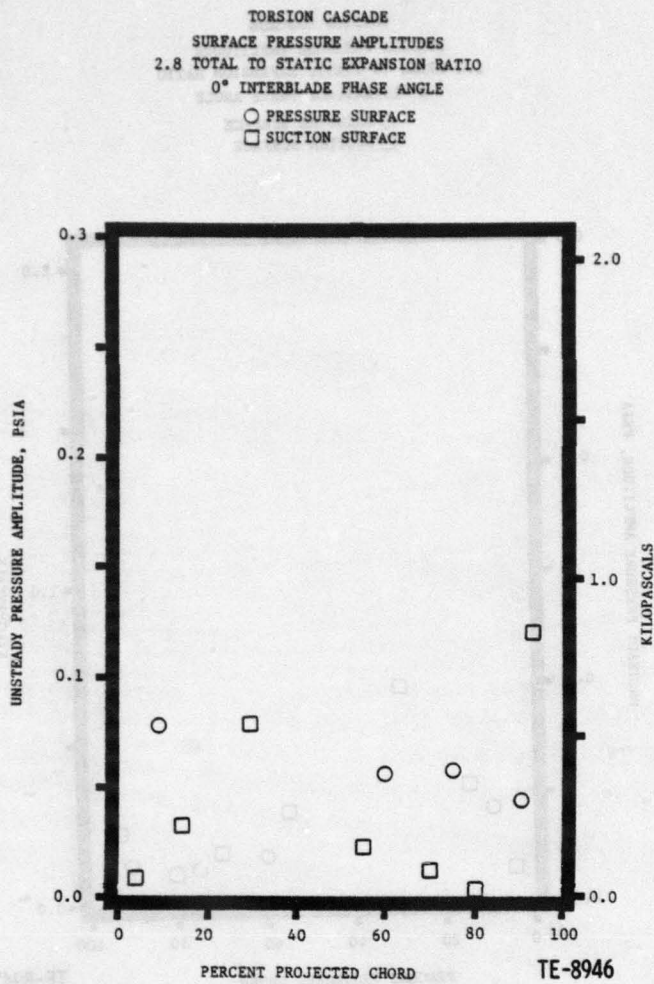


Figure 25. Time-variant surface pressure amplitude plot for 2.8 expansion ratio and 0° interblade phase angle.

TABLE 6. CONDITIONS ASSUMED FOR ANALYTICAL STUDY.

<u>Parameter</u>	<u>Leading edge cascade</u>	<u>Meanline cascade*</u>
Solidity (chord/spacing)	2.532	1.890
Reduced frequency (based on chord)	1.060	0.843
Setting angle, degrees	47.6	25.5
Mach number	0.500	0.489
Interblade phase angle	Variable	Variable

\* $R_e = 1.5$

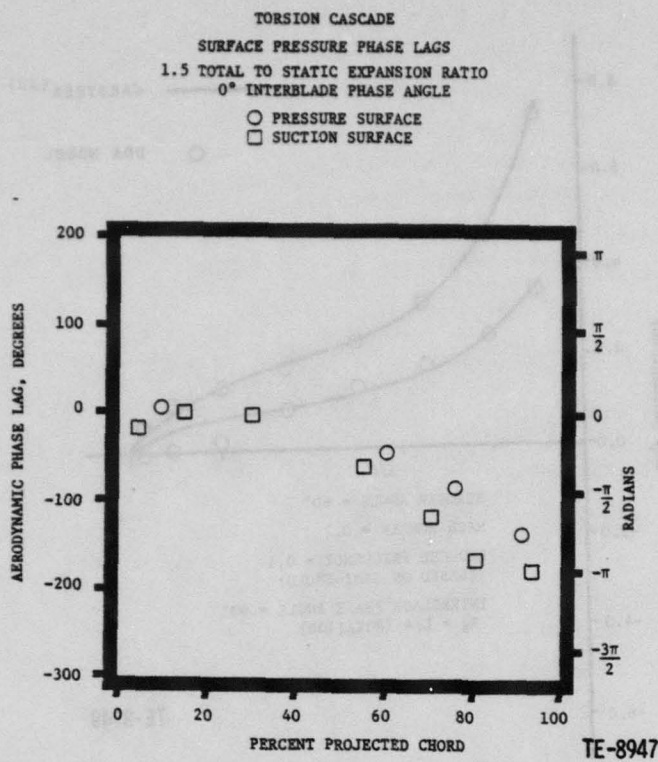


Figure 26. Time-variant surface pressure phase lag plot for 1.5 expansion ratio and 0° interblade phase angle.

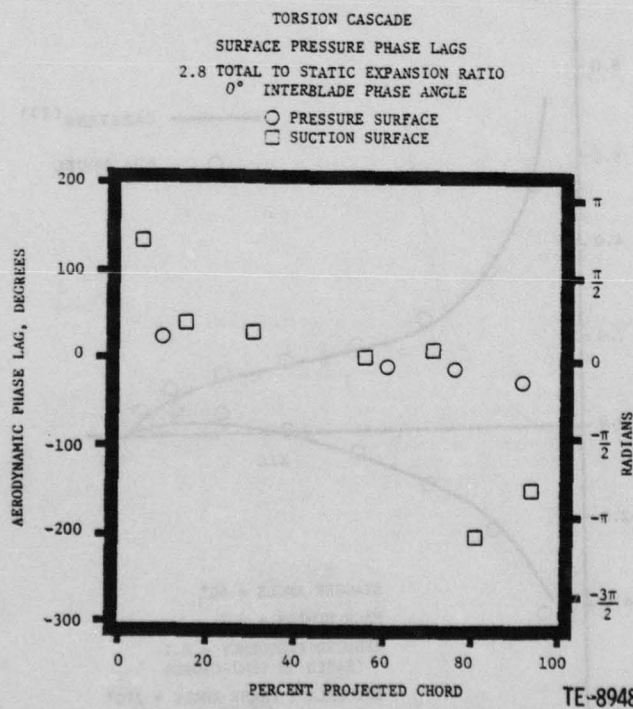


Figure 27. Time-variant surface pressure phase lag plot for 2.8 expansion ratio and 0° interblade phase angle.

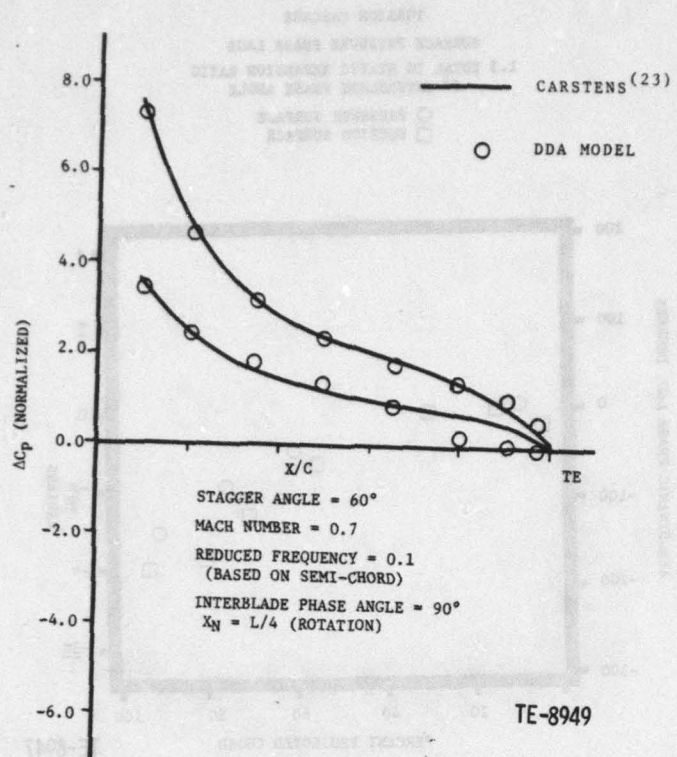


Figure 28. Correlation of calculated results at  $90^\circ$  phase.

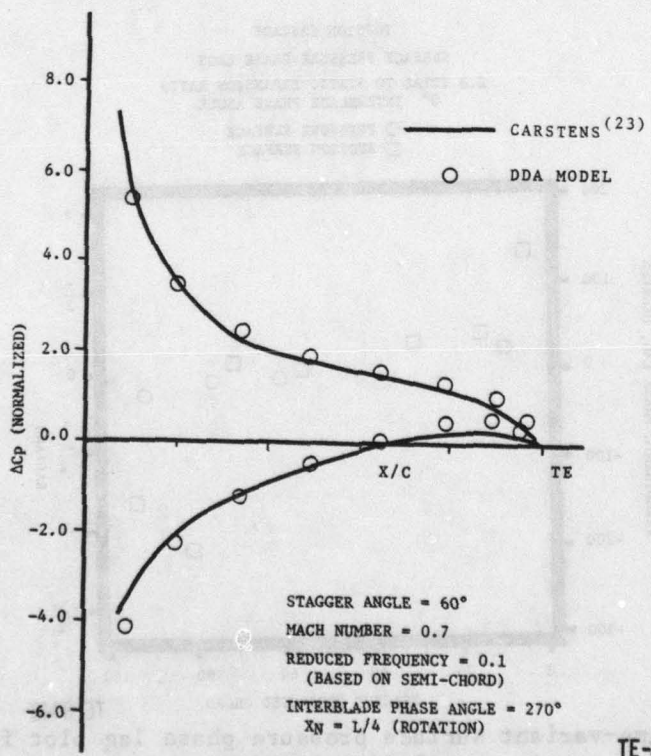


Figure 29. Correlation of calculated results at  $270^\circ$  phase.

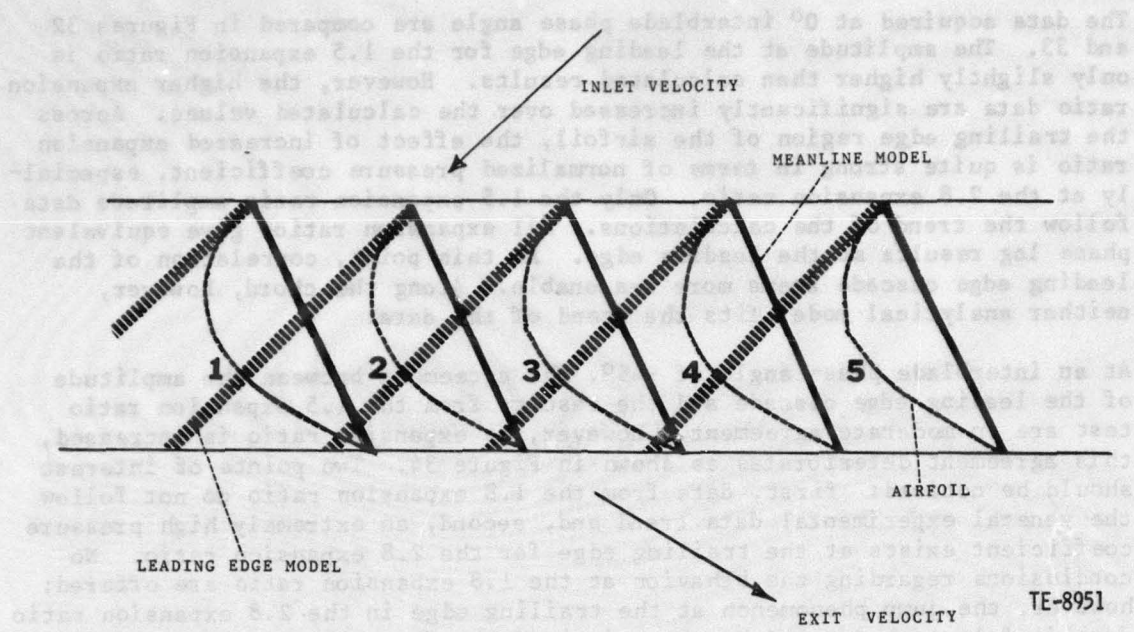


Figure 30. Assumed flat-plate cascades.

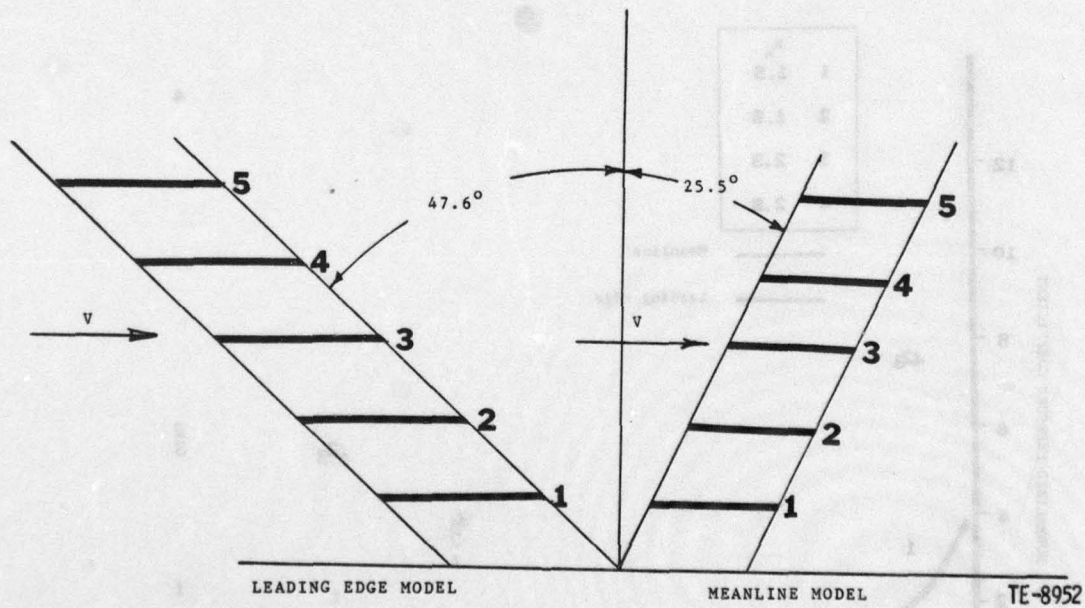


Figure 31. Description of flat-plate cascades.

product of twice the dynamic head and the rotational amplitude of the instrumented airfoil. The phase lag plotted in the curves is also referenced to the motion of the instrumented airfoil.

The data acquired at  $0^\circ$  interblade phase angle are compared in Figures 32 and 33. The amplitude at the leading edge for the 1.5 expansion ratio is only slightly higher than calculated results. However, the higher expansion ratio data are significantly increased over the calculated values. Across the trailing edge region of the airfoil, the effect of increased expansion ratio is quite strong in terms of normalized pressure coefficient, especially at the 2.8 expansion ratio. Only the 1.5 expansion ratio amplitude data follow the trend of the calculations. All expansion ratios give equivalent phase lag results at the leading edge. At this point, correlation of the leading edge cascade seems more reasonable. Along the chord, however, neither analytical model fits the trend of the data.

At an interblade phase angle of  $-45^\circ$ , the agreement between the amplitude of the leading edge cascade and the results from the 1.5 expansion ratio test are in moderate agreement. However, as expansion ratio is increased, this agreement deteriorates as shown in Figure 34. Two points of interest should be noticed: first, data from the 1.8 expansion ratio do not follow the general experimental data trend and, second, an extremely high pressure coefficient exists at the trailing edge for the 2.8 expansion ratio. No conclusions regarding the behavior at the 1.8 expansion ratio are offered; however, the jump phenomenon at the trailing edge in the 2.8 expansion ratio data is felt to be caused by shock impingement from the adjacent airfoil. With regard to phase lag (Figure 35), the experimental data agree more closely at the leading edge with the assumed meanline cascade results.

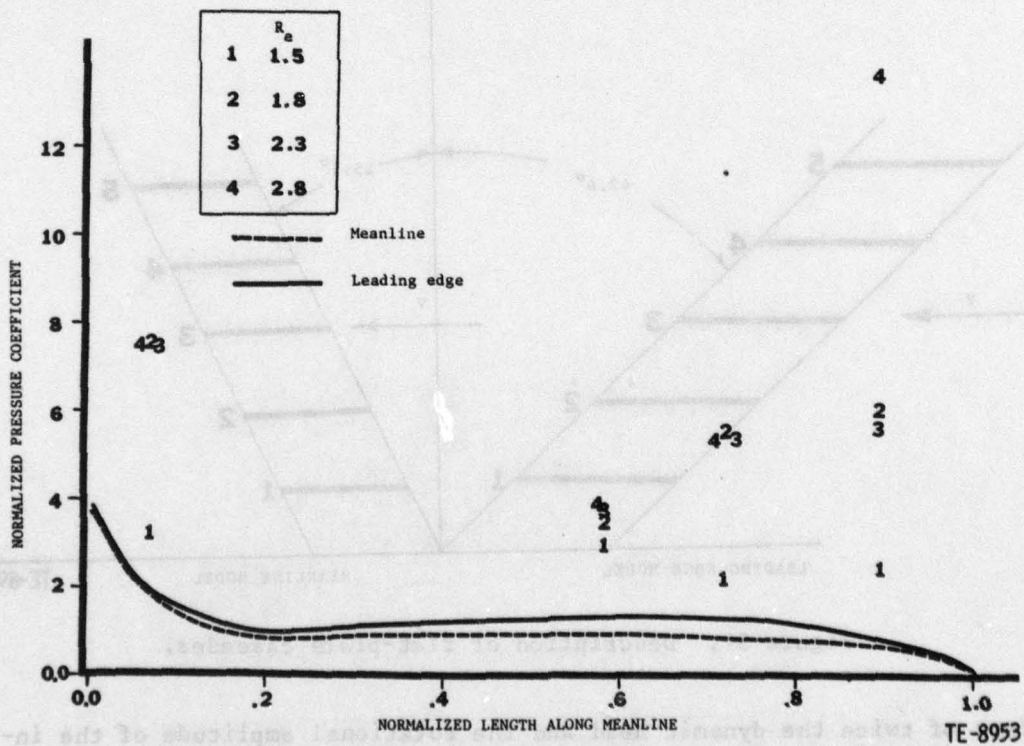


Figure 32. Normalized pressure coefficients for  $0^\circ$  interblade phase angle.

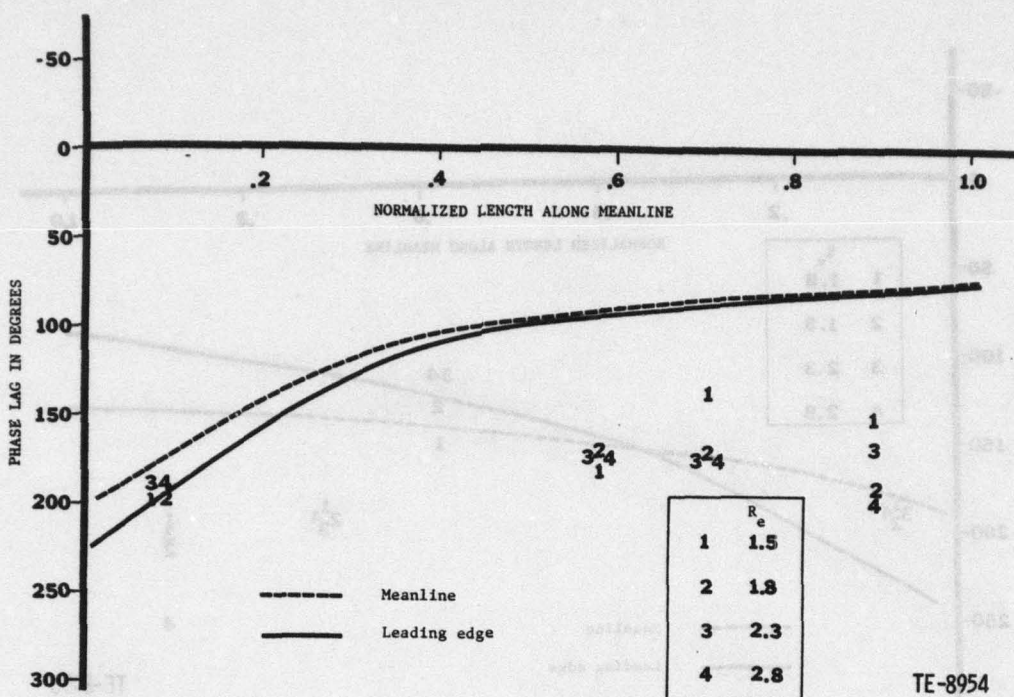


Figure 33. Phase lag for  $0^\circ$  interblade phase angle.

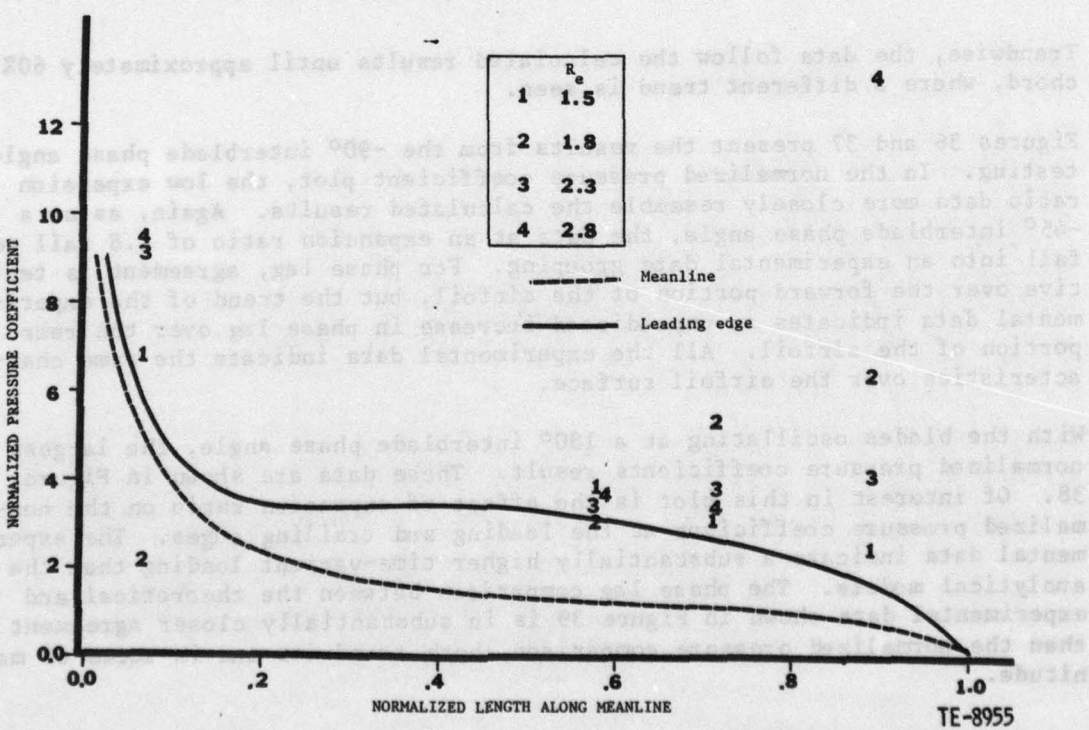


Figure 34. Normalized pressure coefficients for  $-45^\circ$  interblade phase angle.

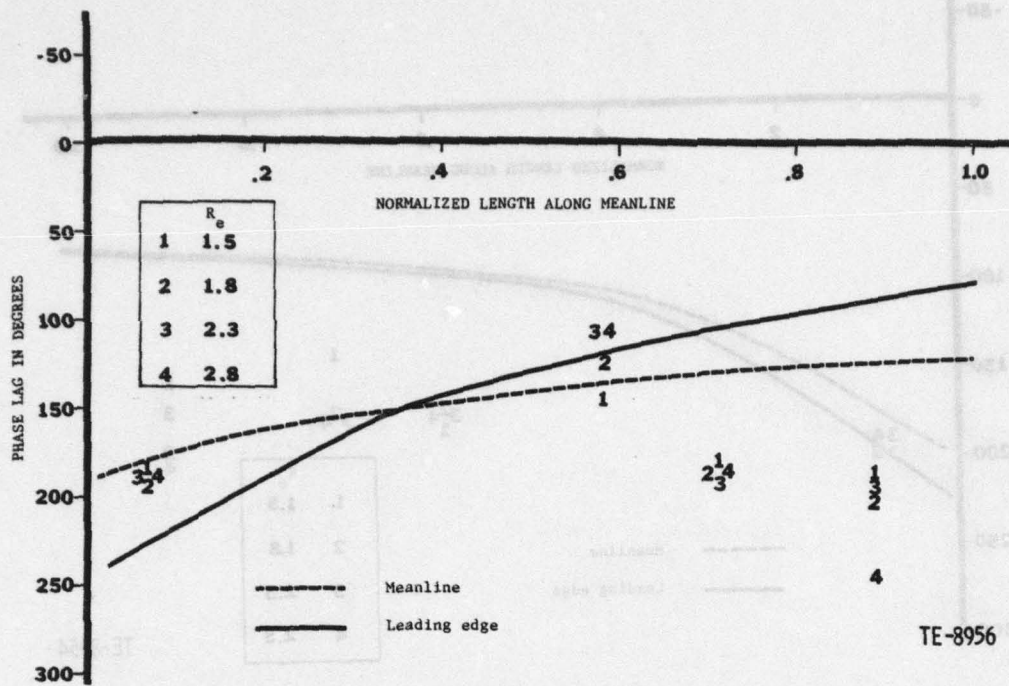


Figure 35. Phase lag for  $-45^\circ$  interblade phase angle.

Trendwise, the data follow the calculated results until approximately 60% chord, where a different trend is seen.

Figures 36 and 37 present the results from the  $-90^\circ$  interblade phase angle testing. In the normalized pressure coefficient plot, the low expansion ratio data more closely resemble the calculated results. Again, as at a  $-45^\circ$  interblade phase angle, the data at an expansion ratio of 1.8 fail to fall into an experimental data grouping. For phase lag, agreement is tentative over the forward portion of the airfoil, but the trend of the experimental data indicates an unpredicted increase in phase lag over the rear portion of the airfoil. All the experimental data indicate the same characteristics over the airfoil surface.

With the blades oscillating at a  $180^\circ$  interblade phase angle, the largest normalized pressure coefficients result. These data are shown in Figure 38. Of interest in this plot is the effect of expansion ratio on the normalized pressure coefficient at the leading and trailing edges. The experimental data indicate a substantially higher time-variant loading than the analytical models. The phase lag comparison between the theoretical and experimental data shown in Figure 39 is in substantially closer agreement than the normalized pressure comparison, both trendwise and in terms of magnitude.

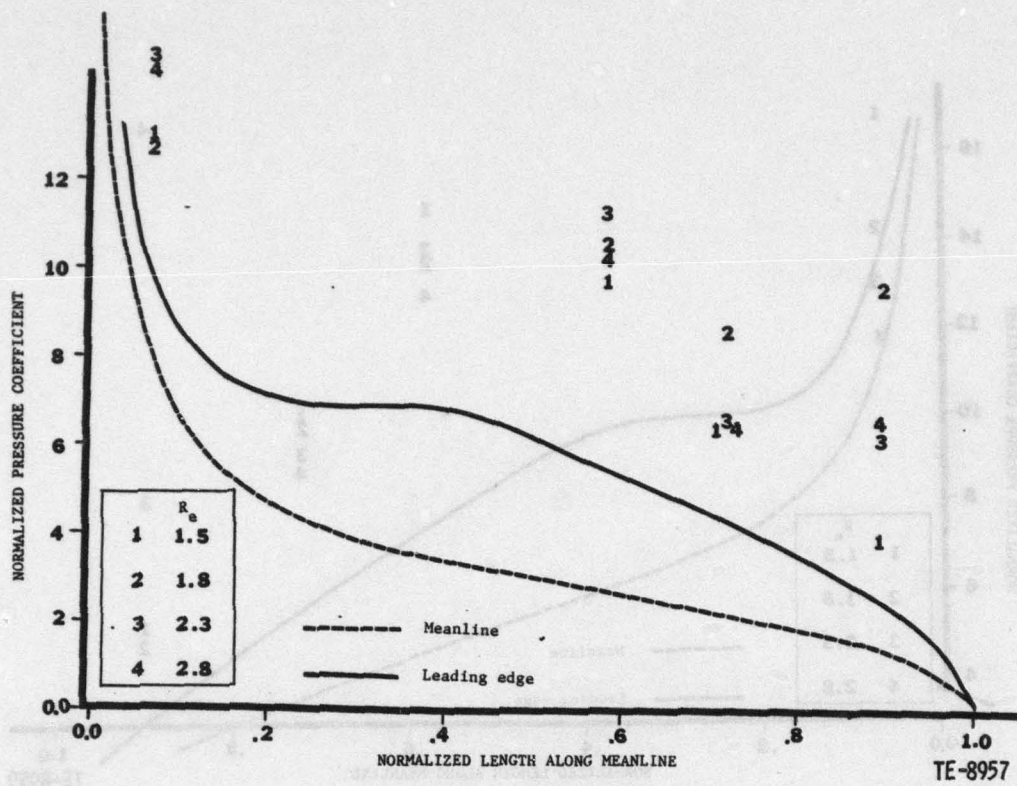


Figure 36. Normalized pressure coefficients for  $-90^\circ$  interblade phase angle.

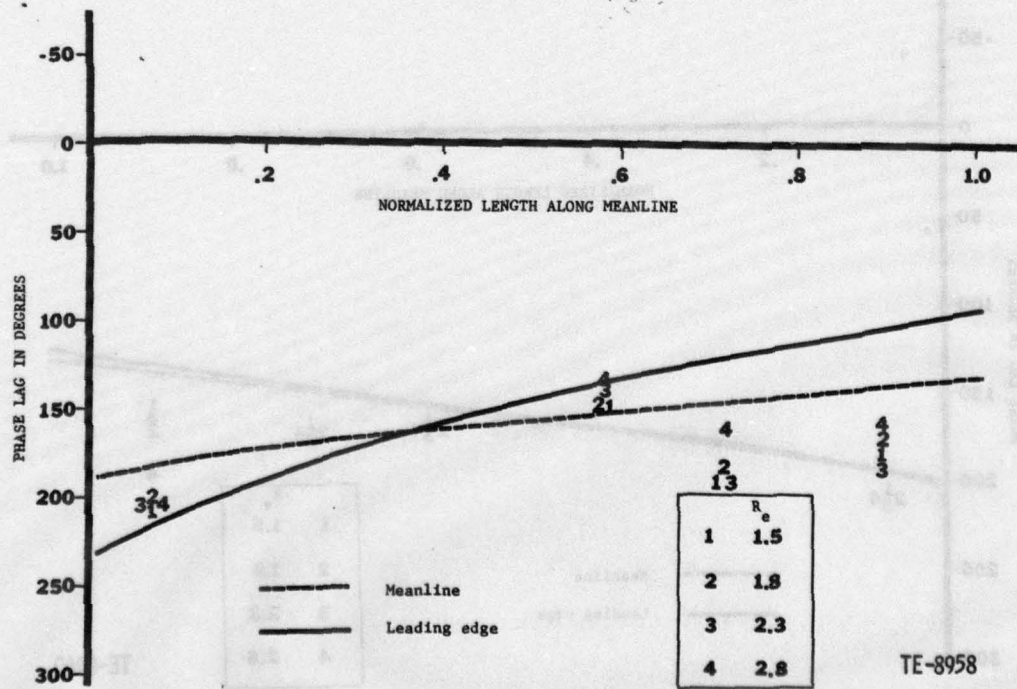


Figure 37. Phase lag for  $-90^\circ$  interblade phase angle.

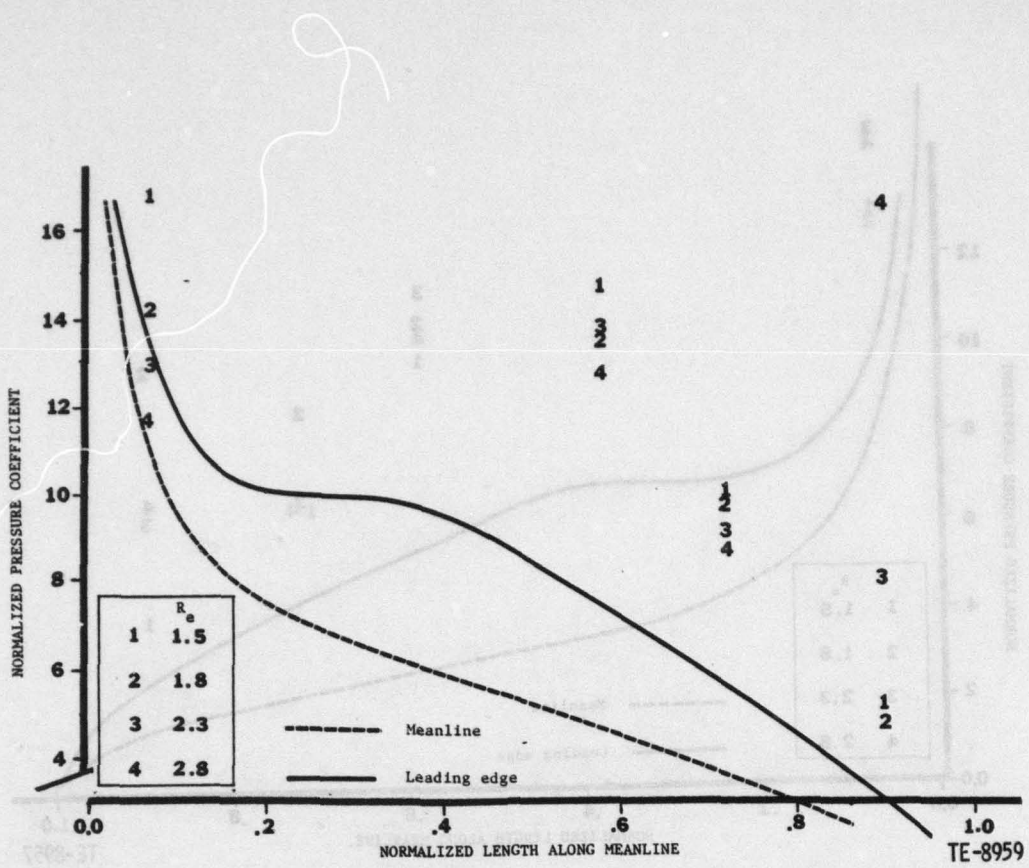


Figure 38. Normalized pressure coefficients for 180° interblade phase angle.

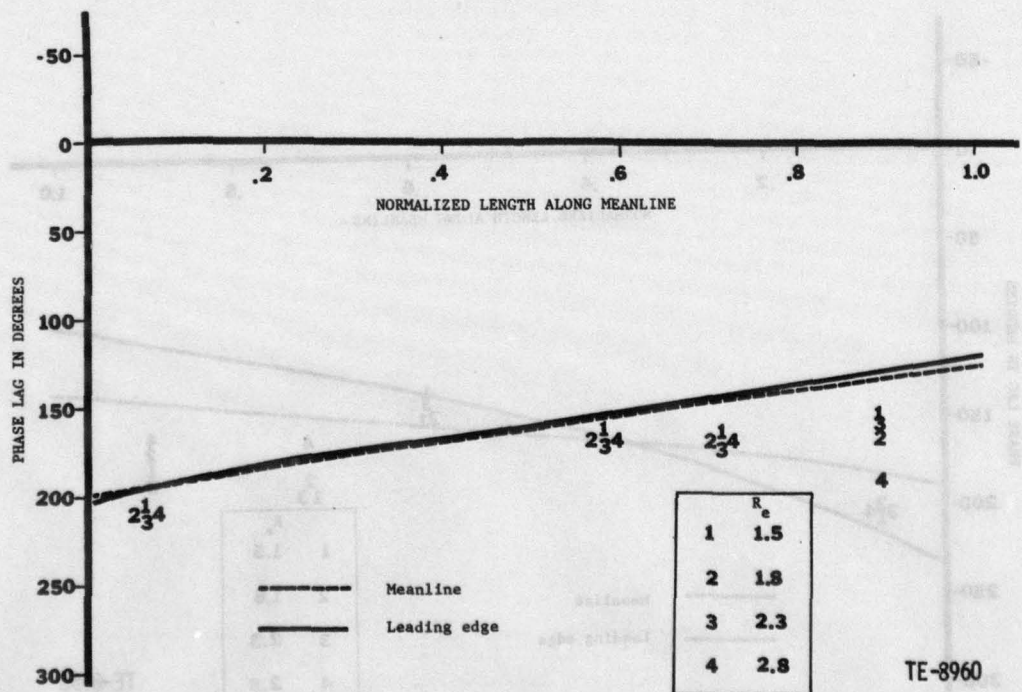


Figure 39. Phase lag for 180° interblade phase angle.

At the  $+90^\circ$  interblade phase angle, large deviations between the experimentally derived and theoretically calculated normalized pressure coefficients are shown in Figure 40. With the exception of the 1.8 expansion ratio, the experimental data are consistent trendwise over the forward two-thirds of the airfoil surface. In terms of phase lag (Figure 41), the assumed meanline cascade better models the leading edge phase characteristics. Close agreement exists between the experimental data over much of the airfoil; the effects of expansion ratio are evident in the trailing edge region.

Finally, the data acquired from the experimental investigations with a  $+45^\circ$  interblade phase angle are compared with theory in Figures 42 and 43. The normalized pressure coefficients measured experimentally follow the same trend over most of the airfoil, the exception occurring at the 2.8 expansion ratio because of shock impingement. The experimental data are of a much larger magnitude than the theoretical data shown in Figure 42. The phase lag comparisons in Figure 43 indicate good agreement between theory and experimental data, assuming a meanline cascade representation. The 1.5 expansion ratio phase lag data agree substantially with the meanline cascade prediction over the entire airfoil surface. The effect of expansion ratio destroys this agreement over the rear portion of the airfoil.

The normalized pressure coefficient data comparison with theoretical predictions indicated large deviations between the two. As a means to explore this disagreement in greater depth, plots of normalized pressure coefficients at each measuring station versus interblade phase angle from both

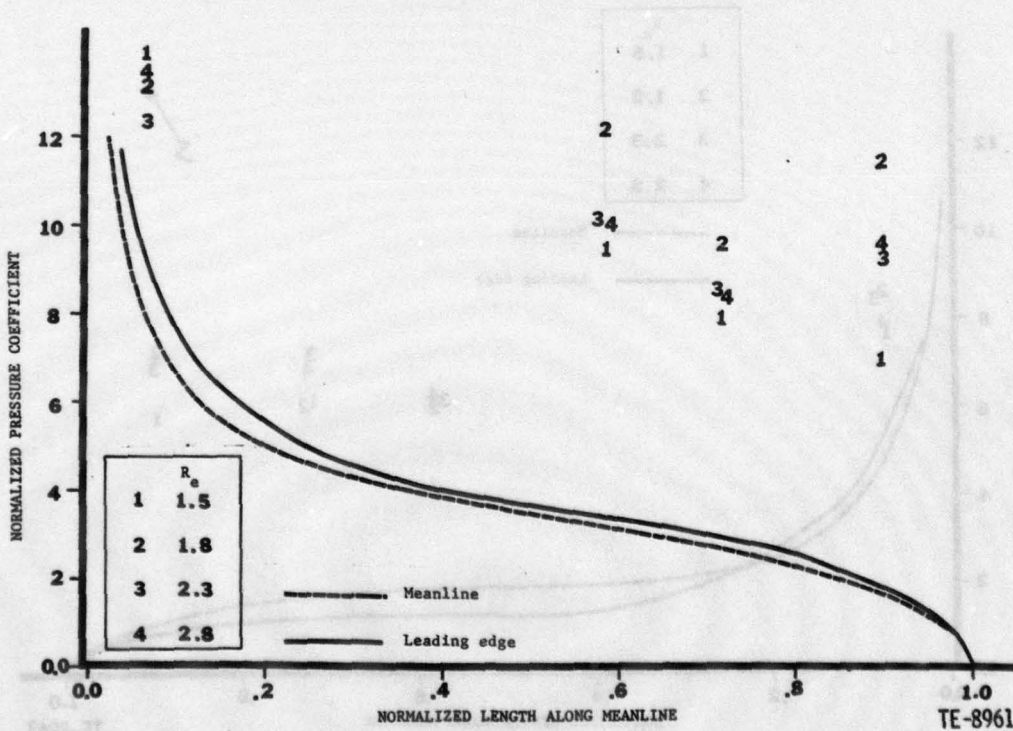


Figure 40. Normalized pressure coefficients for  $90^\circ$  interblade phase angle.

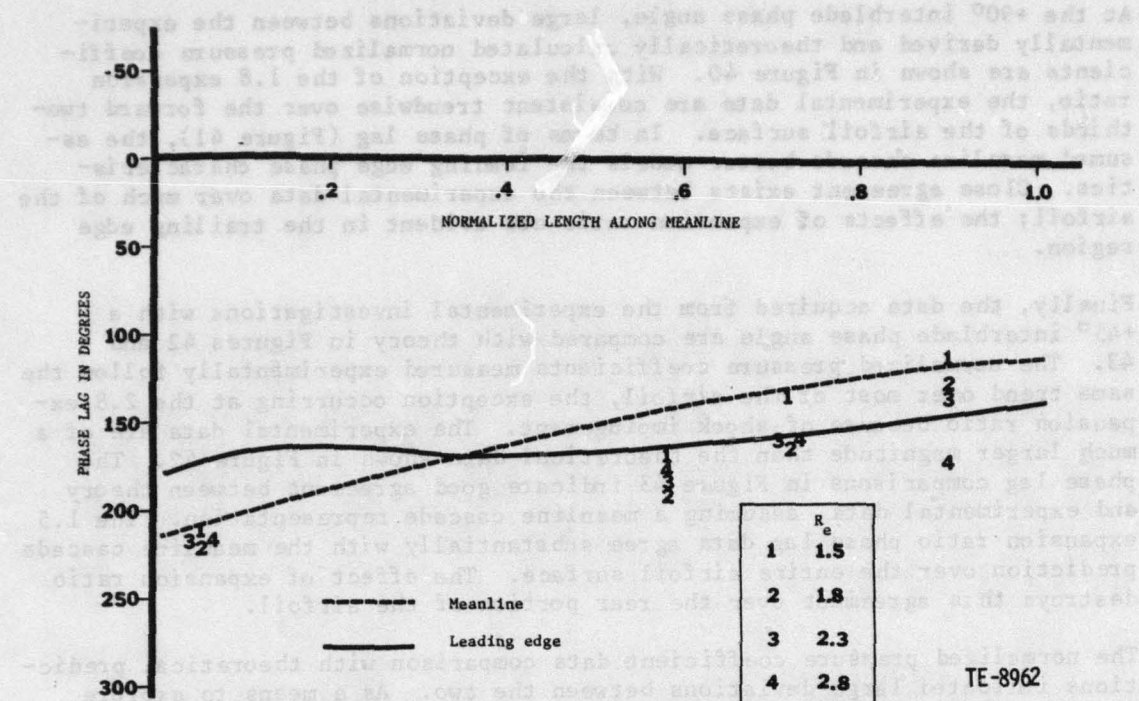


Figure 41. Phase lag for 90° interblade phase angle.

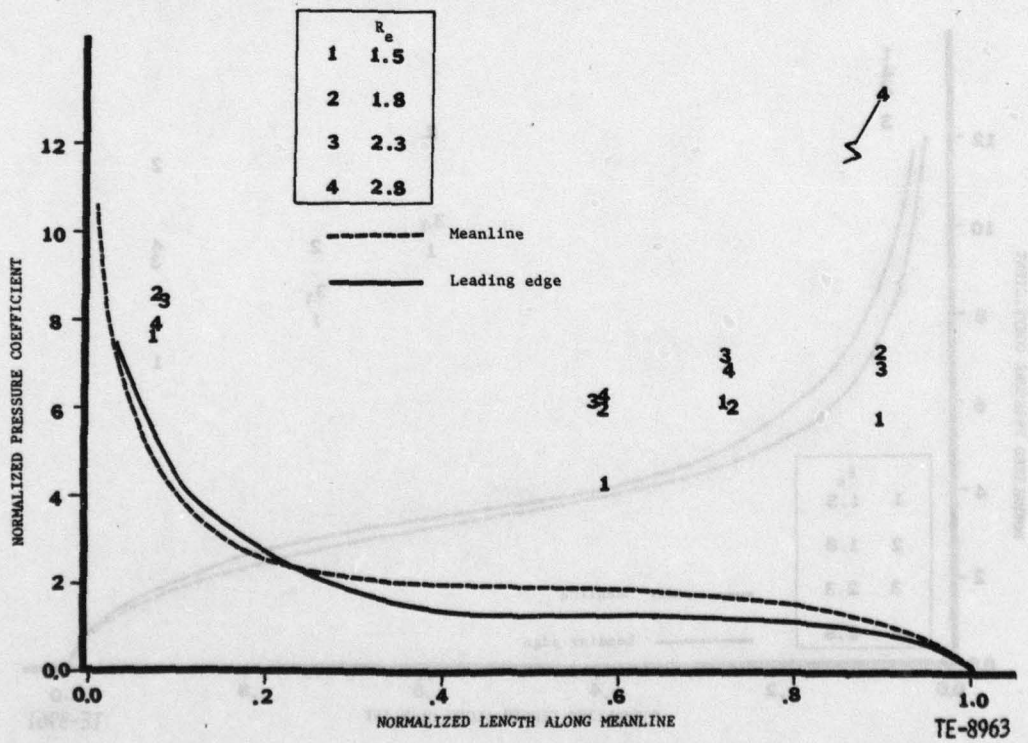


Figure 42. Normalized pressure coefficients for 45° interblade phase angle.

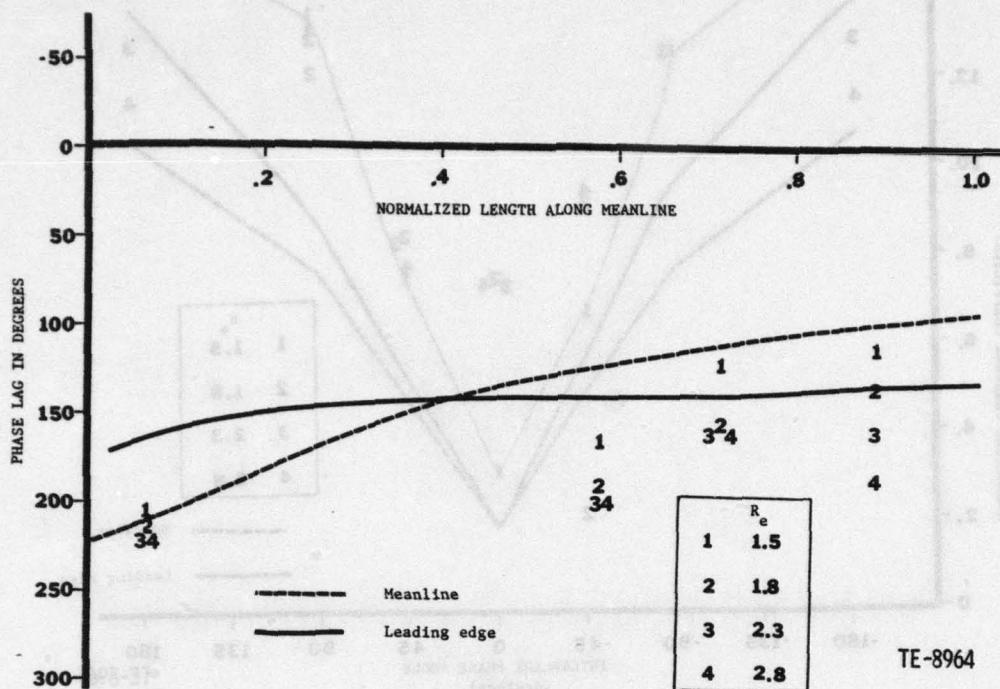


Figure 43. Phase lag for 45° interblade phase angle.

theoretical and experimental results were constructed. Figure 44 presents data acquired at the 8% meanline station. The theory and experimental results yield excellent agreement with regard to trend, but the magnitude of the experimental data is greater than predicted. Note also in this curve the nonalignment of the 1.8 pressure ratio data at a -45° interblade phase angle.

Figure 45 presents the results at the 57.8% meanline station. The experimental data would seem to have a minimum at a slightly negative interblade phase angle. The assumed leading edge cascade indicates a similar behavior, but at a slightly positive interblade phase angle. The meanline cascade model tends to agree with the experimental data in this trend. The magnitude agreement is better, however, with the leading edge cascade model. The data from the 71.2% measuring station reemphasize this trend, as shown in Figure 46. At the most rearward measuring station, 88.5%, a breakdown of even trendwise agreement occurs, as shown in Figure 47. A peak pressure coefficient is seen in the experimental data at approximately +90°, whereas in both analytical models this peak occurs at 180° interblade phase angle. This plot also reflects the effects of expansion ratio. The data obtained experimentally at the 2.8 expansion ratio are clearly influenced

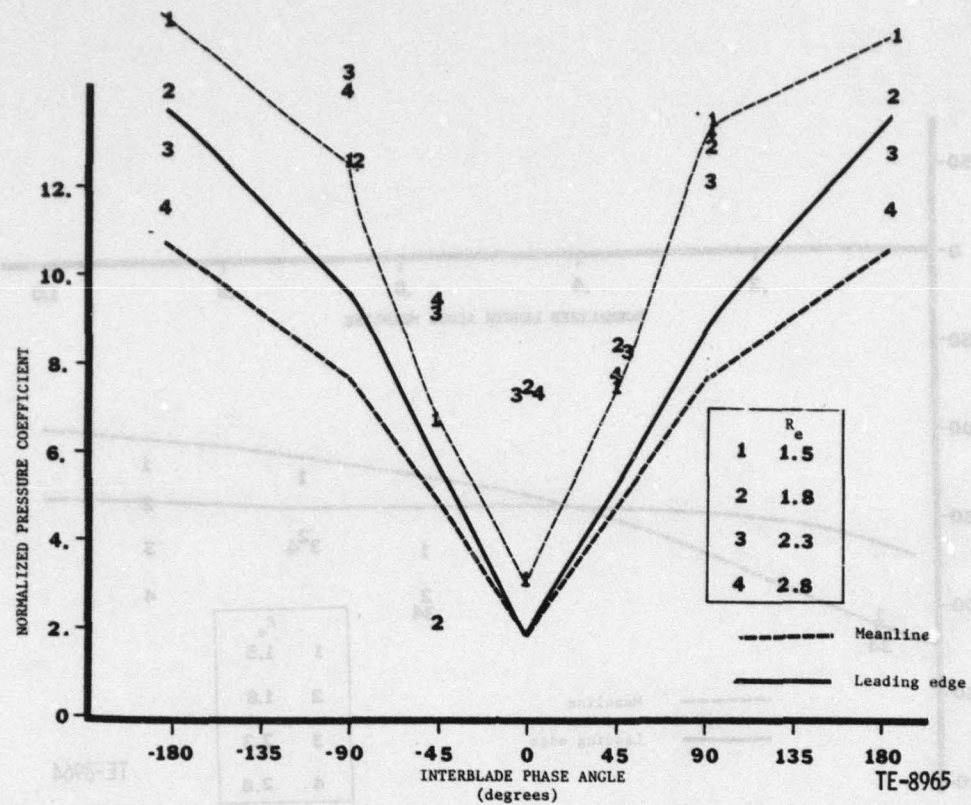


Figure 44. Normalized pressure as a function of interblade phase angle at 8% meanline station.

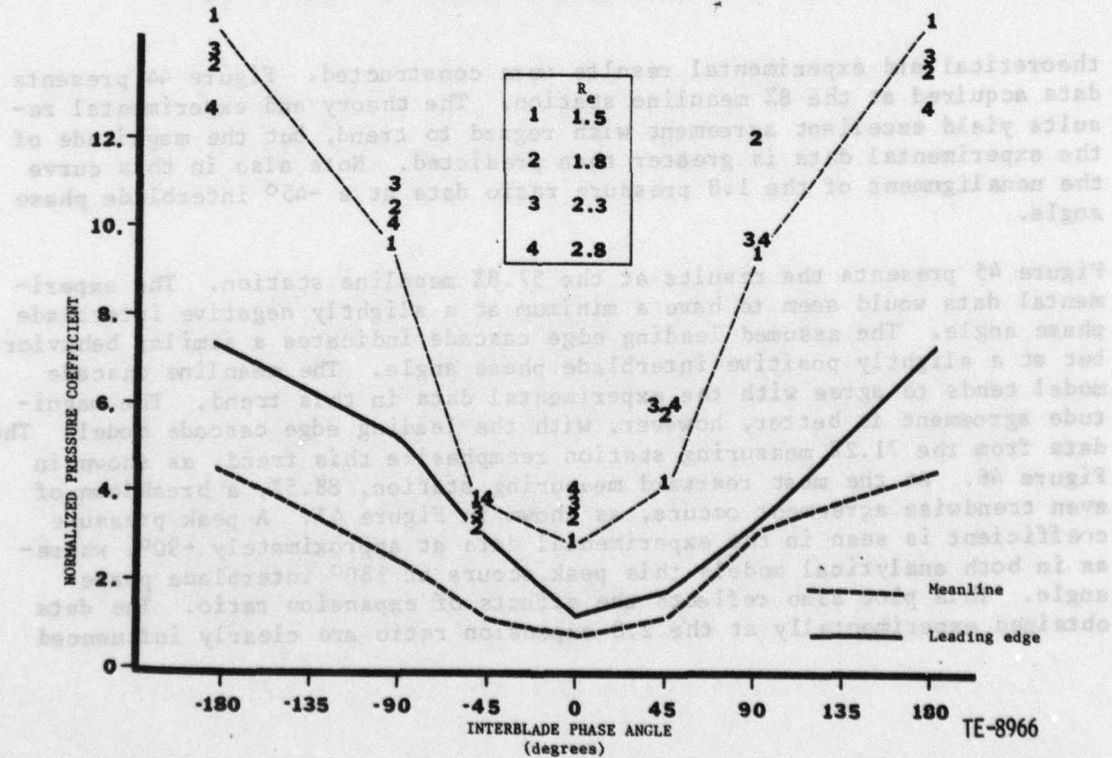


Figure 45. Normalized pressure as a function of interblade phase angle at 57.8% meanline station.

by some phenomenon not present at the other expansion ratios—namely, shock interference from the adjacent airfoil.

Throughout these last four data presentations (Figures 44, 45, 46, and 47) the data from the 1.8 expansion ratio results have not been singled out for comment. At the 8% and 57.8% meanline stations, Figures 44 and 45 indicate that these data agree with the trend of the rest of the experimental data except for the  $-45^\circ$  interblade phase angle point at the 8% station, as discussed. At the two rearward stations, however, the 1.8 expansion ratio data indicate two peaks in the normalized pressure coefficient. The first of these occurs at an interblade phase angle of  $-90^\circ$ , the second at  $+90^\circ$ . The minimum value occurs at a phase angle of  $180^\circ$ , in opposition to trends of the experimental and theoretical results discussed previously.

This behavior at the 1.8 expansion ratio has not been explained to date, yet agreement of the data at the first two measuring stations with data from other expansion ratios would indicate no external influence on the cascade. Thus, the change in behavior must be concluded to be brought about solely by loading effects, a sonic exit occurring at the 1.8 expansion ratio.

The disagreement in pressure coefficient magnitude between the analytical and experimental data was of concern. To generate additional insight into

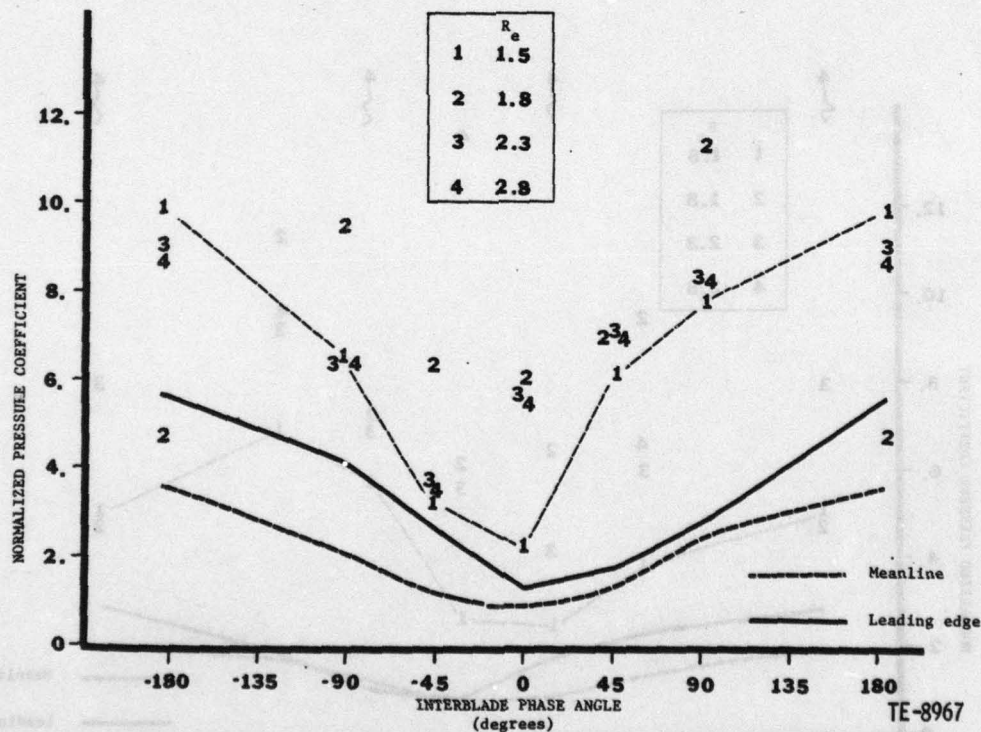


Figure 46. Normalized pressure as a function of interblade phase angle at 71.2% meanline station.

this disparity, the quasi-static results and the dynamic data acquired at  $0^\circ$  interblade phase angle at expansion ratios of 1.5 and 2.8 were compared. Figures 48, 49, 50, and 51 present these comparisons of normalized pressure which have been ratioed to yield a value of 1.0 for the maximum normalized pressure coefficient. Agreement on the suction surface between the dynamic and quasi-static data is outstanding, as shown in Figure 48 and 49. The overall shape of the quasi-static curve is duplicated by the dynamic data results, even at the trailing edge for the 2.8 expansion ratio. Loss of the No. 2 pressure surface transducer made it necessary to normalize the dynamic data to match the quasi-static results at the No. 1 transducer location and in this manner compare the results. Although the convincing totality of the data is not as great as that from the suction surface, Figures 50 and 51 demonstrate that agreement over the forward and aft portions of the pressure surface is good and trendwise correct. The actual quasi-static pressure amplitudes were higher than the time-variant amplitudes, but the trendwise agreement between the quasi-static and dynamic results indicates a relationship between the steady and time-variant aerodynamic fields. Hence, the implication is that to describe the time-variant field adequately, the steady field effects must be properly defined.

The experimentally measured phase lag trends at a 1.5 expansion ratio were compared with the analytical predictions. Figures 52, 53, 54, and 55 are presentations of these comparisons at the instrumented meanline positions.

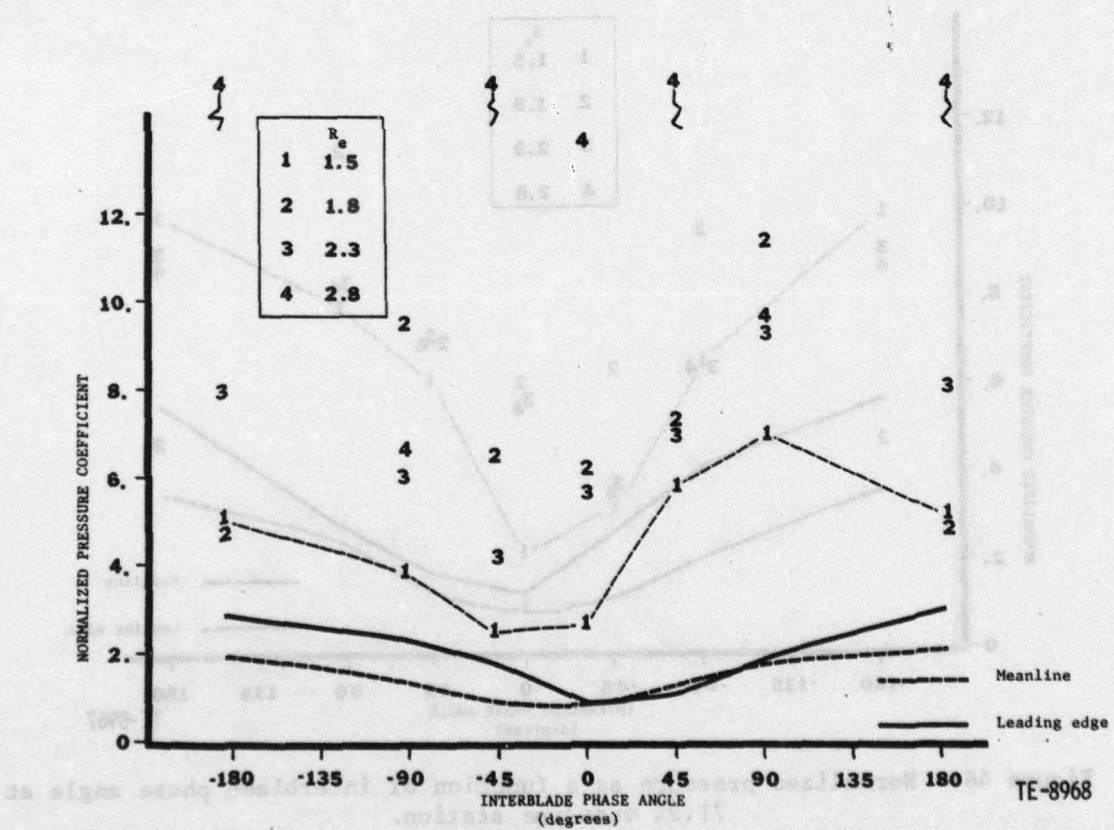


Figure 47. Normalized pressure as a function of interblade phase angle at 88.5% meanline station.

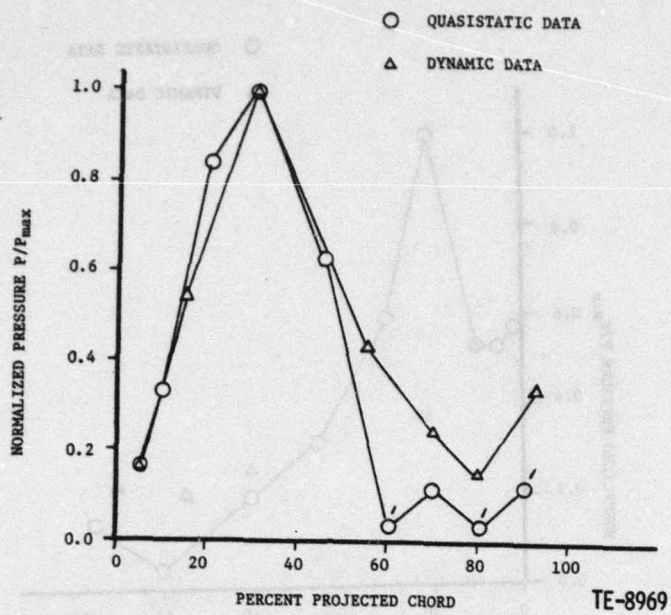


Figure 48. Comparison of quasi-static and dynamic data on suction surface,  
 $R_e = 1.5$ .

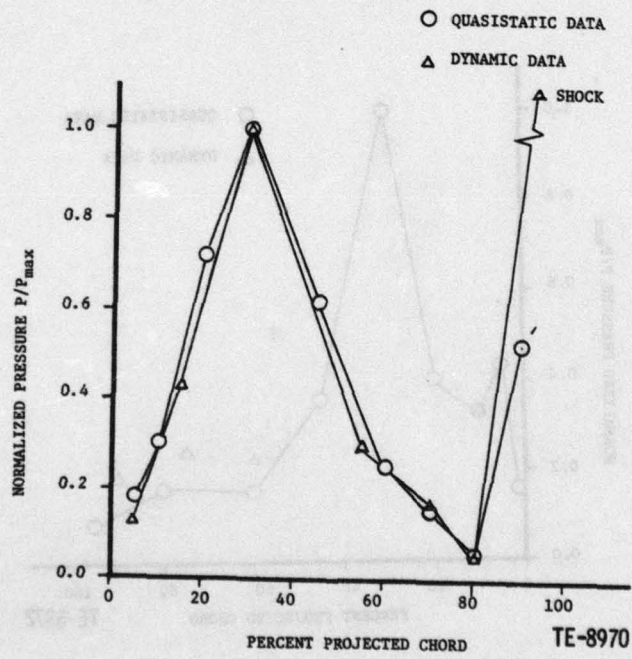


Figure 49. Comparison of quasi-static and dynamic data on suction surface,  
 $R_e = 2.8$ .

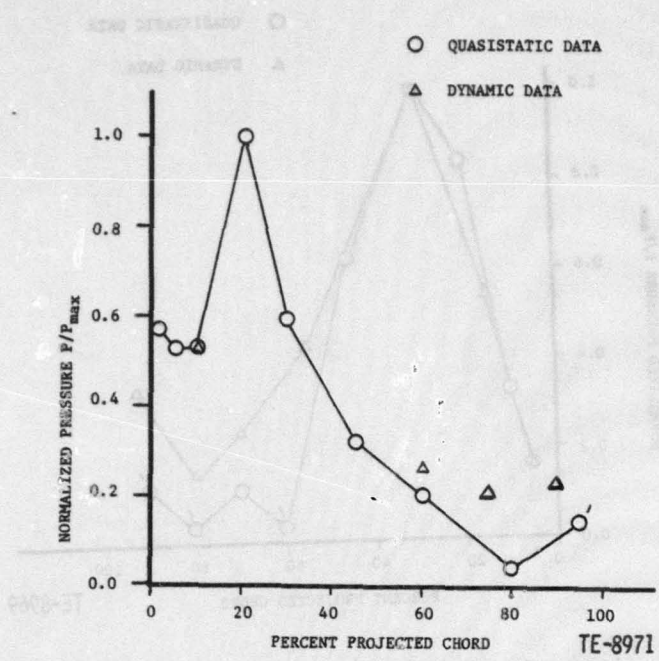


Figure 50. Comparison of quasi-static and dynamic data on pressure surface,  $R_e = 1.5$ .

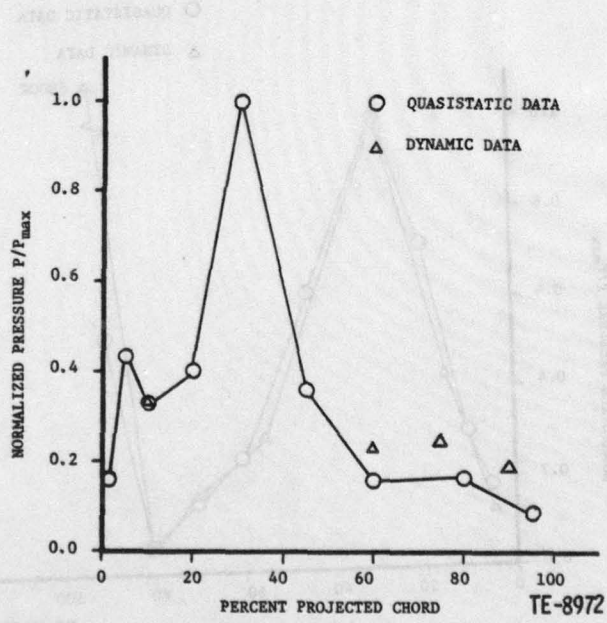


Figure 51. Comparison of quasi-static and dynamic data on pressure surface,  $R_e = 2.8$ .

Figure 52 is a plot of the data acquired at the 8% meanline position and the meanline and leading edge cascade results. In this curve, the experimental data seems to follow the meanline cascade predictions more closely. Also of interest is the asymmetry in phase lag resultant from the cascade assumptions.

Figure 53 presents the results obtained at the 57.8% meanline station. The experimental data do not clearly favor one predictive method over the other. The experimental data at the 71.2% meanline station in Figure 54 exhibit a trend similar to the experimental data at the 88.5% station of Figure 55. Minimum phase lags occur in the  $45^\circ$  to  $90^\circ$  interblade phase angle range, and maximum phase lag occurs in the  $-45^\circ$  to  $-90^\circ$  interblade phase angle range. The shape of these experimental curves more closely resemble those of the results from the meanline cascade. The minimum phase lag occurs at  $0^\circ$  interblade phasing for both analytical models, which does not agree with the experimental results.

The absolute magnitude and trend agreement between the experimental and analytical indicates a basic adequacy of the analytical tools, provided calibration is performed. The disagreement in location (relative to interblade phase angle) of the minimum phase lag appears to arise from the obvious violations in the assumed flow field used in the analytical calculations.

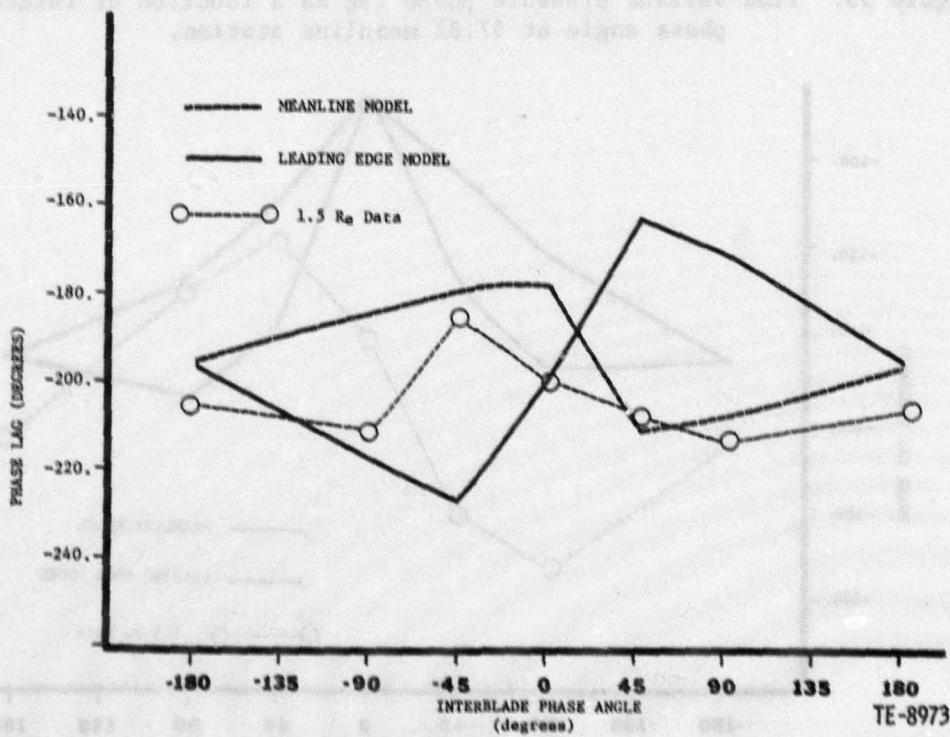


Figure 52. Time-variant pressure phase lag as a function of interblade phase angle at 8% meanline station.

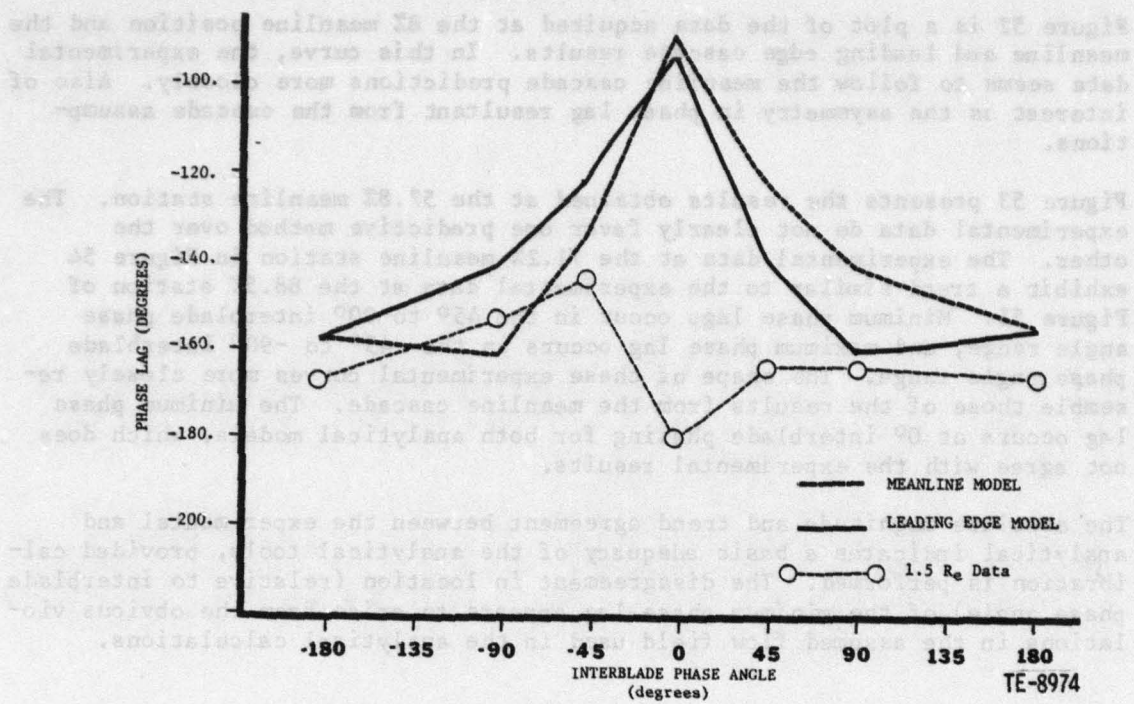


Figure 53. Time-variant pressure phase lag as a function of interblade phase angle at 57.8% meanline station.

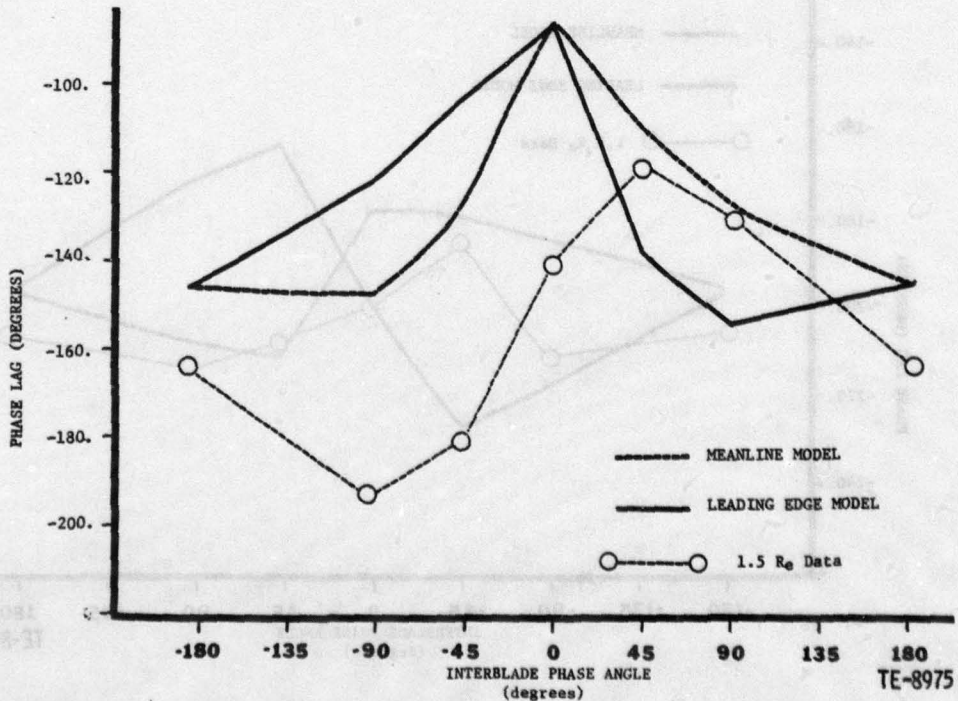


Figure 54. Time-variant pressure phase lag as a function of interblade phase angle at 71.2% meanline station.

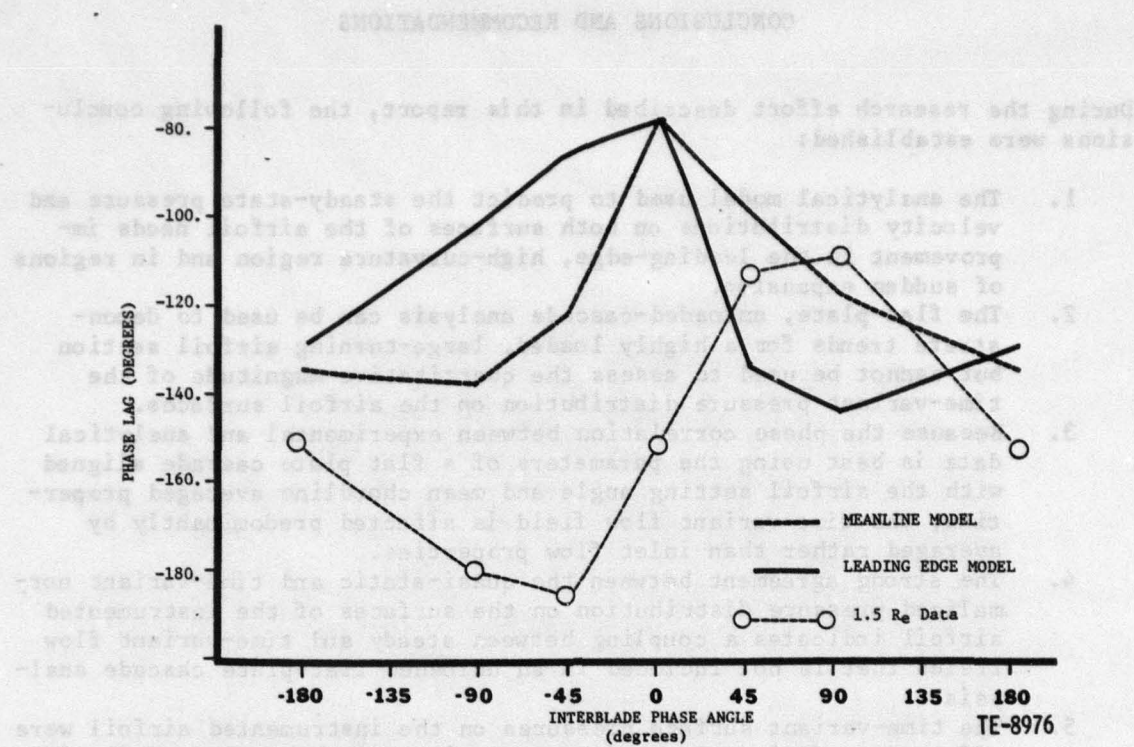


Figure 55. Time-variant pressure phase lag as a function of interblade phase angle at 88.5% meanline station.

## CONCLUSIONS AND RECOMMENDATIONS

During the research effort described in this report, the following conclusions were established:

1. The analytical model used to predict the steady-state pressure and velocity distributions on both surfaces of the airfoil needs improvement in the leading-edge, high-curvature region and in regions of sudden expansion.
2. The flat-plate, unloaded-cascade analysis can be used to demonstrate trends for a highly loaded, large-turning airfoil section but cannot be used to assess the quantitative magnitude of the time-variant pressure distribution on the airfoil surfaces.
3. Because the phase correlation between experimental and analytical data is best using the parameters of a flat plate cascade aligned with the airfoil setting angle and mean chordline averaged properties, the time-variant flow field is affected predominantly by averaged rather than inlet flow properties.
4. The strong agreement between the quasi-static and time-variant normalized pressure distribution on the surfaces of the instrumented airfoil indicates a coupling between steady and time-variant flow fields that is not included in an unloaded flat-plate cascade analysis.
5. The time-variant surface pressures on the instrumented airfoil were affected predominantly by its own motion and the motion of the immediately adjacent airfoils. In view of this conclusion, the airfoils affecting the quasi-static field of the instrumented airfoil should be the immediately adjacent ones.

These conclusions are submitted in response to the results of the experimental program and the attempts to provide experimentally based data for correlation of time-variant analyses.

From the foregoing conclusions and an in-depth study of the experimental and analytical data generated in this program, a number of recommendations become evident:

1. Assess the reasons for lack of agreement in the steady-state analytical and experimental results and develop a series of combined analytical/experimental efforts to document the accuracy of differing analytical formulations.
2. Develop an analytical formulation of the time-variant behavior of highly cambered, thick airfoils operating in a loaded cascade which will include the effects of the steady flow field.
3. Perform a series of experimental investigations to isolate the effects of camber and thickness on the time-variant surface pressures of oscillating airfoils so that adequate data for analytical model development will be obtained.
4. In view of the strong agreement in the form of the normalized pressures in the quasi-static and time-variant portions of this program, perform a series of comparisons of quasi-static and time-variant data at varying interblade phase angles and reduced frequencies. Of interest to examine would be a functional relationship

between the dynamic pressure distributions and reduced frequency, both in trend and actual amplitude.

5. Alter the mode of vibration and/or the location of the torsional axis for the large turning airfoils in order to provide additional, necessary correlation data for analyses, such as those presented by Verdon(24).
6. Investigate an airfoil cascade of less turning to indicate whether quasi-static trends will continue to dominate the time-variant response and to provide further correlation with the flat-plate analysis.

These conclusions and recommendations encompass the entire experimental program and are concerned with the data acquired. These data are unique in that they are the first time-variant data of this nature to be acquired for a cascade of thick, highly cambered airfoils.

REFERENCES

1. Kemp, N. H. and Sears, W. R., "Aerodynamic Interference Between Moving Blade Rows," Journal of the Aeronautical Sciences, Vol 20, No. 9, September 1953.
2. Horlock, J. H., "Fluctuating Lift Forces on Airfoils Moving Through Transverse and Chordwise Gusts," Transactions of the ASME, Journal of Basic Engineering, Vol 90, Series D, No. 4, December 1968.
3. Naumann, H. and Yeh, H., "Lift and Pressure Fluctuations of a Cambered Airfoil Under Periodic Gusts and Applications in Turbomachinery," Transactions of the ASME, Journal of Engineering for Power, Vol 95, Series A, No. 1, January 1973, pp 1-10.
4. Goldstein, M. E. and Atassi, H., "A Complete Second-Order Theory for the Unsteady Flow About an Airfoil Due to a Periodic Gust," Journal of Fluid Mechanics, Vol 74, 1976.
5. Whitehead, D. S., Force and Moment Coefficients for Vibrating Airfoils in Cascade, Aeronautical Research Council R and M 3254, February 1960.
6. Smith, S. M., Discrete Frequency Sound Generation in Axial Flow Turbomachines, University of Cambridge, Department of Engineering Report CUED/A-Turbo/TR 29, 1971.
7. Henderson, R. E. and Daneshyar, H., Theoretical Analysis of Fluctuating Lift on the Rotor of an Axial Turbomachine, Aeronautical Research Council R and M 3684, September 1970.
8. Henderson, R. E. and Horlock, J. H., "An Approximate Analysis of the Unsteady Lift on Airfoils in Cascade," Transactions of the ASME, Journal of Engineering for Power, October 1972.
9. Commerford, G. L. and Carta, F. O., "Unsteady Aerodynamic Response of a Two-Dimensional Airfoil at High Reduced Frequency," AIAA Journal, Vol 12, No. 1, 1974.
10. Ostdiek, F. R., A Cascade in Unsteady Flow, Ph.D. Thesis, The Ohio State University, 1975.
11. Henderson, R. E. and Franke, G. F., Investigation of the Unsteady Pressure Distribution on the Blades of an Axial Flow Fan, Final Report, NASA Grant No. NGR 39-009-275, March 1978.
12. Fleeter, S., Novick, A. S., and Riffel, R. E., "The Unsteady Aerodynamic Response of an Airfoil Cascade to a Time-Variant Supersonic Inlet Flow Field," Unsteady Phenomena in Turbomachinery, AGARD-CP-177, 1975.
13. Fleeter, S., Jay, R. L., and Bennett, W. A., Rotor Wake Generated Unsteady Aerodynamic Response of a Compressor Stator, ASME Paper No. 78-GT-112, April 1978.

XEROX 2500A

14. Fleeter, S., Bennett, W. A., and Jay, R. L., "Time-Variant Aerodynamic Measurements in a Research Compressor," Proceedings of the Dynamic Flow Conference 1978, September 1978.
15. Fleeter, S., Jay, R. L., and Bennett, W. A., "Wake Induced Time-Variant Aerodynamics Including Rotor-Stator Axial Spacing Effects," ASME Journal of Non-Steady Fluid Dynamics, December 1978.
16. Fleeter, S., Bennett, W. A., and Jay, R. L., The Time-Variant Response of a Stator Row Including the Effects of Airfoil Camber, ASME Paper No. 79-GT-110, March 1979.
17. Fleeter, S., "Fluctuating Lift and Moment Coefficients for Cascaded Airfoils in a Nonuniform Compressible Flow," AIAA Journal of Aircraft, Vol 10, No. 2, February 1973.
18. Atassi, H. and Akai, T. J., Aerodynamic and Aeroelastic Characteristics of Oscillating Loaded Cascades at Low Mach Number, ASME Paper No. 79-FT-111, March 1979.
19. Carta, F. O. and St. Hilaire, A. O., An Experimental Study on the Aerodynamic Response of a Subsonic Cascade Oscillating Near Stall, ASME Paper No. 77-GT-47.
20. Fleeter, S. and Riffel, R. E., Aerodynamic Phenomena in an Oscillating Transonic MCA Airfoil Cascade Including Loading Effects, AGARD-CP-227, September 1979.
21. Platzer, M. F., Unsteady Flows in Turbomachines - A Review of Recent Developments, AGARD-CP-227, September 1977.
22. Coustou, M., Time Dependent Solution of Euler's Equations to Solve the Transonic Blade to Blade Flow in Turbomachinery, von Karman Institute for Fluid Dynamics, December 1975.
23. Carstens, V., "Unsteady Pressure Distributions on an Oscillating Cascade in Subsonic Flow," Revue Francaise de Mecanique - Numero Special, pp 25-33, 1976.
24. Verdon, J. M. and Caspar, J. R., Subsonic Flow Past an Oscillating Cascade with Finite Mean Flow Deflection, AIAA Paper No. 79-1516, July 1979.

## APPENDIX

### TIME-VARIANT DATA

#### TORSION CASCADE

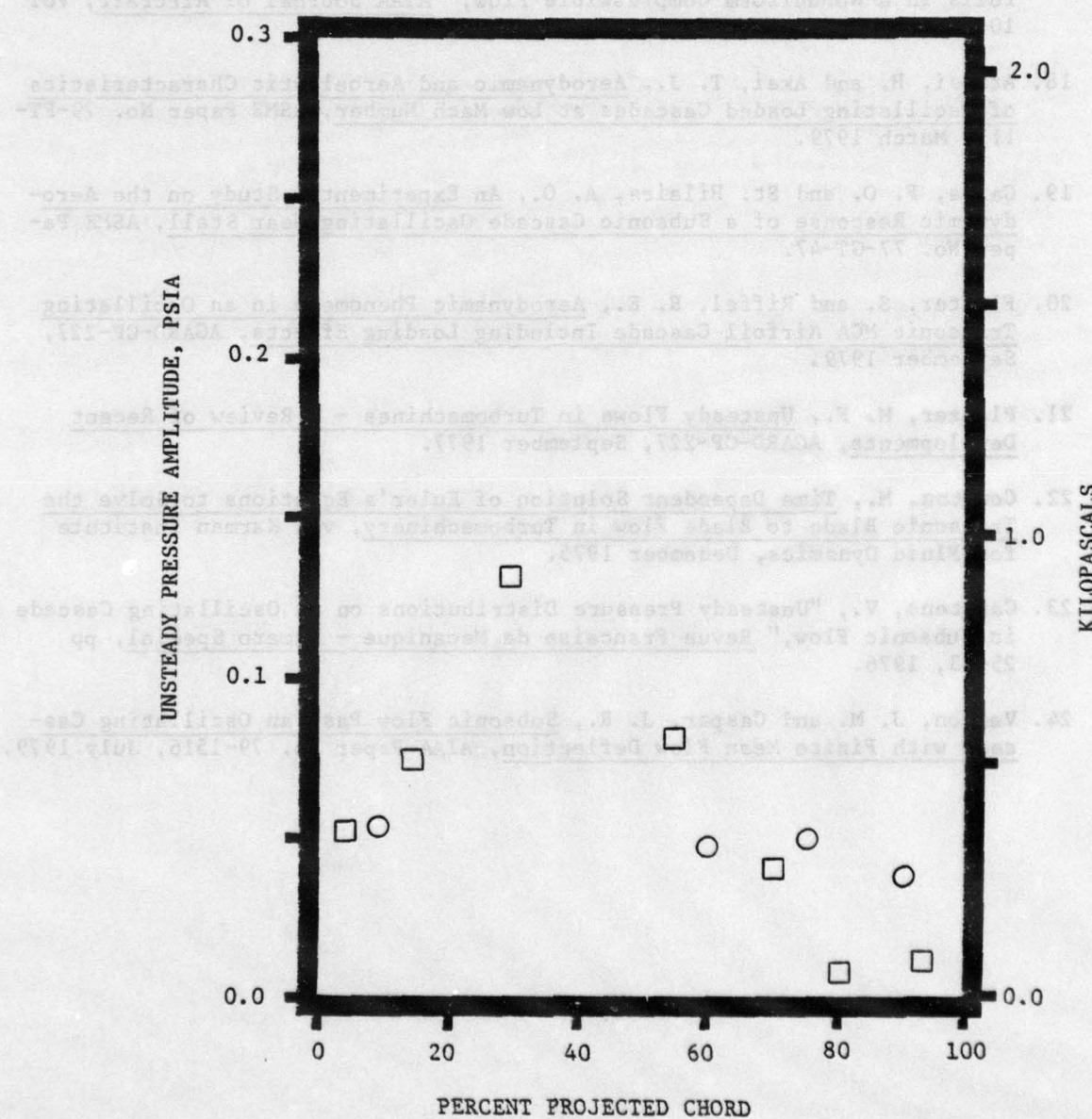
SURFACE PRESSURE AMPLITUDES

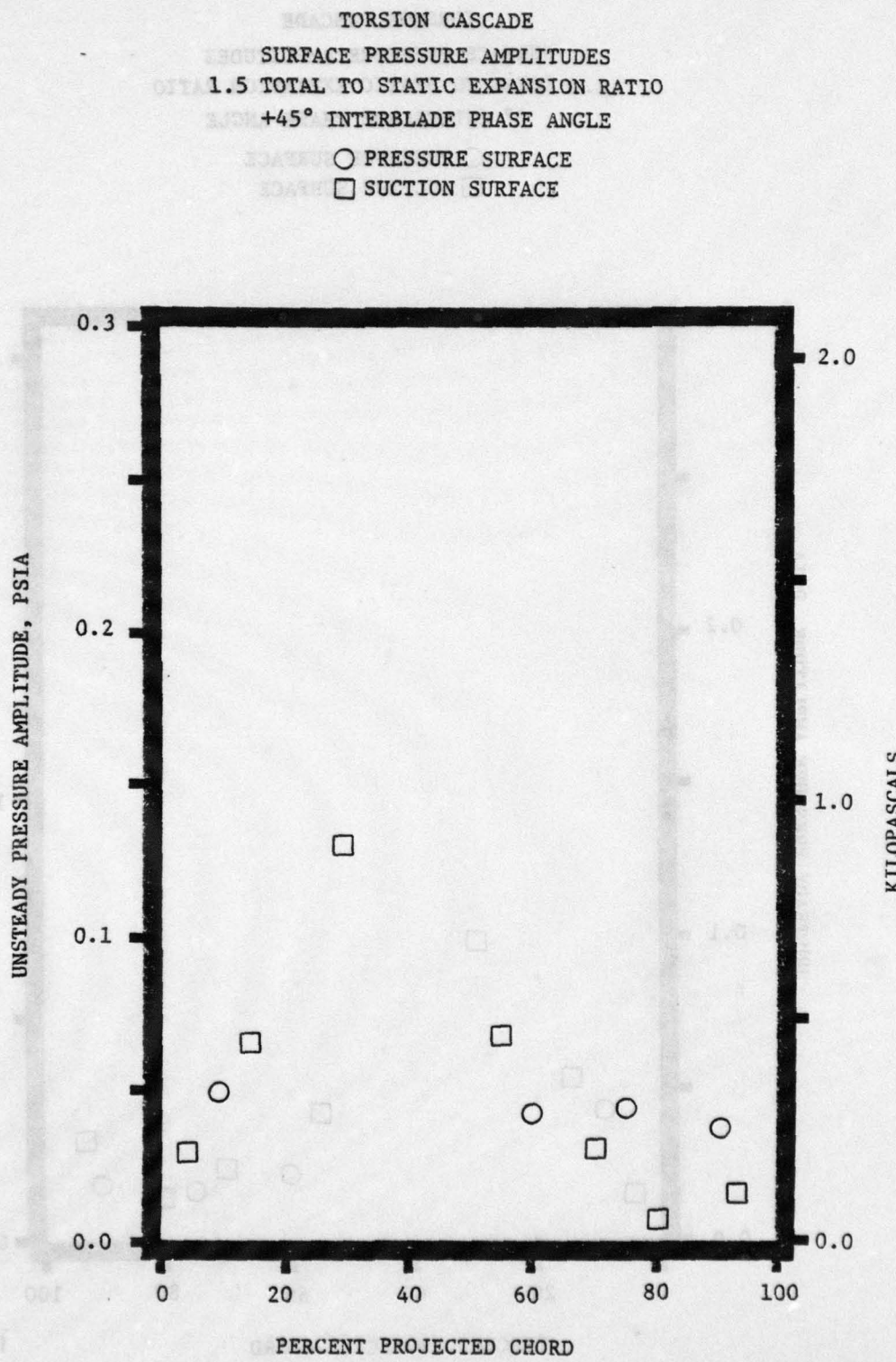
1.5 TOTAL TO STATIC EXPANSION RATIO

+90° INTERBLADE PHASE ANGLE

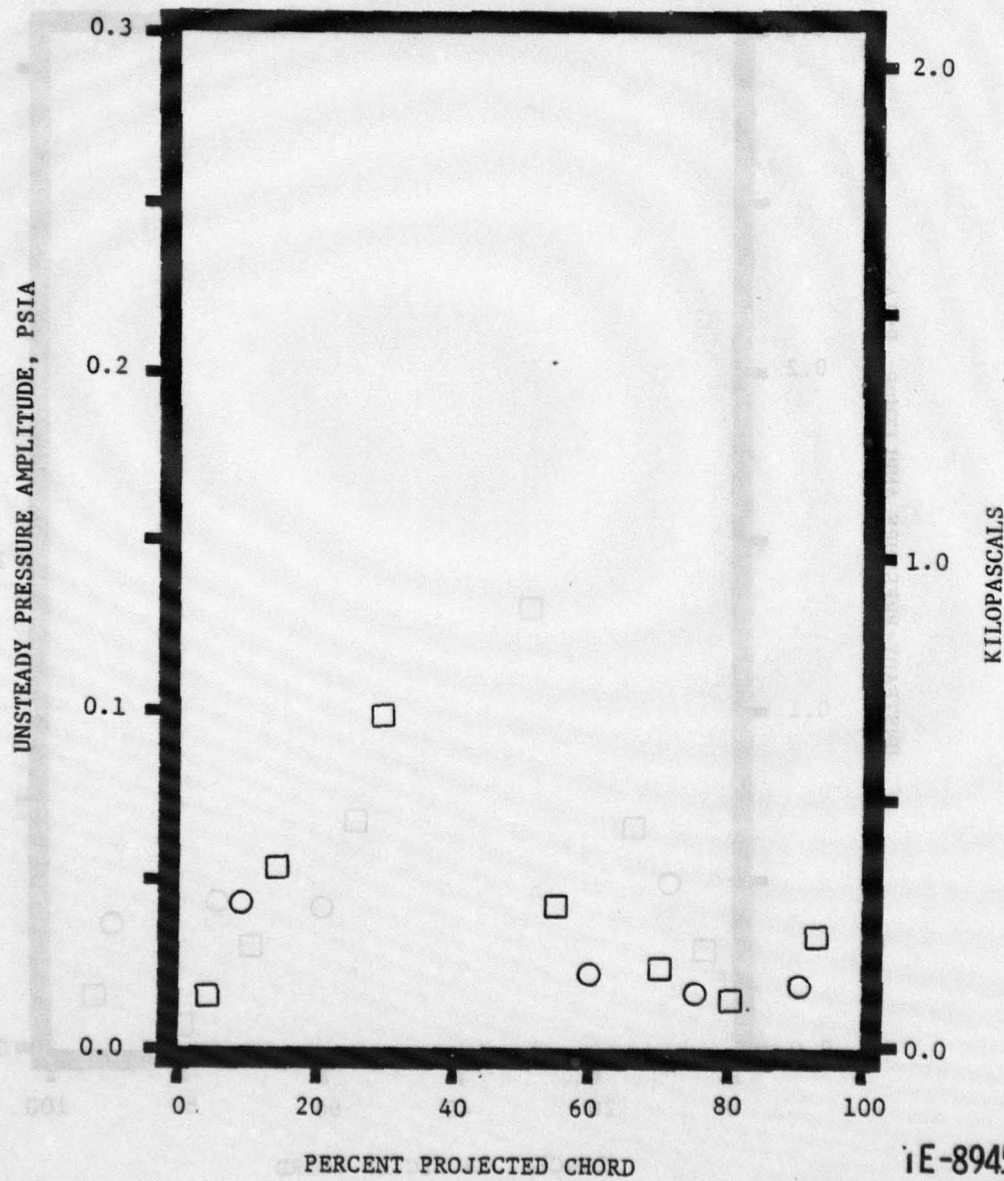
○ PRESSURE SURFACE

□ SUCTION SURFACE

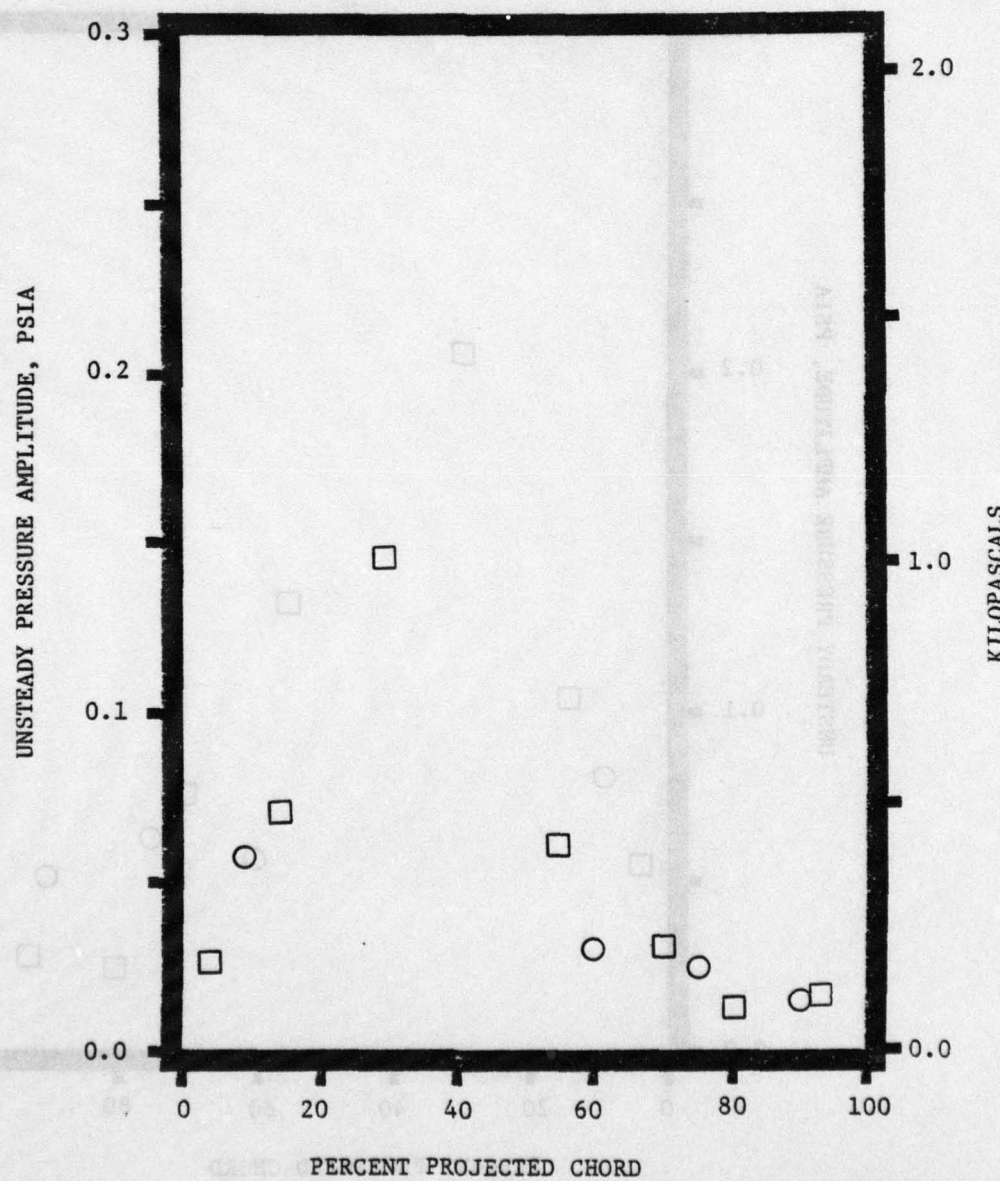




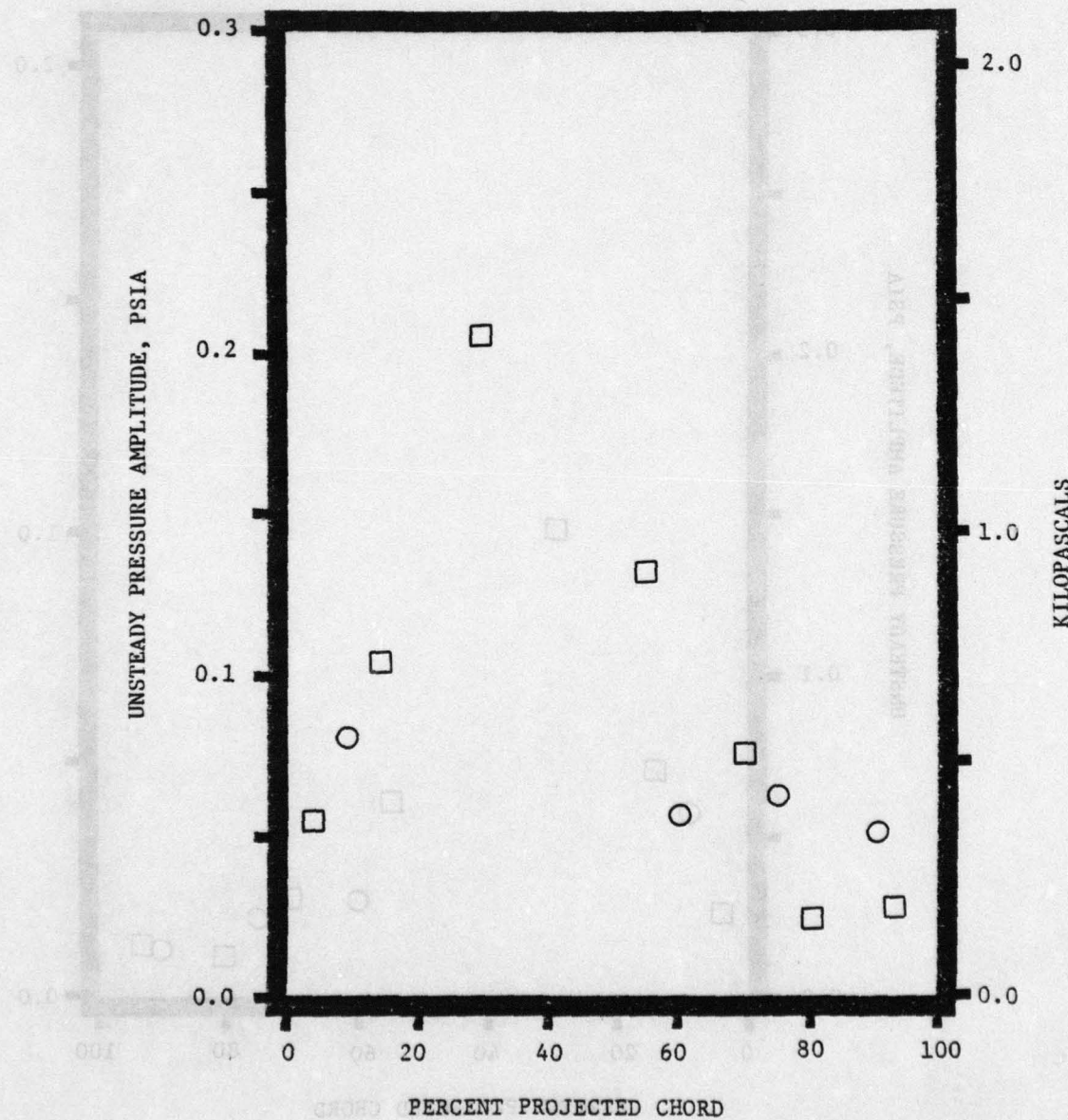
TORSION CASCADE  
SURFACE PRESSURE AMPLITUDES  
1.5 TOTAL TO STATIC EXPANSION RATIO  
0° INTERBLADE PHASE ANGLE  
○ PRESSURE SURFACE  
□ SUCTION SURFACE



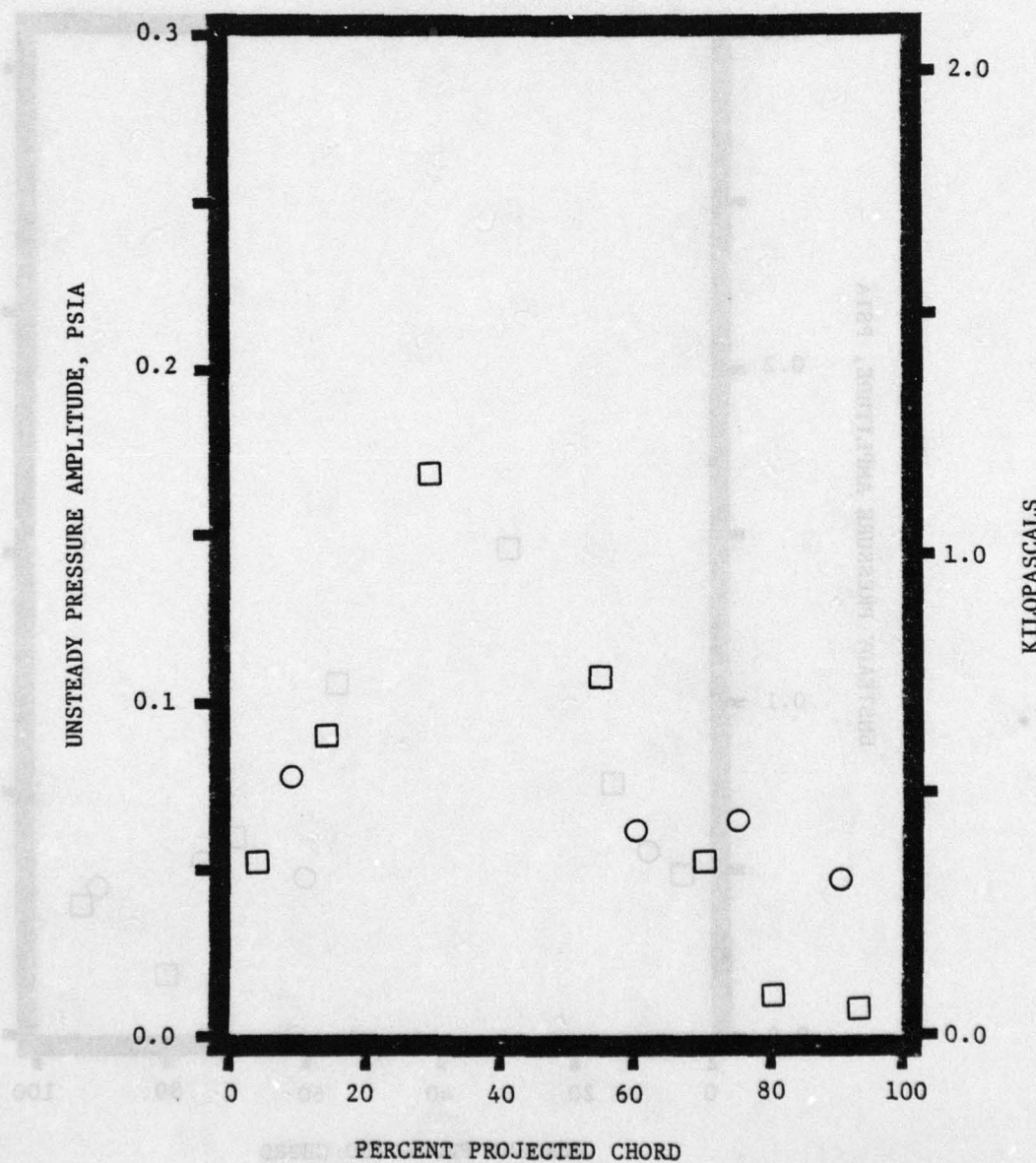
STAGGERED TORSION CASCADE  
EQUILIBRIUM SURFACE PRESSURE AMPLITUDES  
CITAS NO 1.5 TOTAL TO STATIC EXPANSION RATIO  
INTERBLADE PHASE ANGLE -45°  
○ PRESSURE SURFACE  
□ SUCTION SURFACE



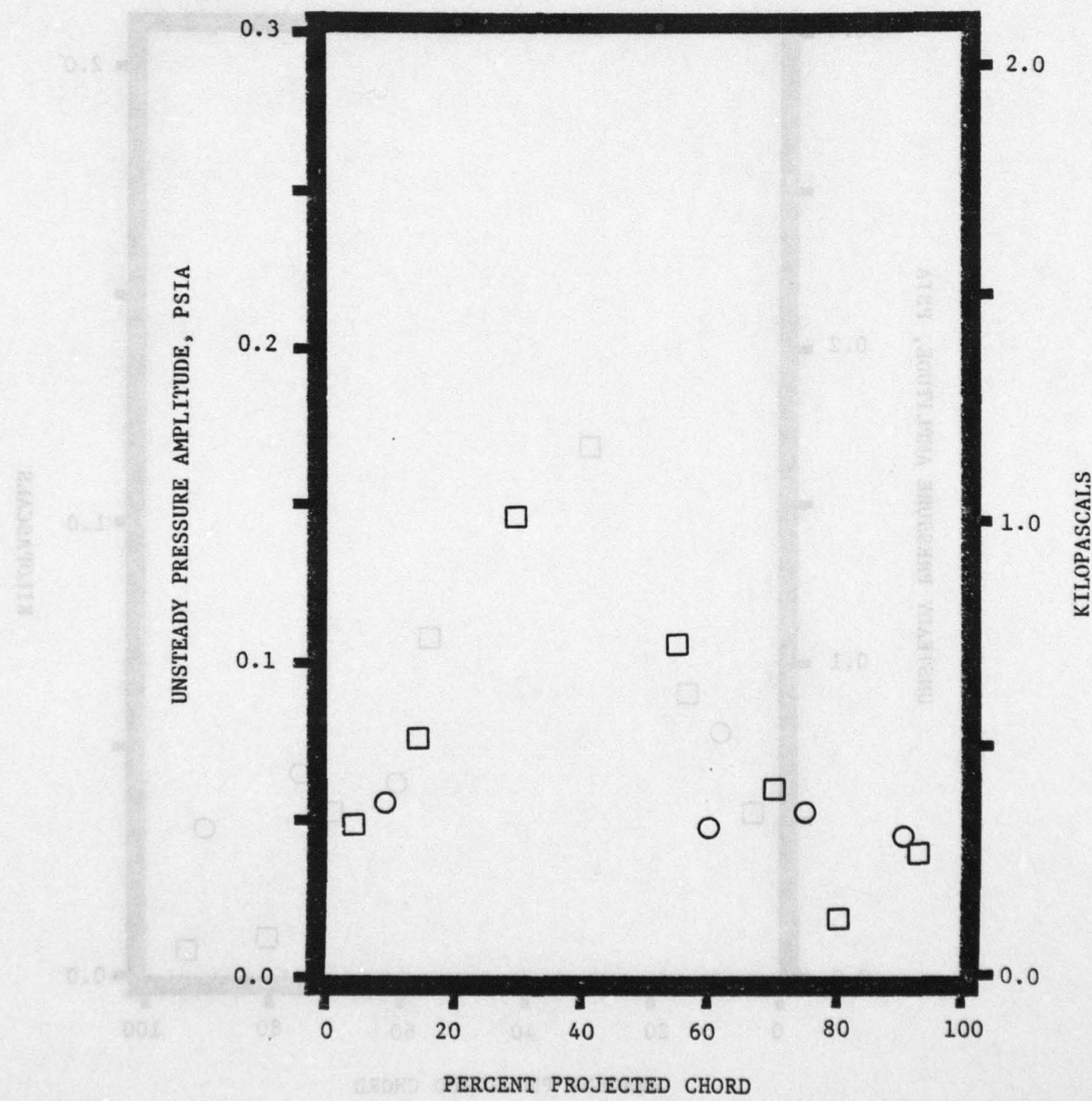
SCALAR TORSION CASCADE  
SURFACE PRESSURE AMPLITUDES  
1.5 TOTAL TO STATIC EXPANSION RATIO  
-90° INTERBLADE PHASE ANGLE  
○ PRESSURE SURFACE  
□ SUCTION SURFACE



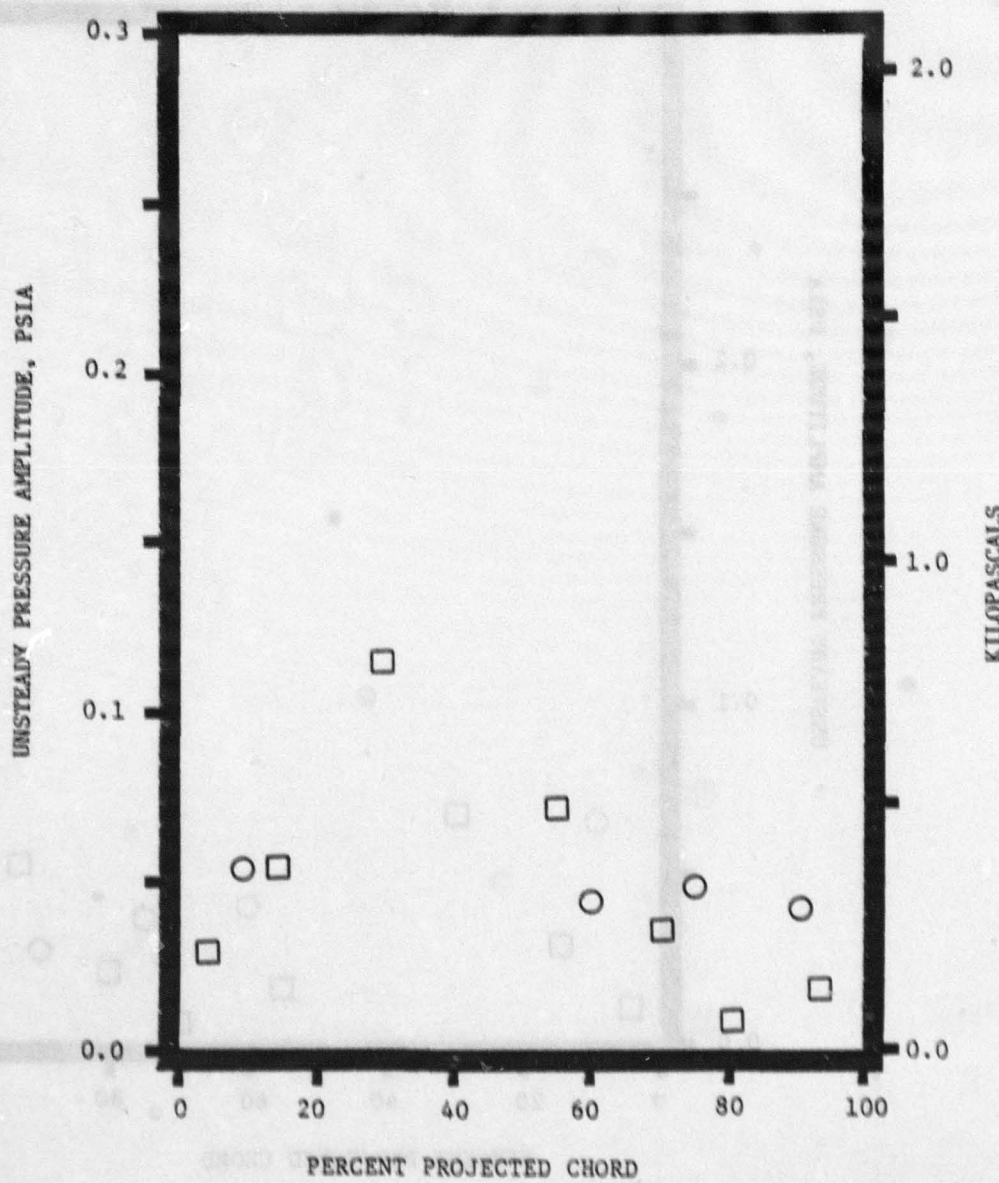
SEAGARD TORSION CASCADE  
SURFACE PRESSURE AMPLITUDES  
1.5 TOTAL TO STATIC EXPANSION RATIO  
180° INTERBLADE PHASE ANGLE  
○ PRESSURE SURFACE  
□ SUCTION SURFACE



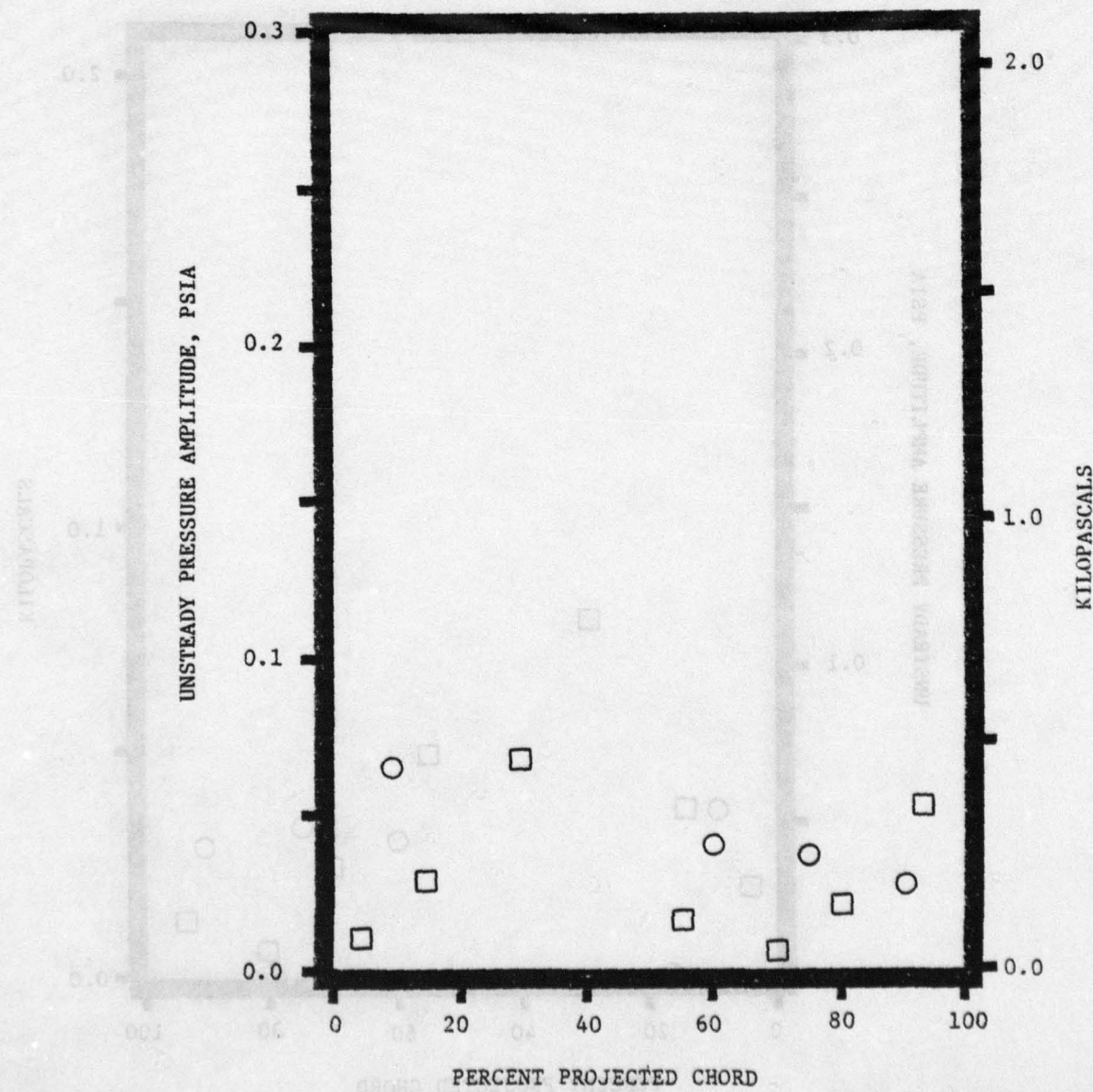
SEAGARD TORSION CASCADE  
SURFACE PRESSURE AMPLITUDES  
1.8 TOTAL TO STATIC EXPANSION RATIO  
+90°INTERBLADE PHASE ANGLE  
○ PRESSURE SURFACE  
□ SUCTION SURFACE

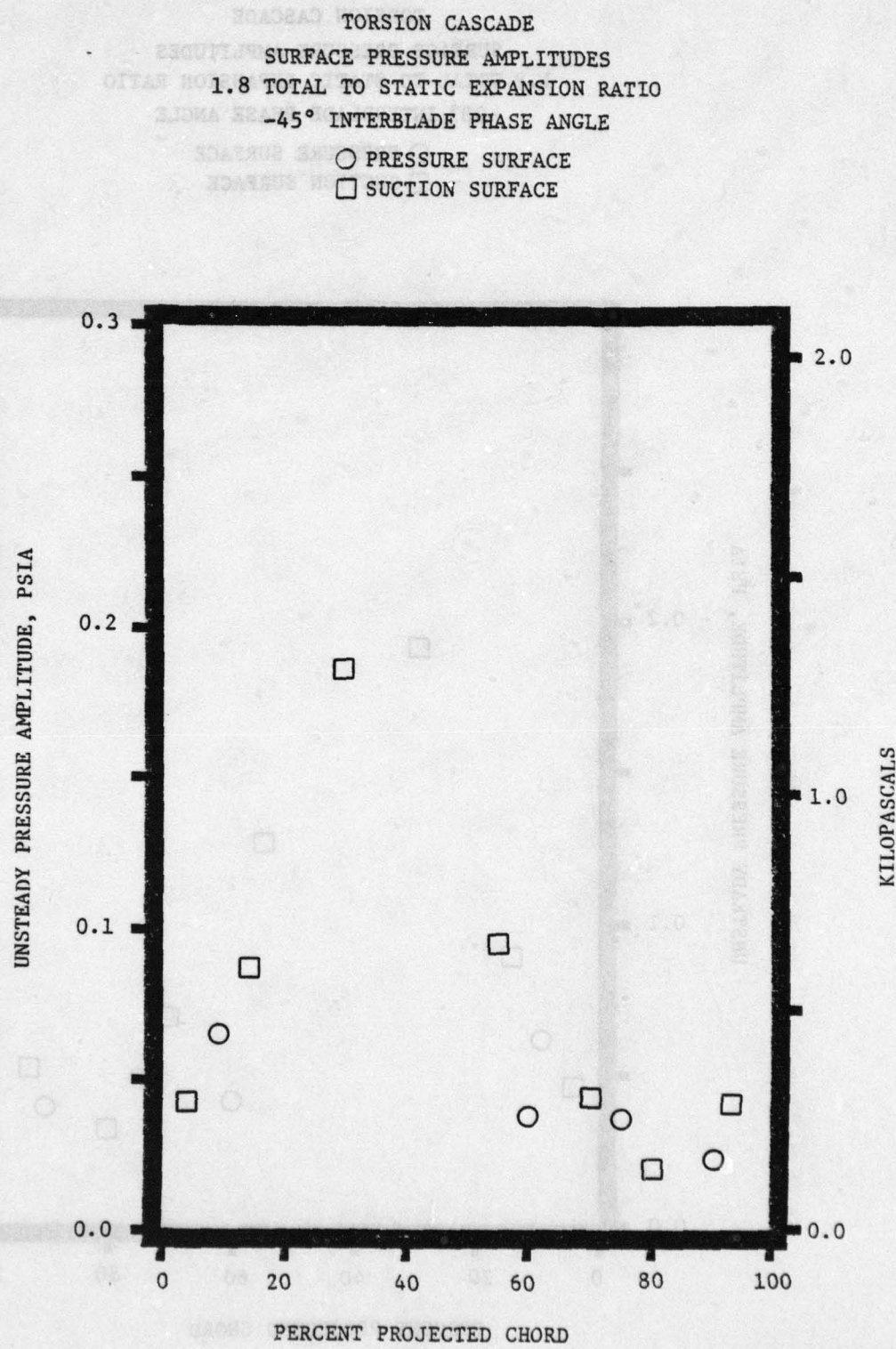


TORSION CASCADE  
SURFACE PRESSURE AMPLITUDES  
1.8 TOTAL TO STATIC EXPANSION RATIO  
 $+45^\circ$  INTERBLADE PHASE ANGLE  
○ PRESSURE SURFACE  
□ SUCTION SURFACE

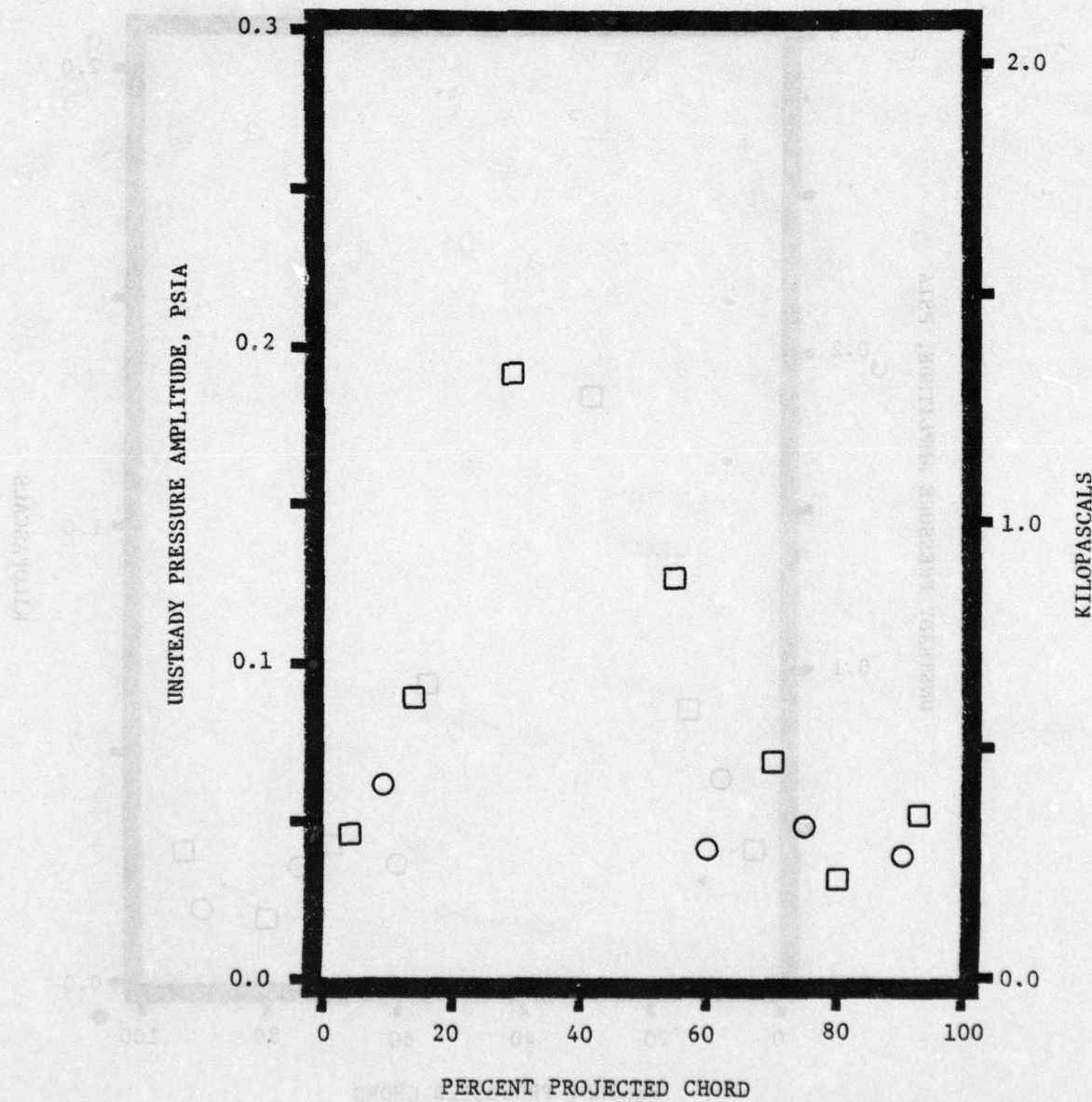


TORSION CASCADE  
SURFACE PRESSURE AMPLITUDES  
1.8 TOTAL TO STATIC EXPANSION RATIO  
0° INTERBLADE PHASE ANGLE  
○ PRESSURE SURFACE  
□ SUCTION SURFACE

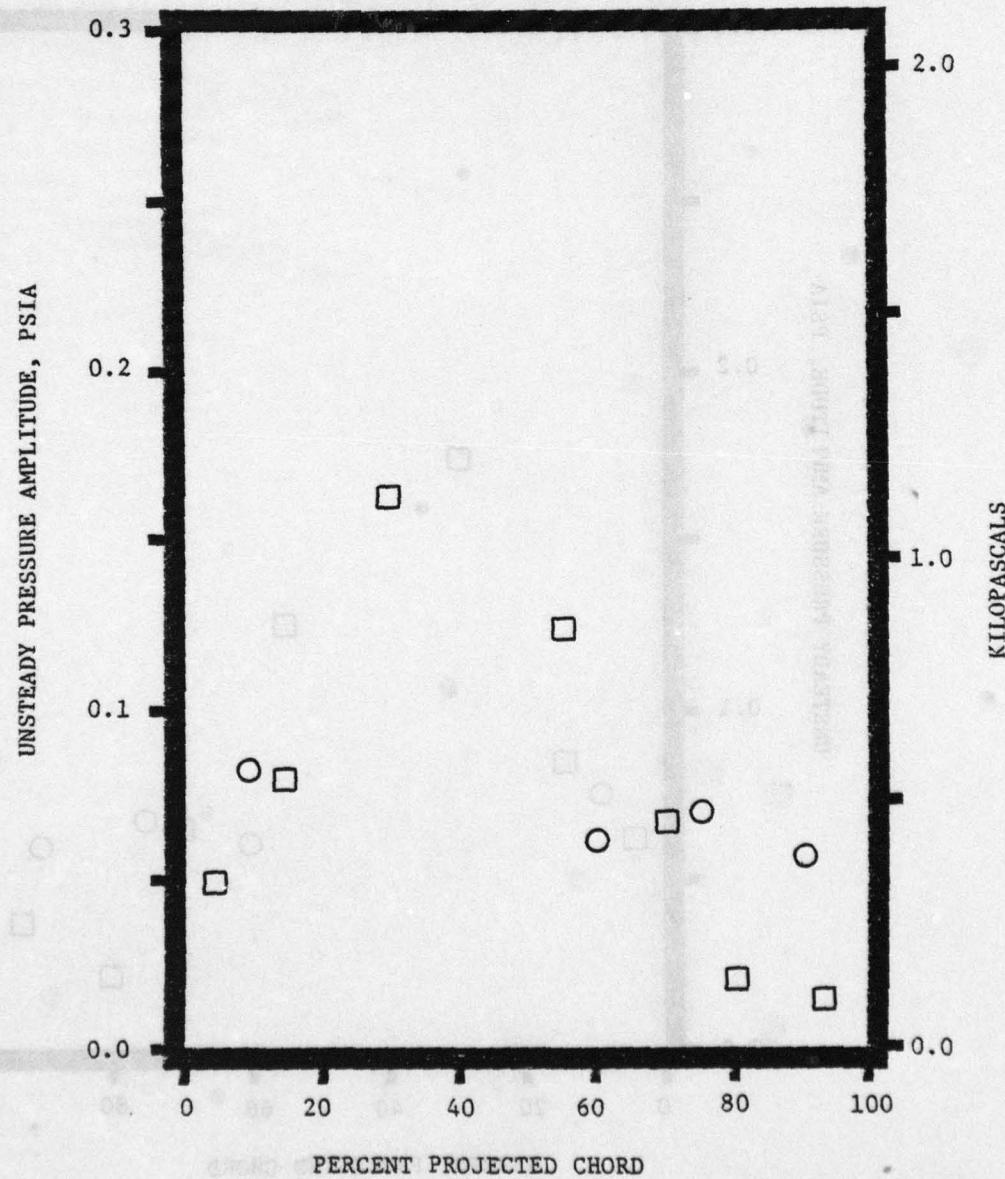




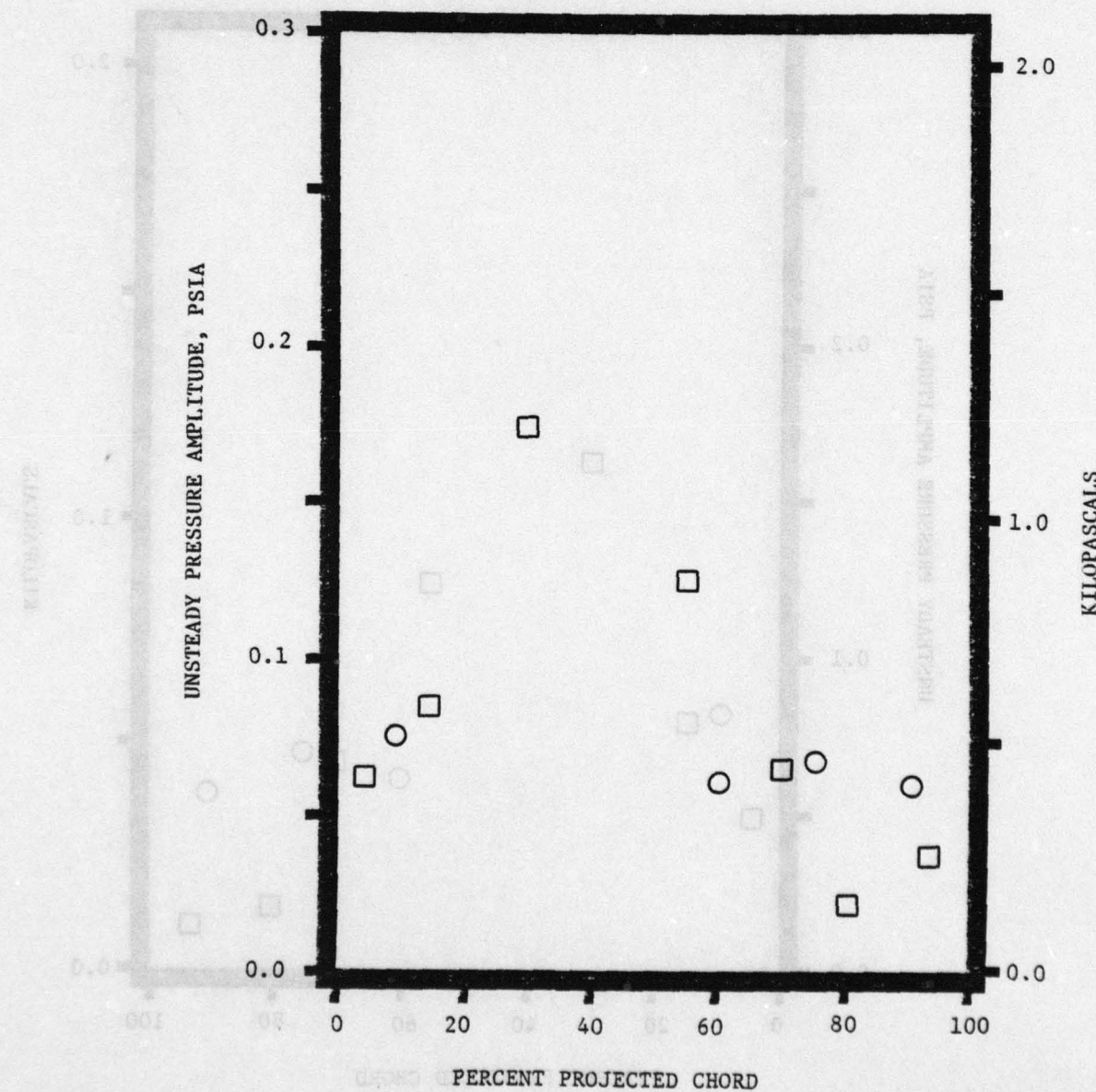
SEASIDE TORSION CASCADE  
SURFACE PRESSURE AMPLITUDES  
1.8 TOTAL TO STATIC EXPANSION RATIO  
-90° INTERBLADE PHASE ANGLE  
○ PRESSURE SURFACE  
□ SUCTION SURFACE



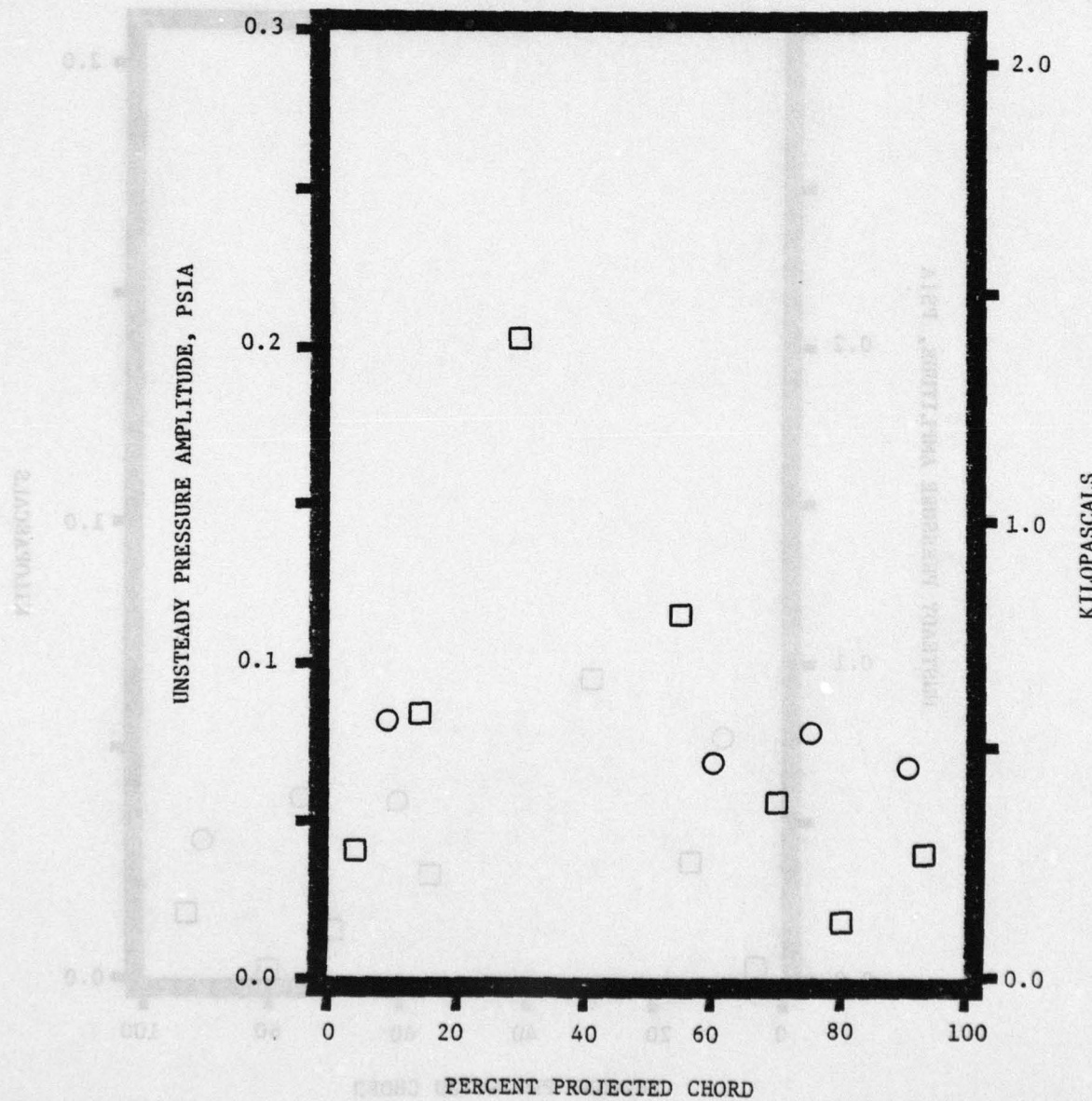
TORSION CASCADE  
SURFACE PRESSURE AMPLITUDES  
1.8 TOTAL TO STATIC EXPANSION RATIO  
180° INTERBLADE PHASE ANGLE  
○ PRESSURE SURFACE  
□ SUCTION SURFACE



TORSION CASCADE  
SURFACE PRESSURE AMPLITUDES  
2.3 TOTAL TO STATIC EXPANSION RATIO  
+90° INTERBLADE PHASE ANGLE  
○ PRESSURE SURFACE  
□ SUCTION SURFACE



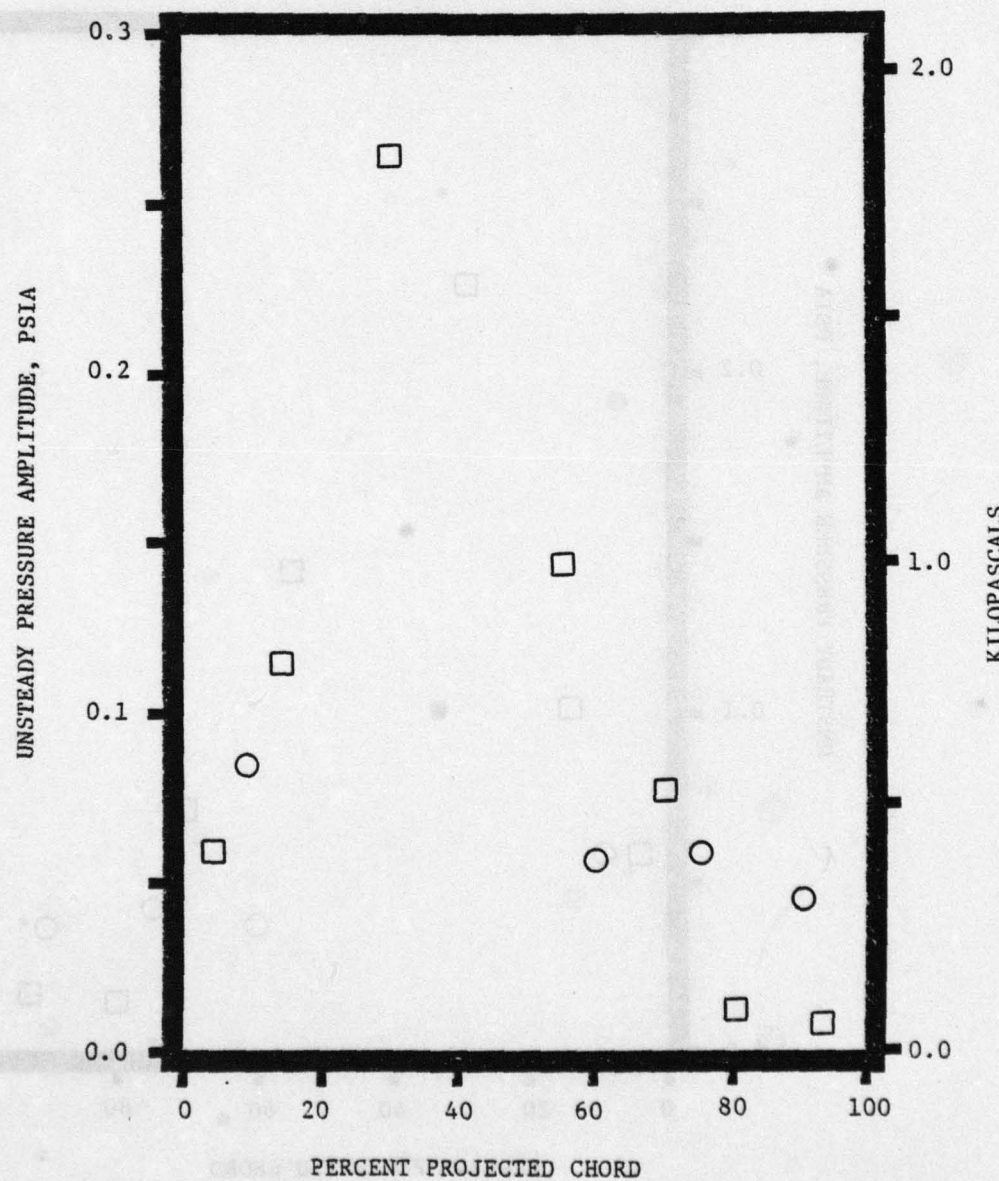
SEALBLADE TORSION CASCADE  
SEALBLADE SURFACE PRESSURE AMPLITUDES  
CITAS NO. 2.3 TOTAL TO STATIC EXPANSION RATIO  
SIGMA = 45° INTERBLADE PHASE ANGLE  
PRESSURE SURFACE ○  
SUCTION SURFACE □



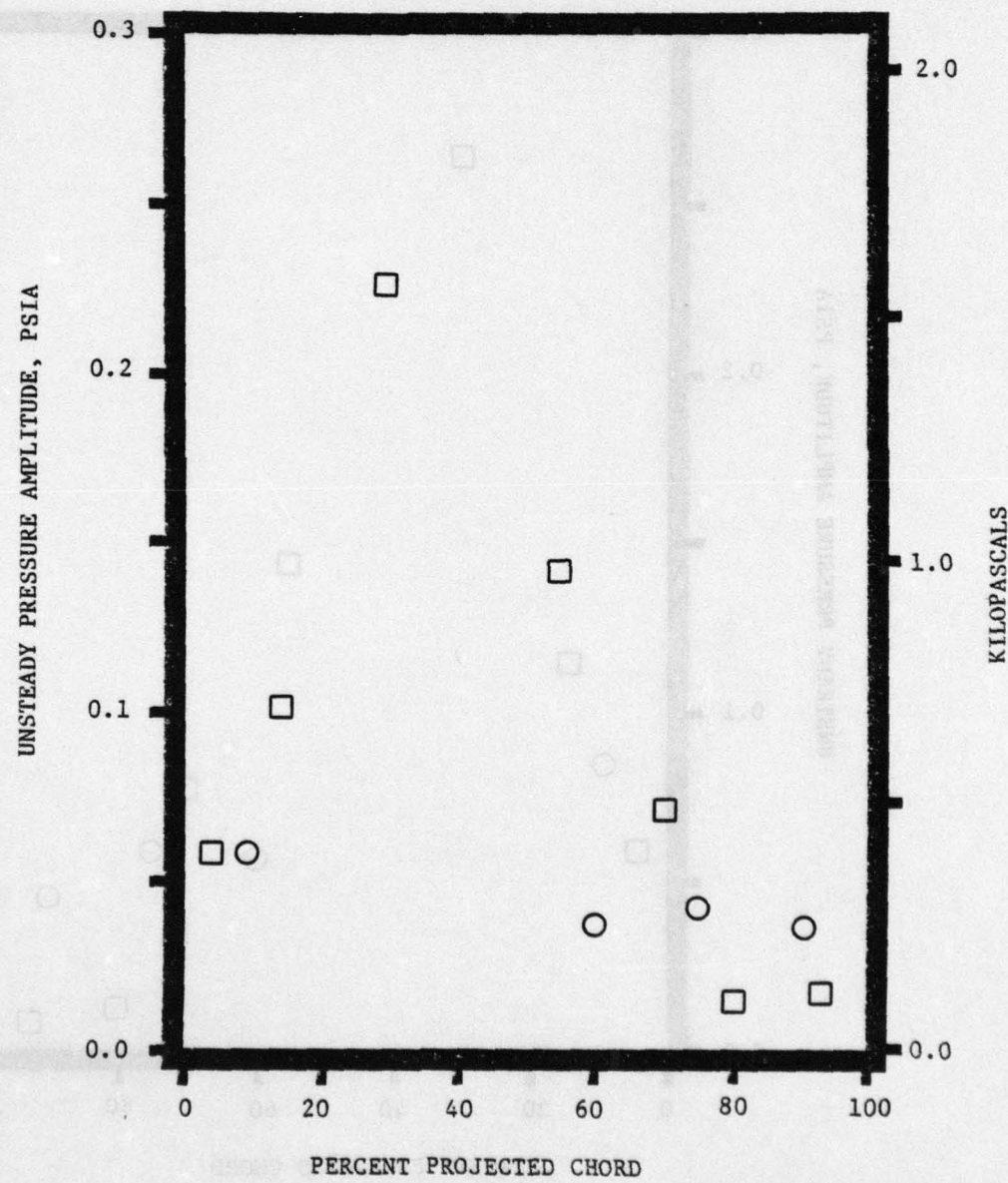
SEADRAKE TORSION CASCADE  
SUCCTION SURFACE PRESSURE AMPLITUDES  
TOTAL NO. 2.3 TOTAL TO STATIC EXPANSION RATIO  
SEEDRAKE 0° INTERBLADE PHASE ANGLE  
○ PRESSURE SURFACE  
□ SUCTION SURFACE



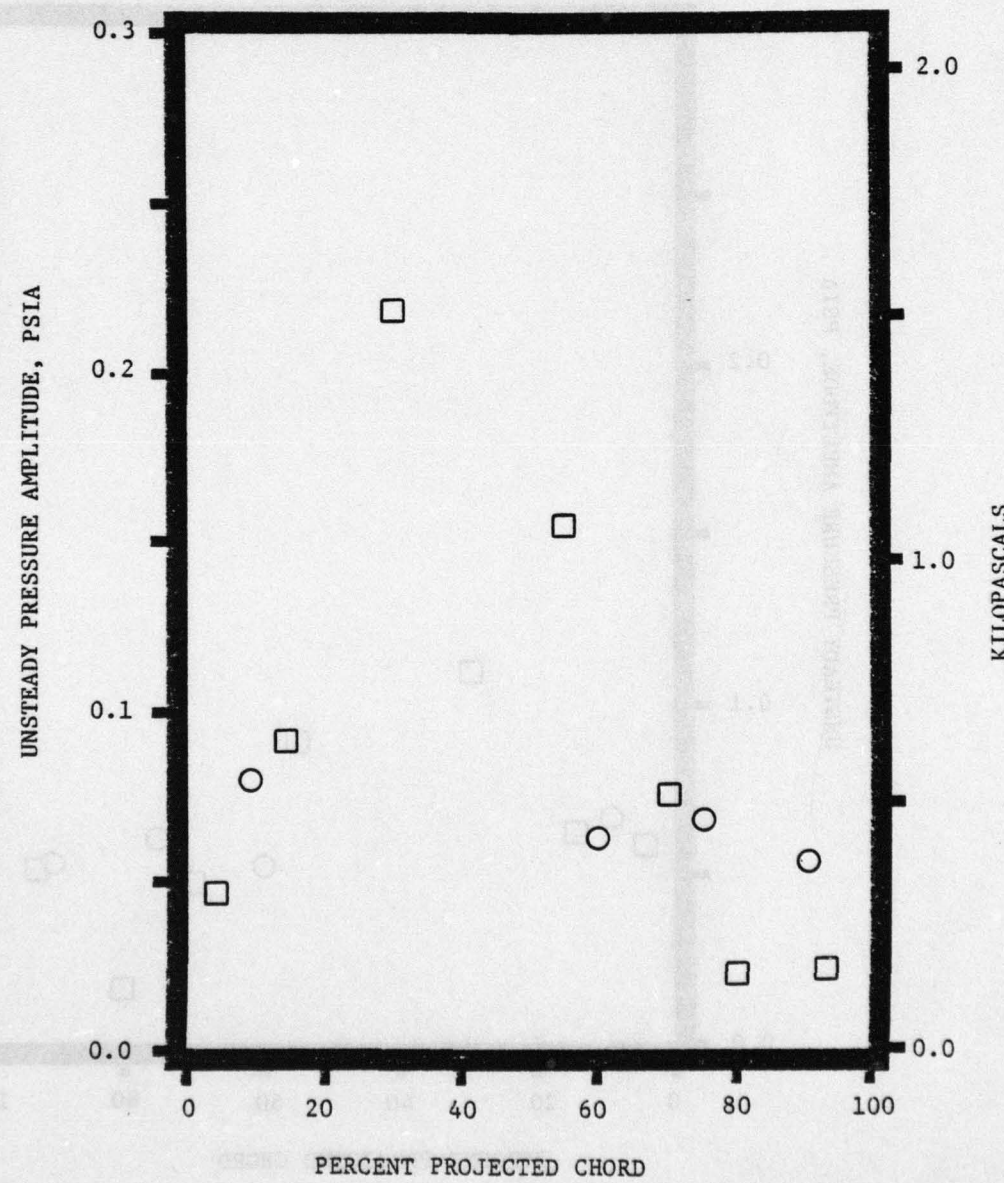
SEASIDE TORSION CASCADE  
SURFACE PRESSURE AMPLITUDES  
2.3 TOTAL TO STATIC EXPANSION RATIO  
 $-45^\circ$  INTERBLADE PHASE ANGLE  
○ PRESSURE SURFACE  
□ SUCTION SURFACE



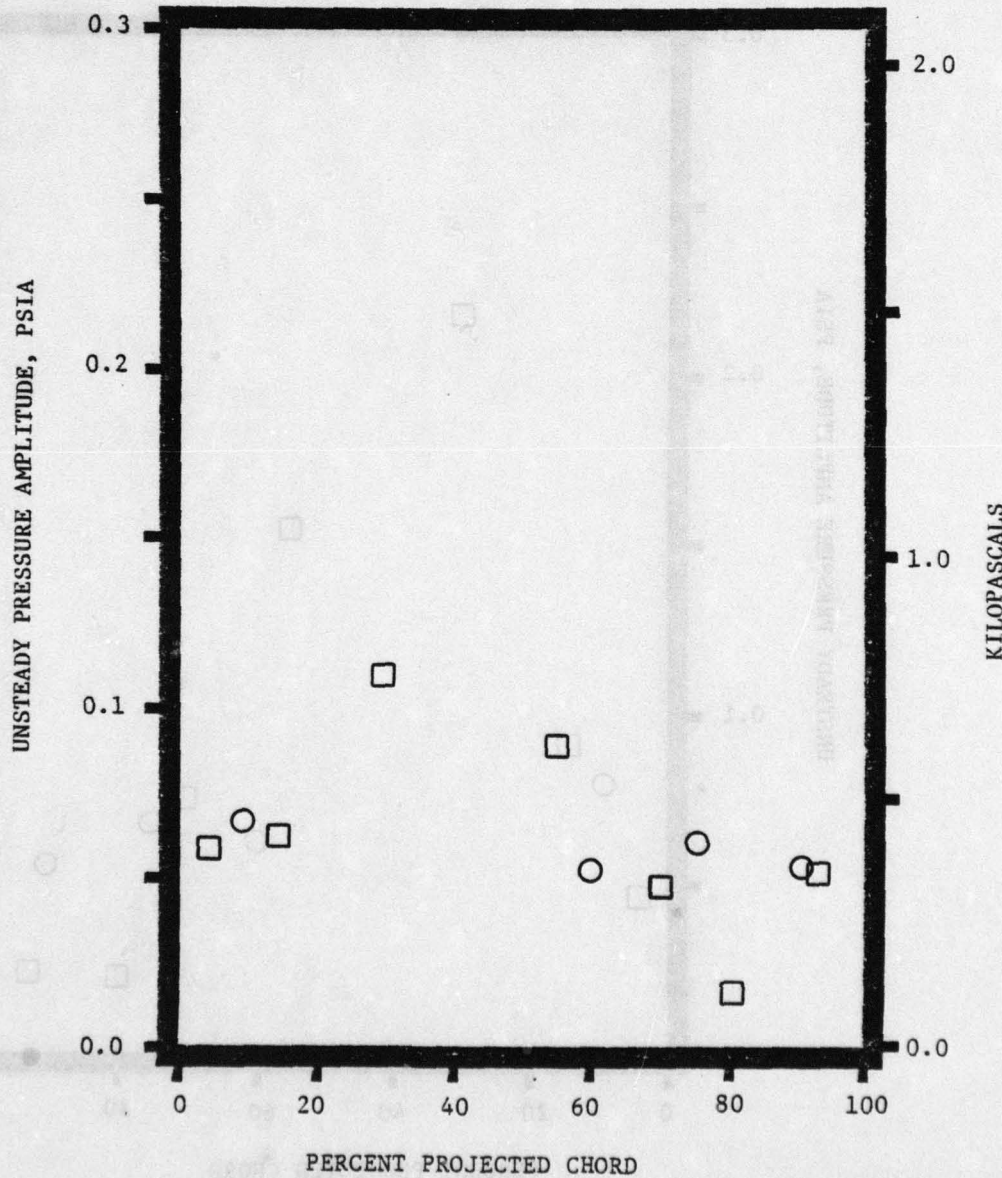
TORSION CASCADE  
SURFACE PRESSURE AMPLITUDES  
2.3 TOTAL TO STATIC EXPANSION RATIO  
-90° INTERBLADE PHASE ANGLE  
○ PRESSURE SURFACE  
□ SUCTION SURFACE



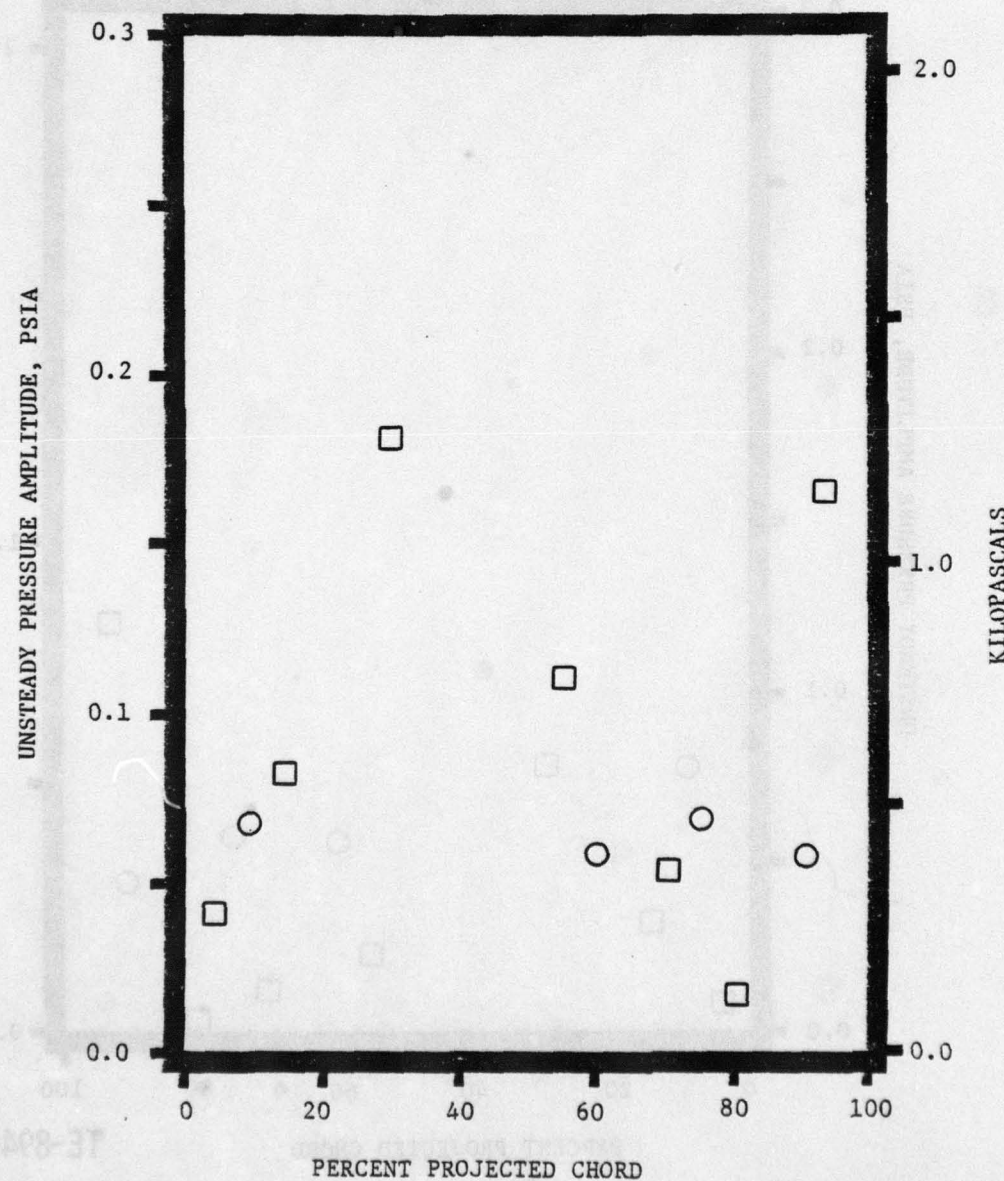
TORSION CASCADE  
SURFACE PRESSURE AMPLITUDES  
2.3 TOTAL TO STATIC EXPANSION RATIO  
180° INTERBLADE PHASE ANGLE  
○ PRESSURE SURFACE  
□ SUCTION SURFACE



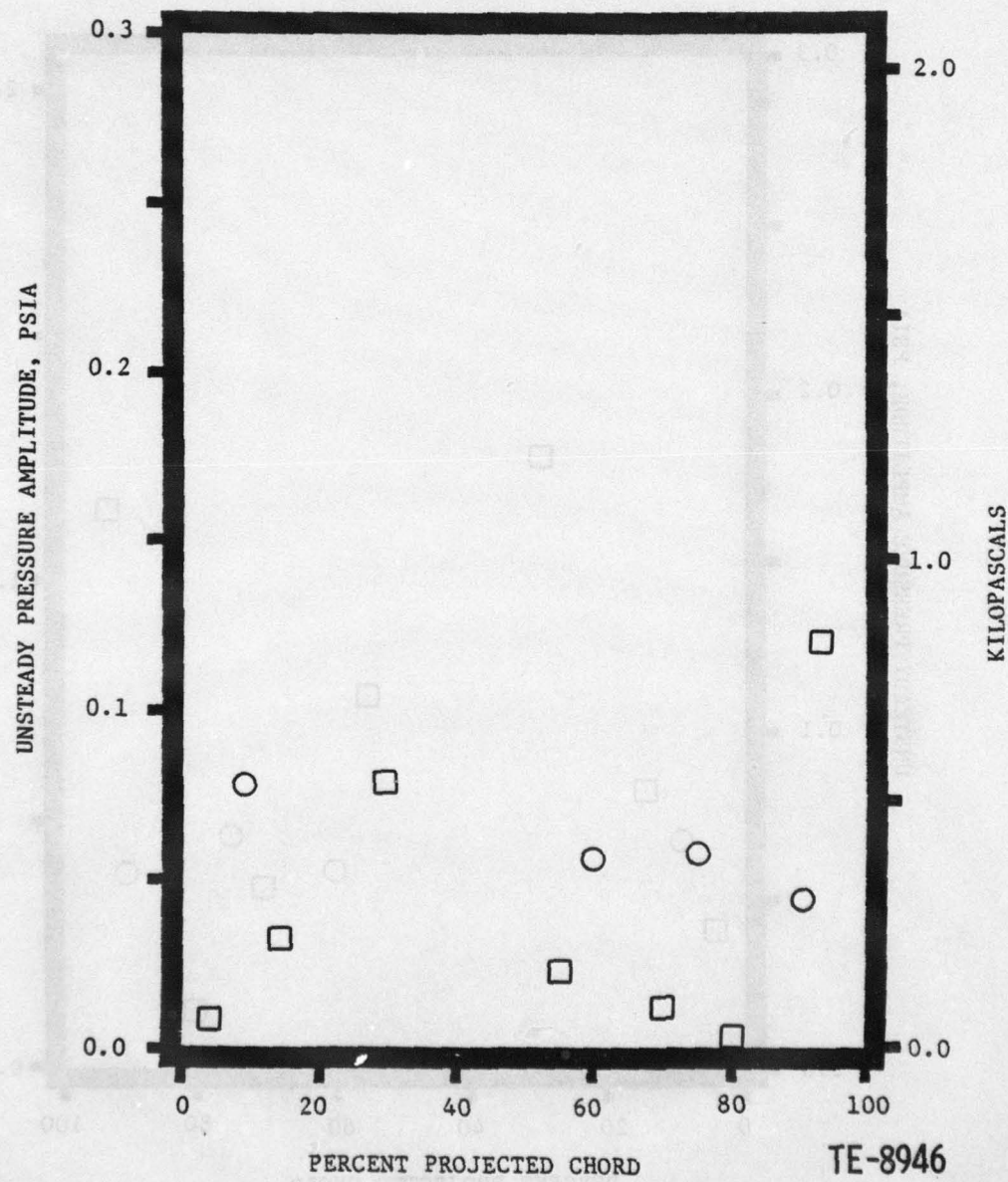
TORSION CASCADE  
SURFACE PRESSURE AMPLITUDES  
2.8 TOTAL TO STATIC EXPANSION RATIO  
 $+90^\circ$  INTERBLADE PHASE ANGLE  
○ PRESSURE SURFACE  
□ SUCTION SURFACE



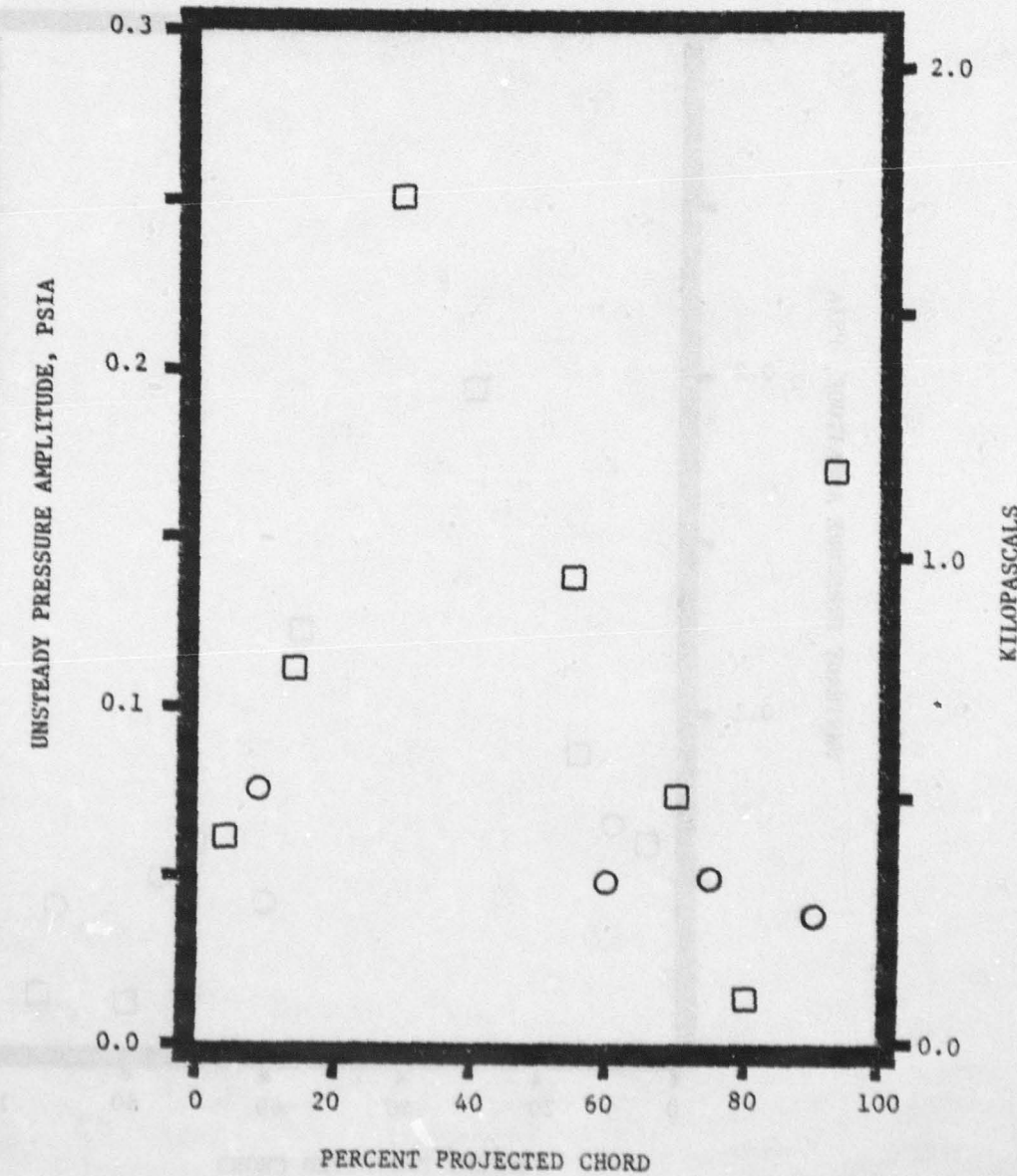
TORSION CASCADE  
SURFACE PRESSURE AMPLITUDES  
2.8 TOTAL TO STATIC EXPANSION RATIO  
 $+45^\circ$  INTERBLADE PHASE ANGLE  
○ PRESSURE SURFACE  
□ SUCTION SURFACE



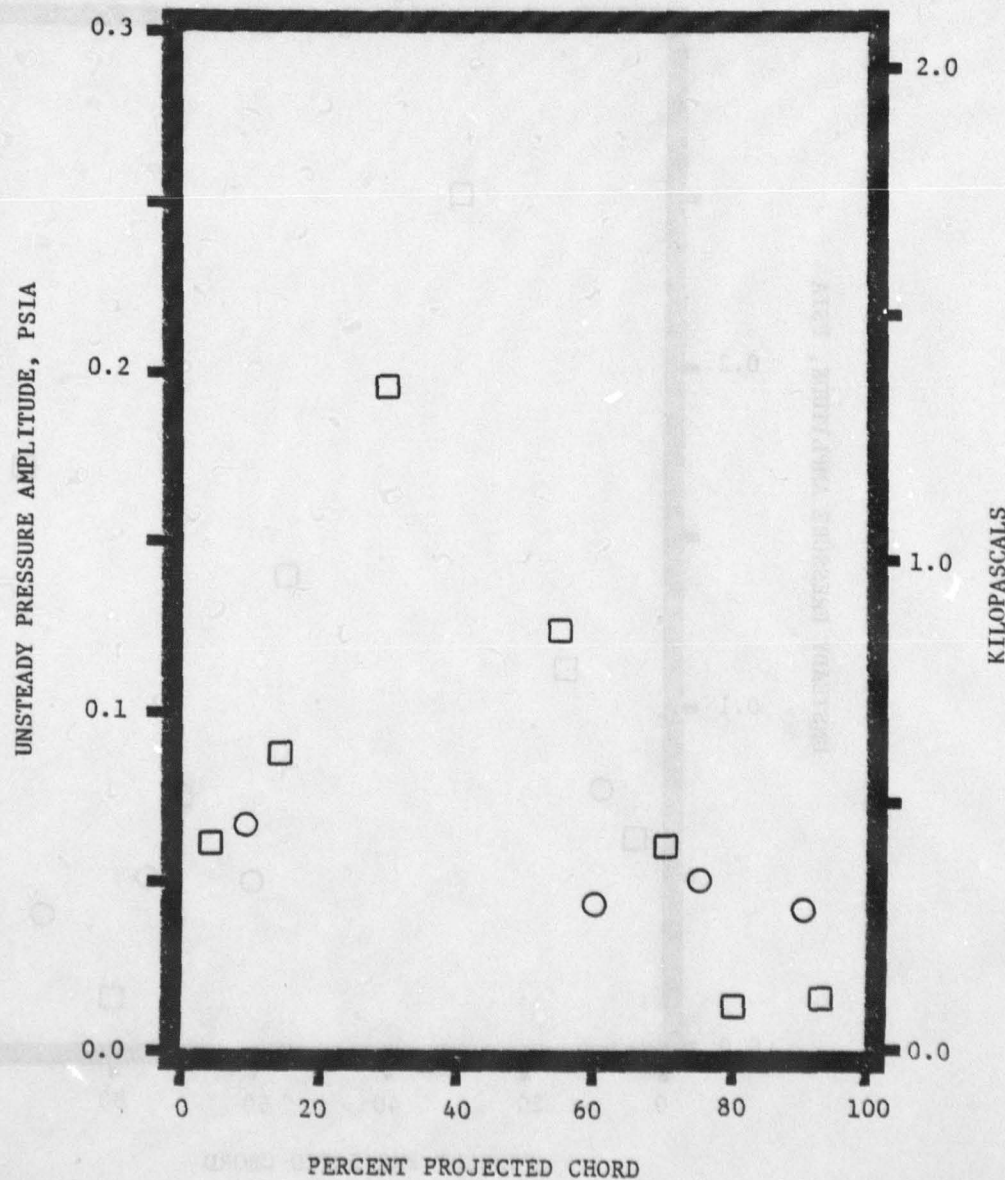
TORSION CASCADE  
SURFACE PRESSURE AMPLITUDES  
2.8 TOTAL TO STATIC EXPANSION RATIO  
0° INTERBLADE PHASE ANGLE  
○ PRESSURE SURFACE  
□ SUCTION SURFACE



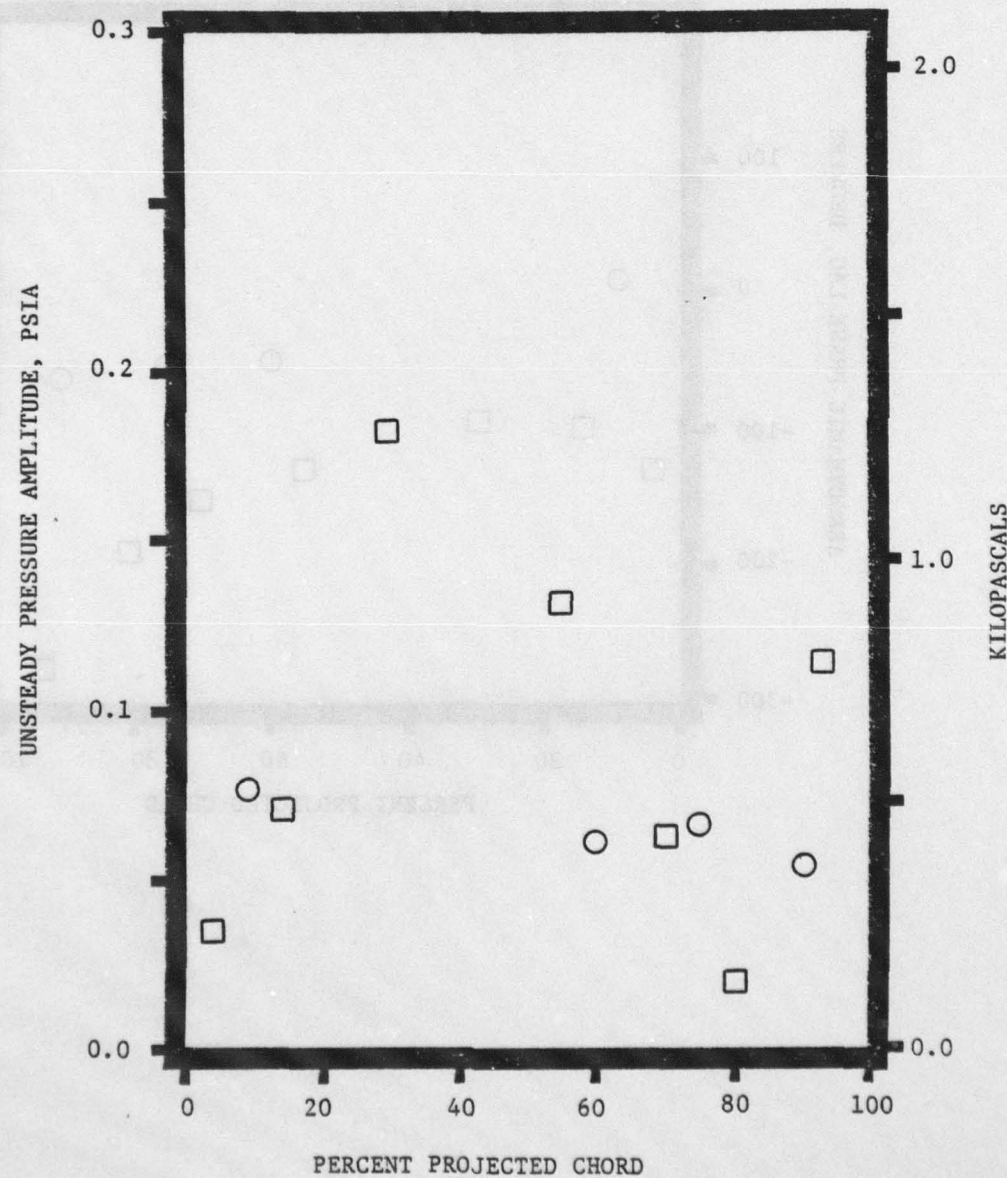
TORSION CASCADE  
SURFACE PRESSURE AMPLITUDES  
2.8 TOTAL TO STATIC EXPANSION RATIO  
-45° INTERBLADE PHASE ANGLE  
○ PRESSURE SURFACE  
□ SUCTION SURFACE



TORSION CASCADE  
SURFACE PRESSURE AMPLITUDES  
2.8 TOTAL TO STATIC EXPANSION RATIO  
-90° INTERBLADE PHASE ANGLE  
○ PRESSURE SURFACE  
□ SUCTION SURFACE



STAGE 2 TORSION CASCADE  
SURFACE PRESSURE AMPLITUDES  
2.8 TOTAL TO STATIC EXPANSION RATIO  
180° INTERBLADE PHASE ANGLE  
○ PRESSURE SURFACE  
□ SUCTION SURFACE

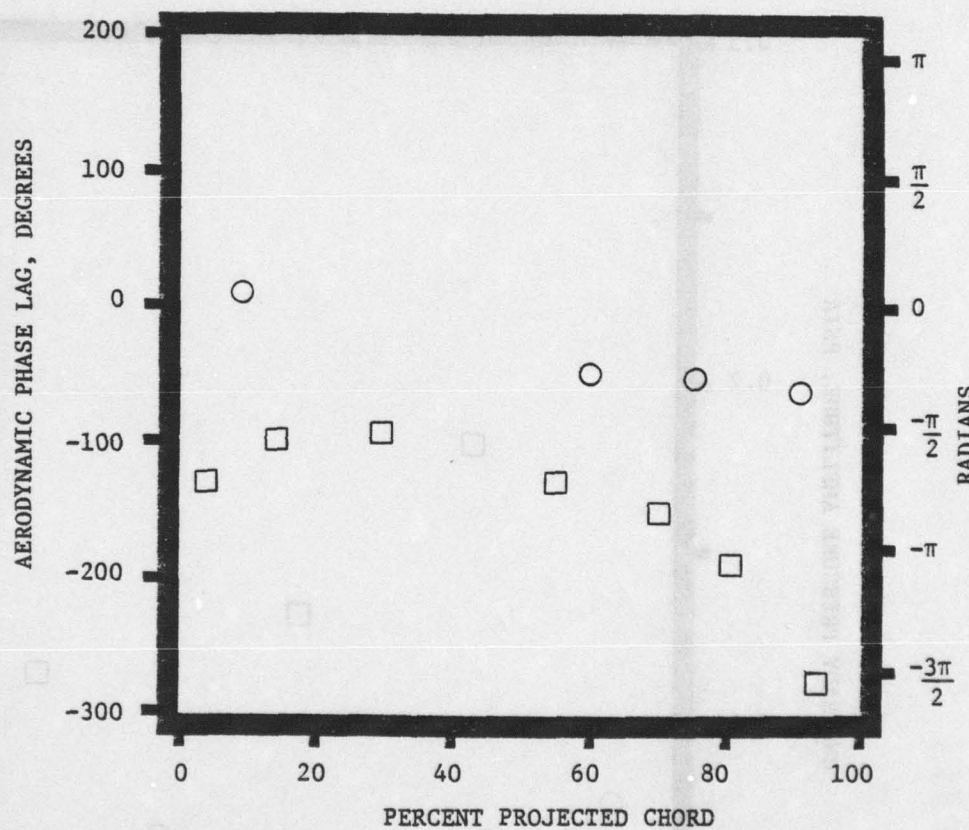


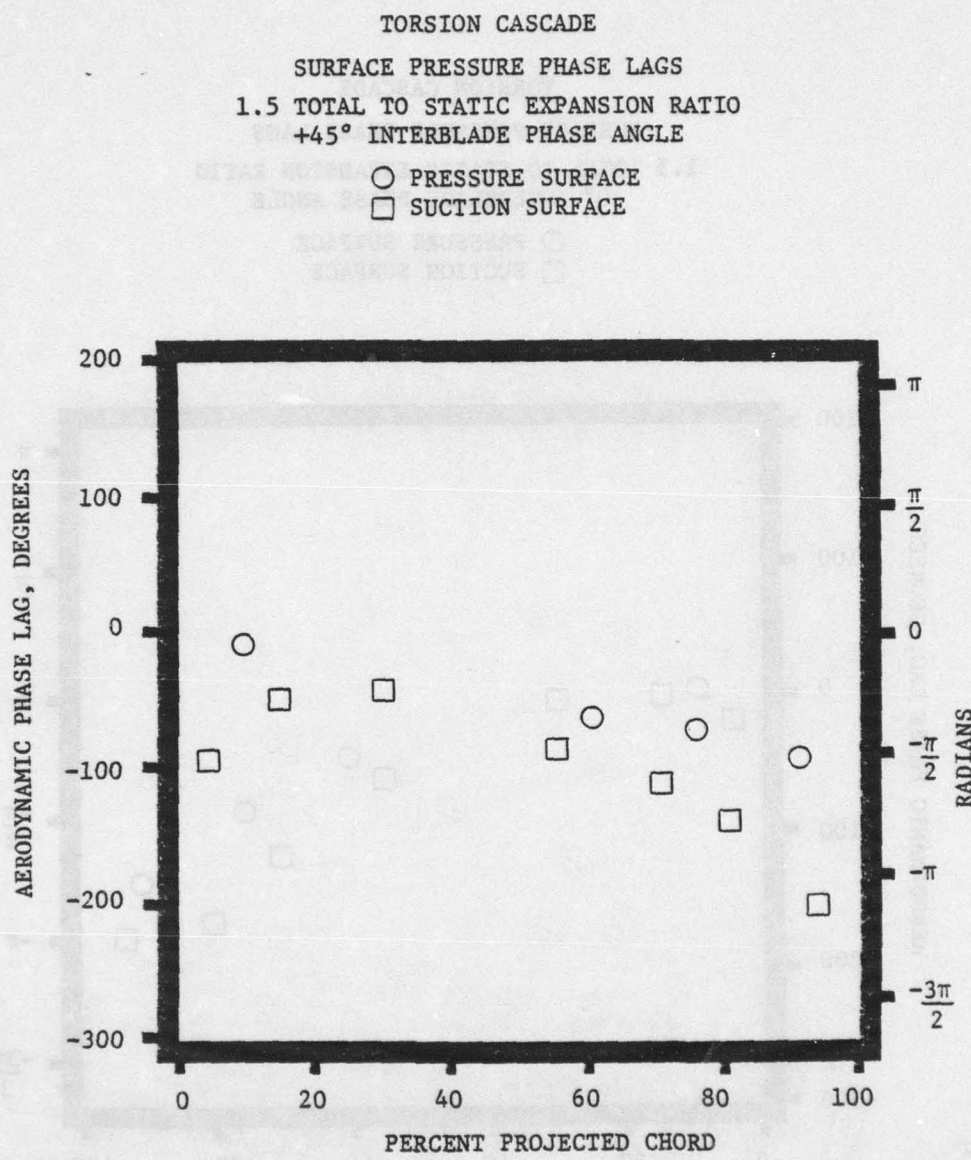
TORSION CASCADE

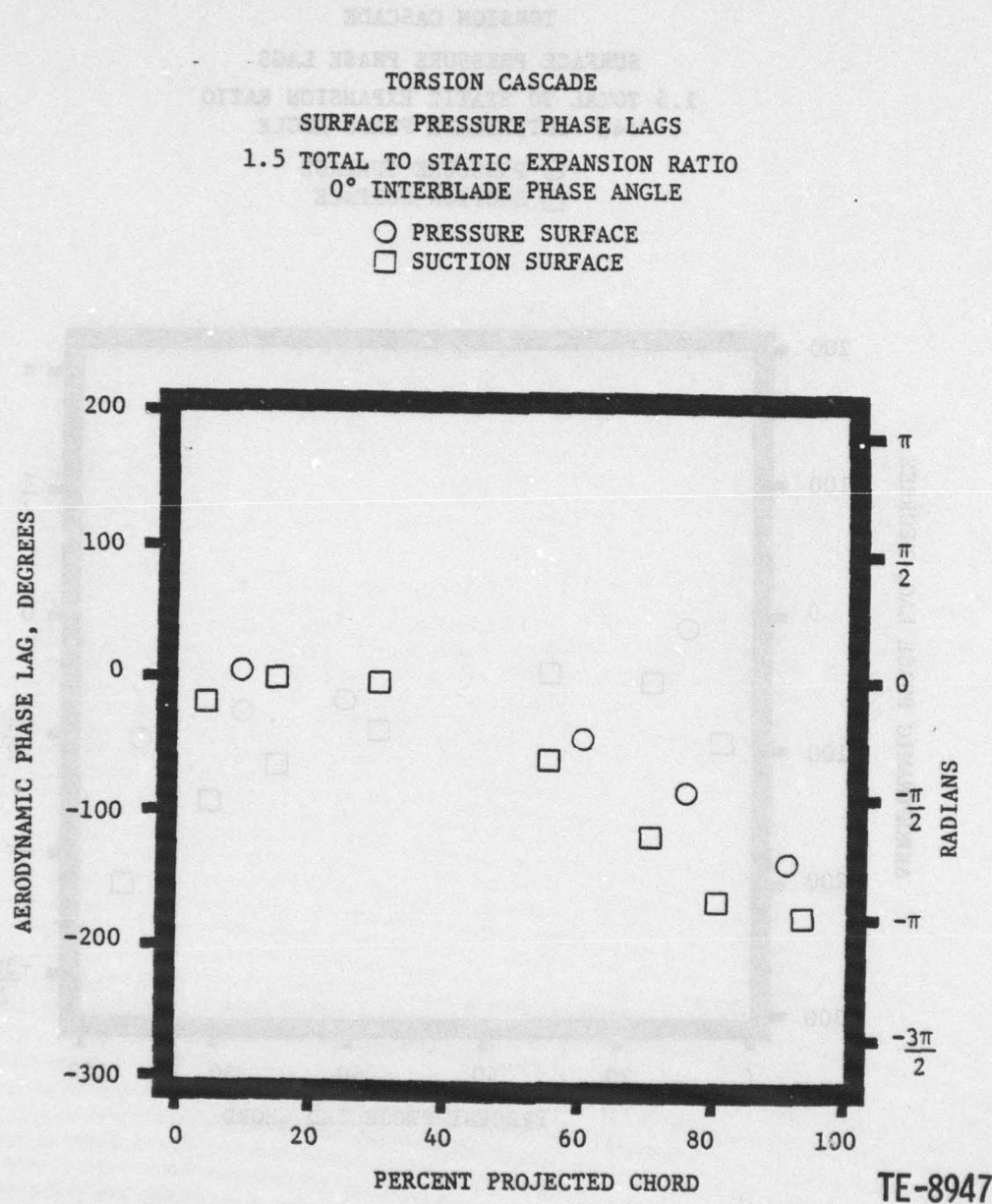
SURFACE PRESSURE PHASE LAGS

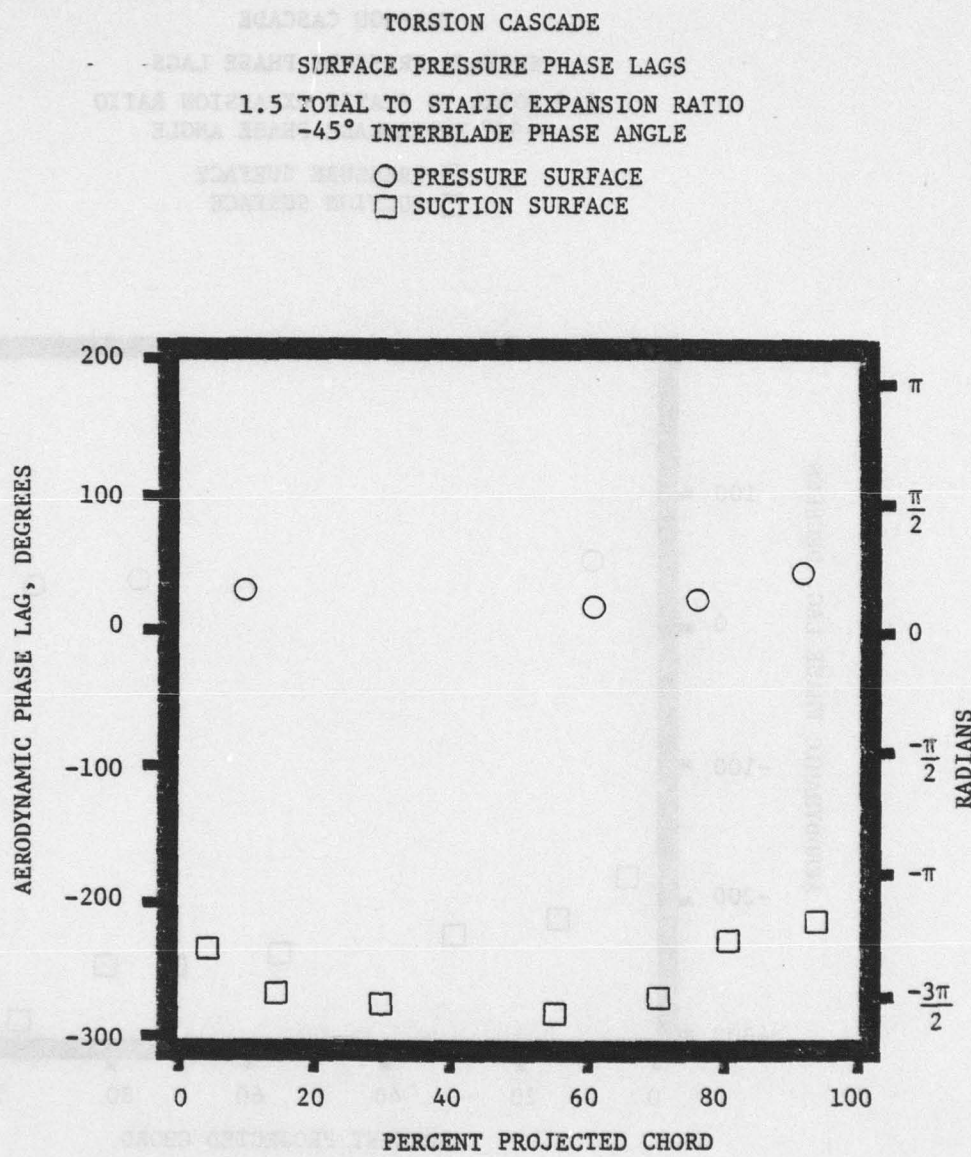
1.5 TOTAL TO STATIC EXPANSION RATIO  
 $+90^\circ$  INTERBLADE PHASE ANGLE

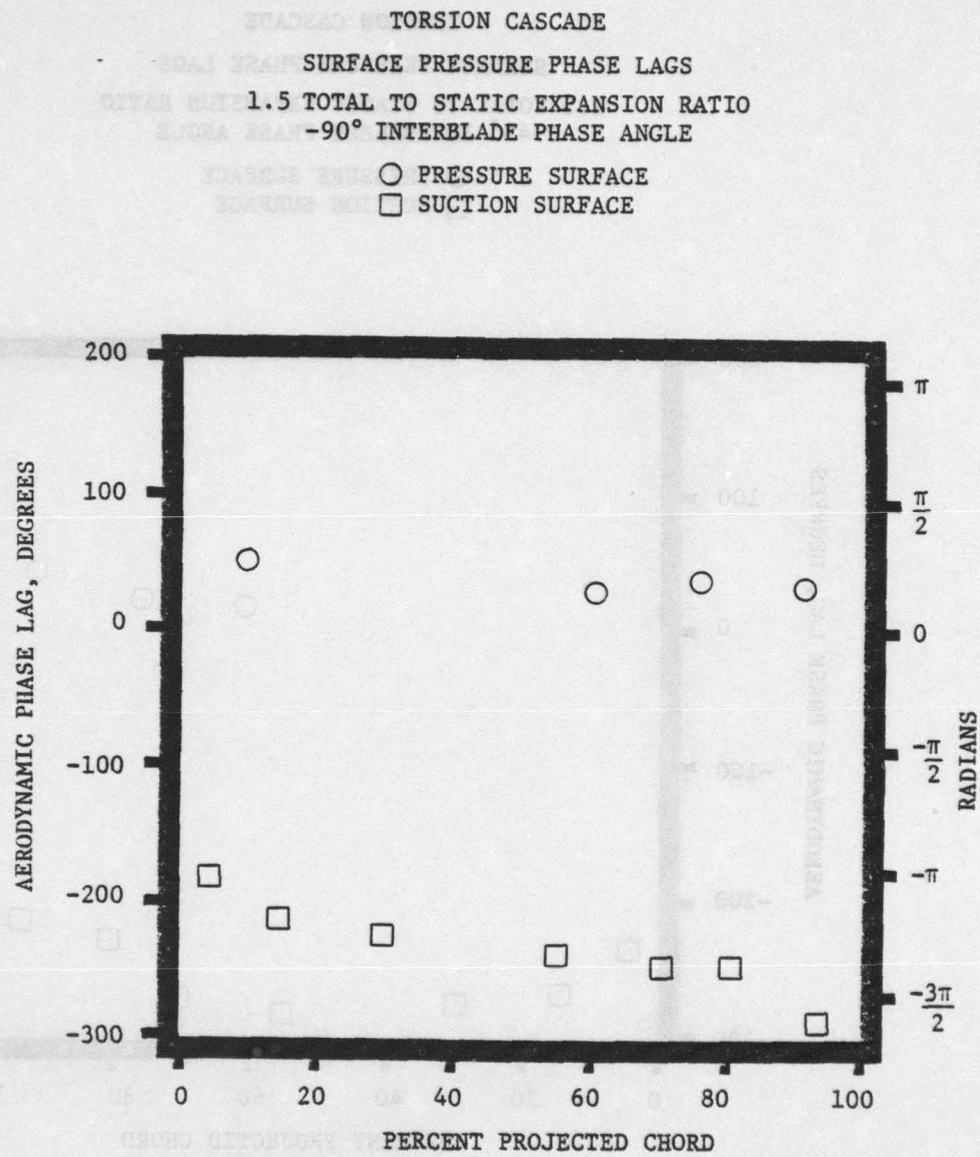
○ PRESSURE SURFACE  
□ SUCTION SURFACE

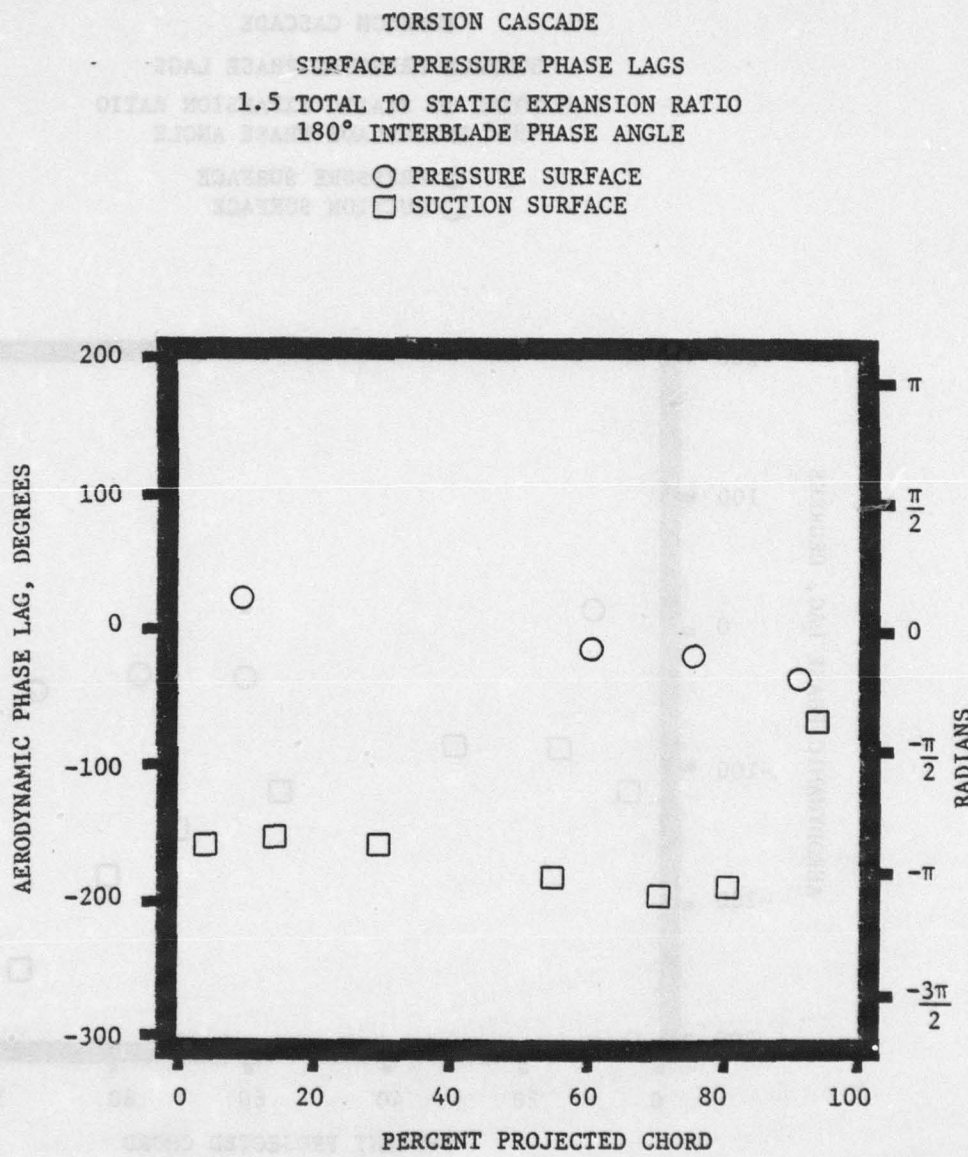




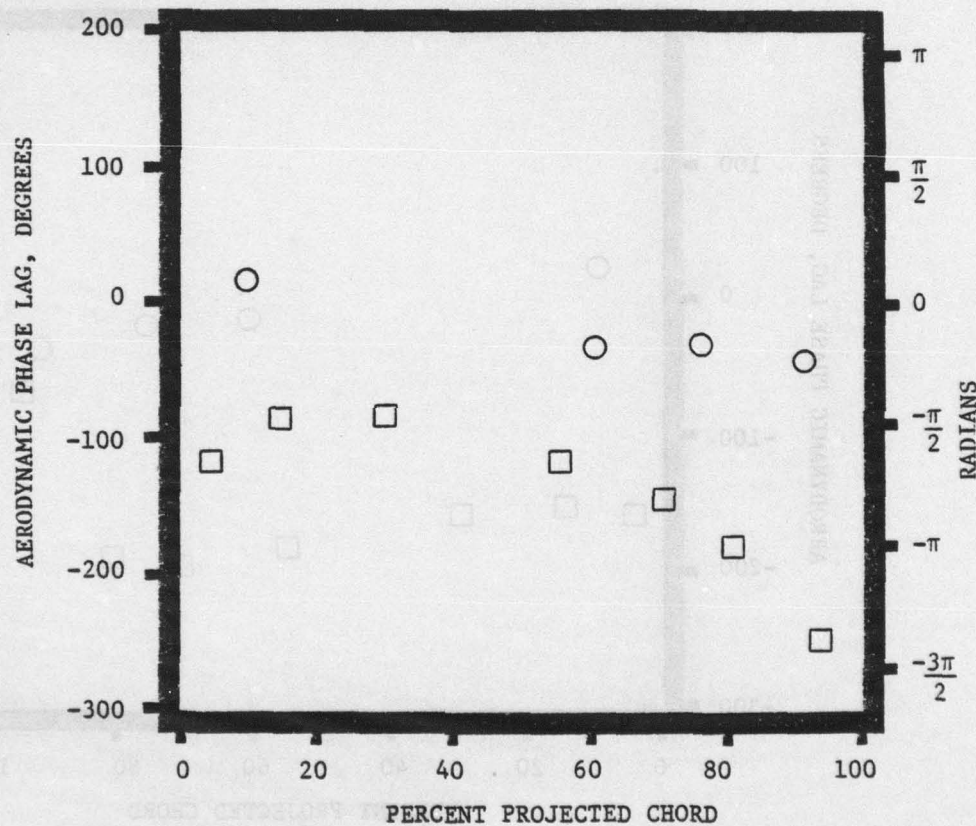


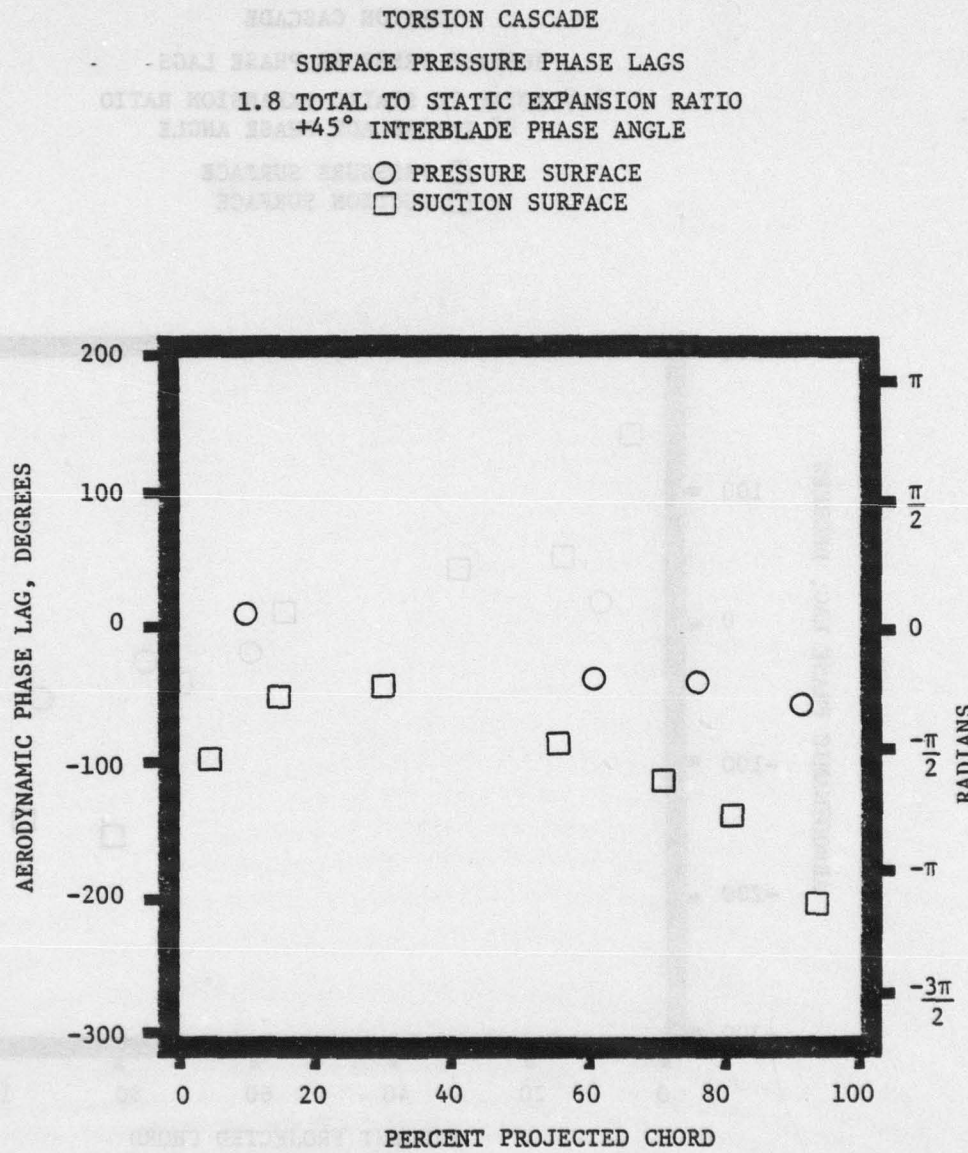


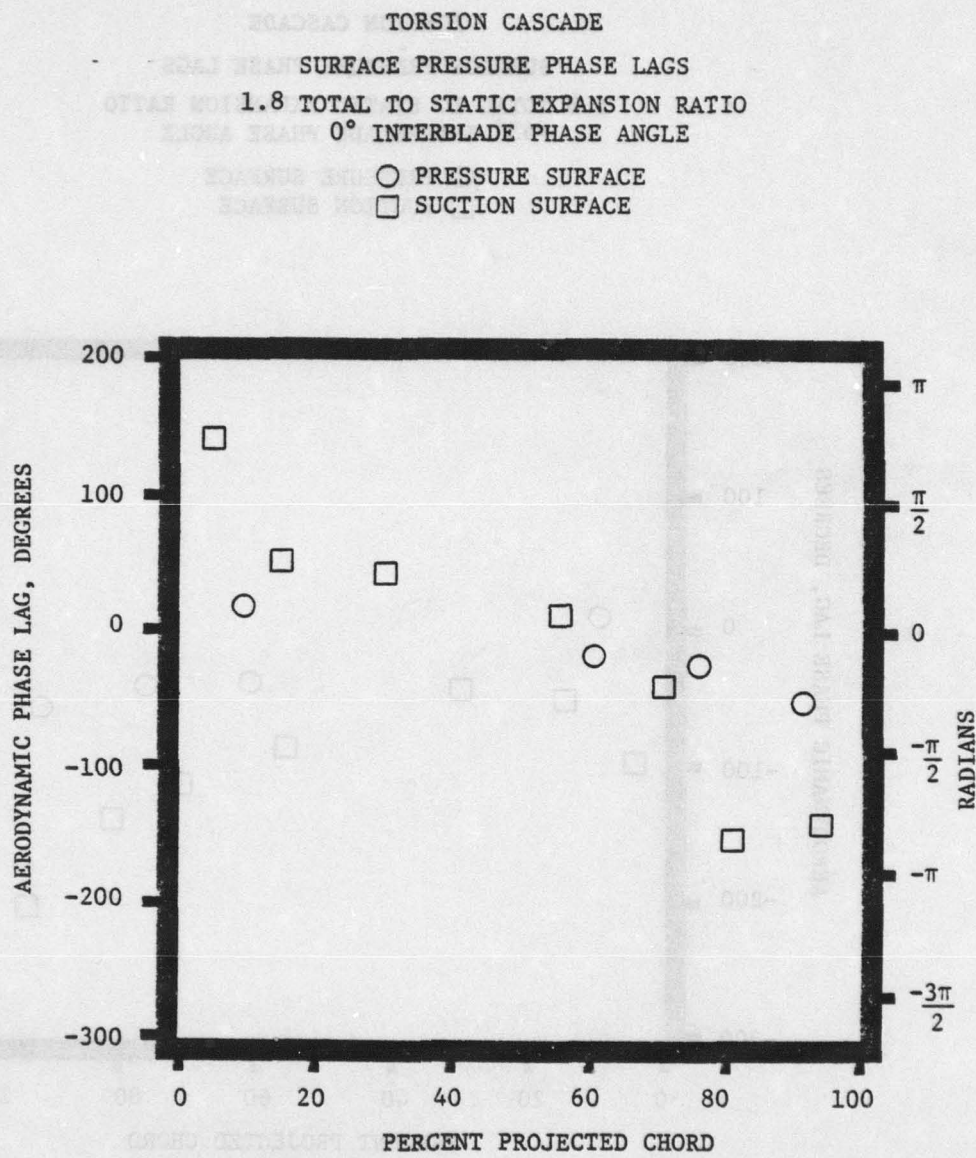


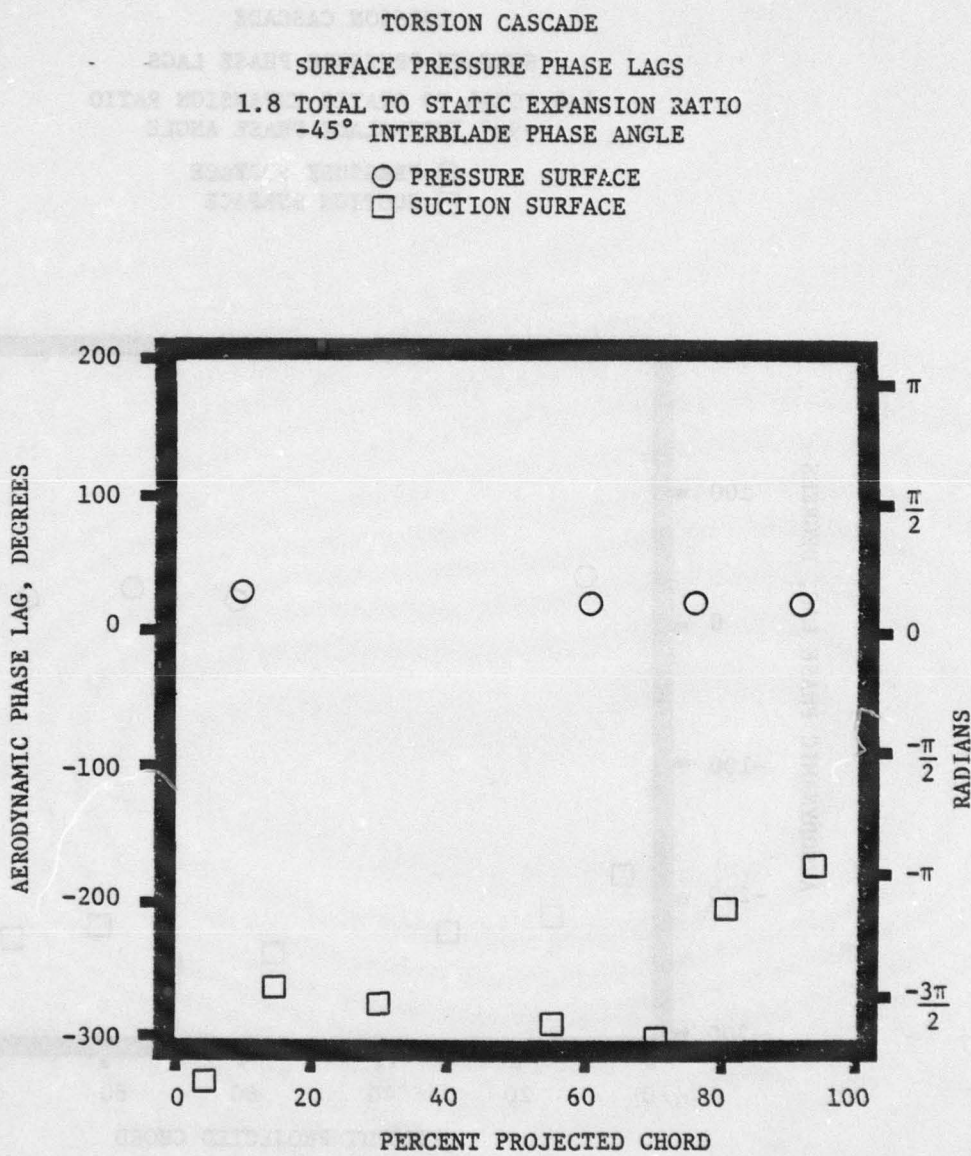


TORSION CASCADE  
SURFACE PRESSURE PHASE LAGS  
1.8 TOTAL TO STATIC EXPANSION RATIO  
 $+90^\circ$  INTERBLADE PHASE ANGLE  
○ PRESSURE SURFACE  
□ SUCTION SURFACE









ROADMAP TO TORSION CASCADE

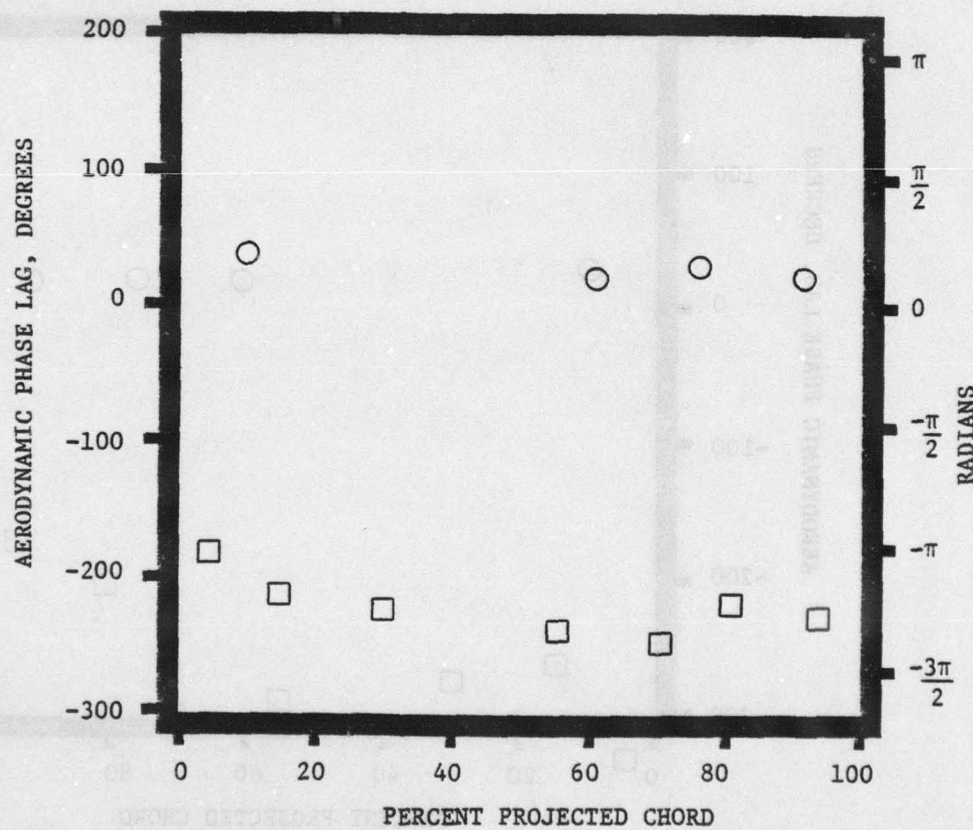
SURFACE PRESSURE PHASE LAGS

1.8 TOTAL TO STATIC EXPANSION RATIO

-90° INTERBLADE PHASE ANGLE

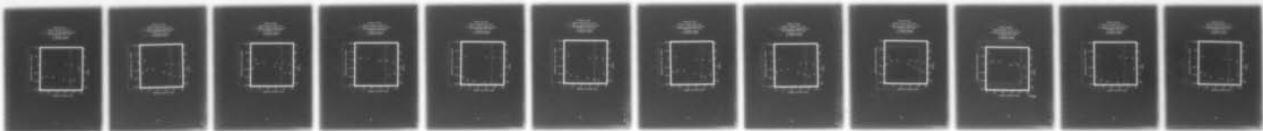
○ PRESSURE SURFACE

□ SUCTION SURFACE

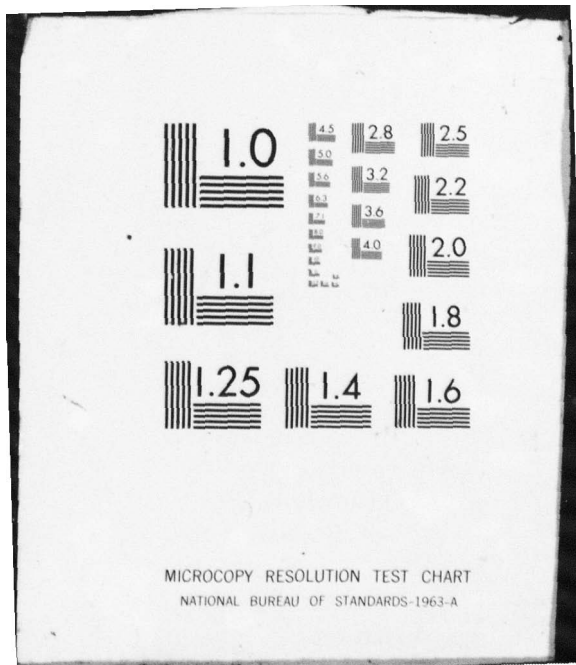


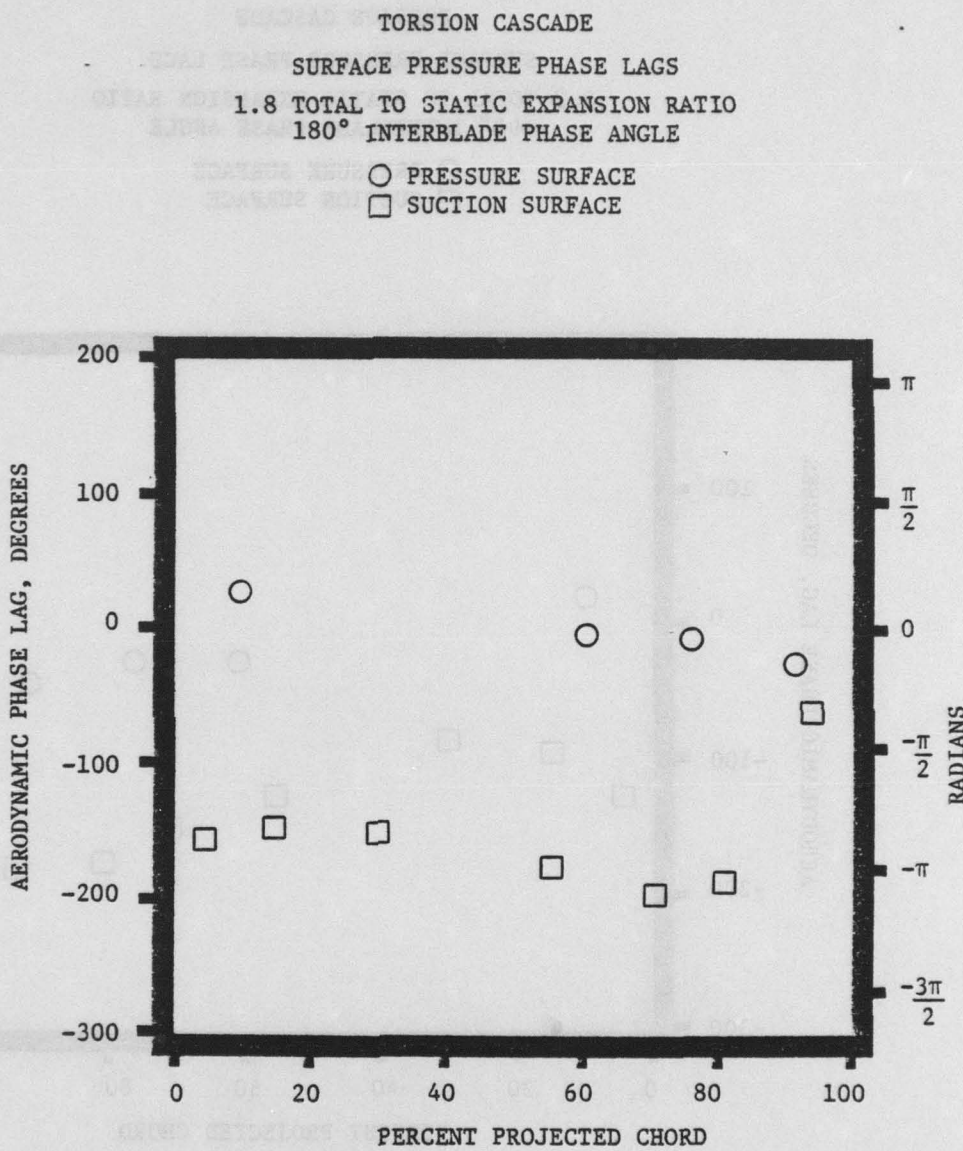
AD-A083 766 GENERAL MOTORS CORP INDIANAPOLIS IN DETROIT DIESEL A--ETC F/G 20/4  
TIME-VARIANT AERODYNAMICS FOR TORSIONAL MOTION OF LARGE-TURNING--ETC(U)  
JAN 80 R L JAY, M D ROTHROCK, R E RIFFEL N00019-79-C-0087  
UNCLASSIFIED DDA-EDR-10192 NL

2 OF 2  
AD  
A083766



END  
DATE  
FILED  
6-80  
DTIC



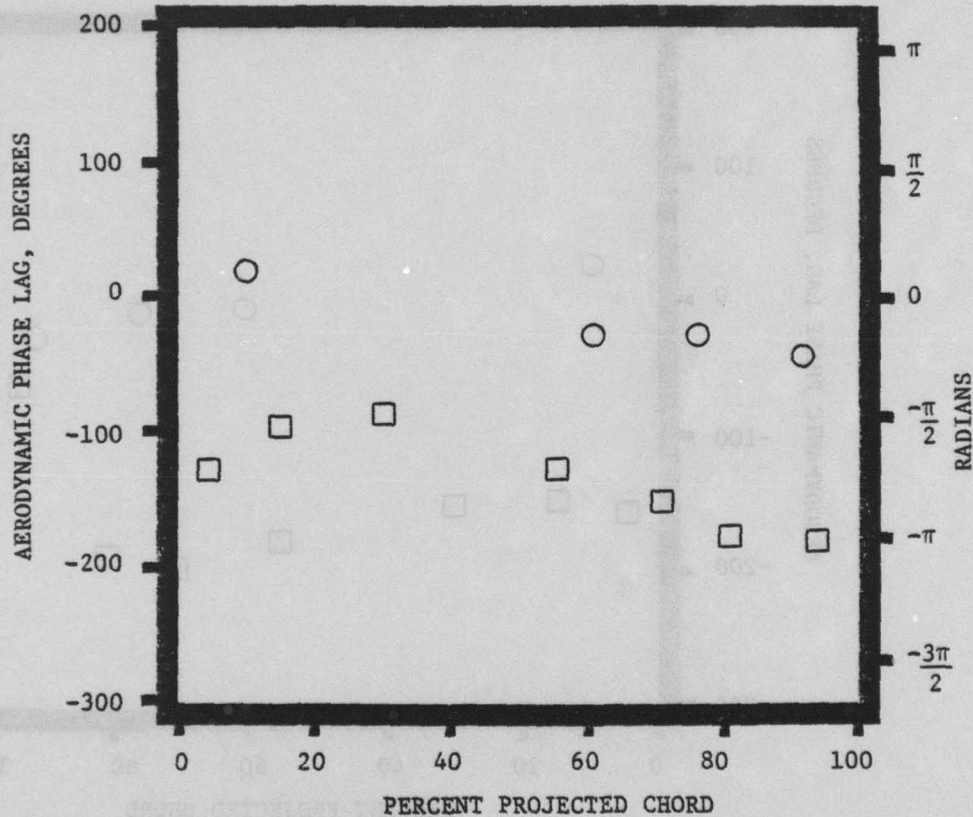


TORSION CASCADE

SURFACE PRESSURE PHASE LAGS

2.3 TOTAL TO STATIC EXPANSION RATIO  
+90° INTERBLADE PHASE ANGLE

○ PRESSURE SURFACE  
□ SUCTION SURFACE

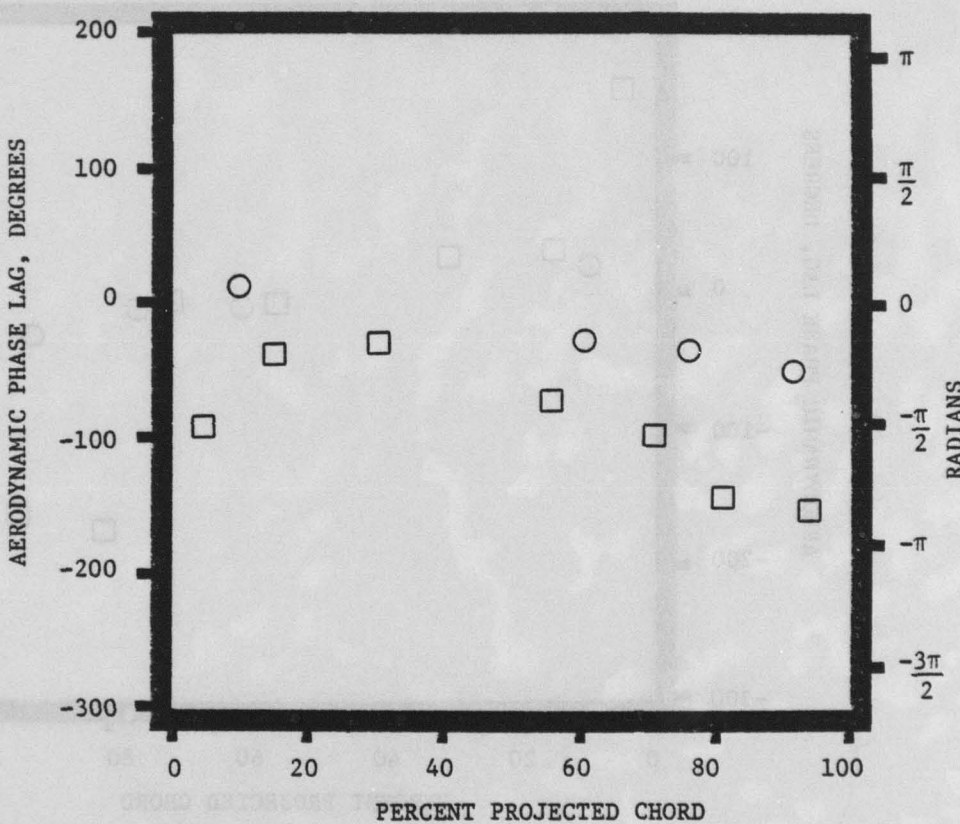


TORSION CASCADE

SURFACE PRESSURE PHASE LAGS

2.3 TOTAL TO STATIC EXPANSION RATIO  
 $+45^\circ$  INTERBLADE PHASE ANGLE

○ PRESSURE SURFACE  
□ SUCTION SURFACE

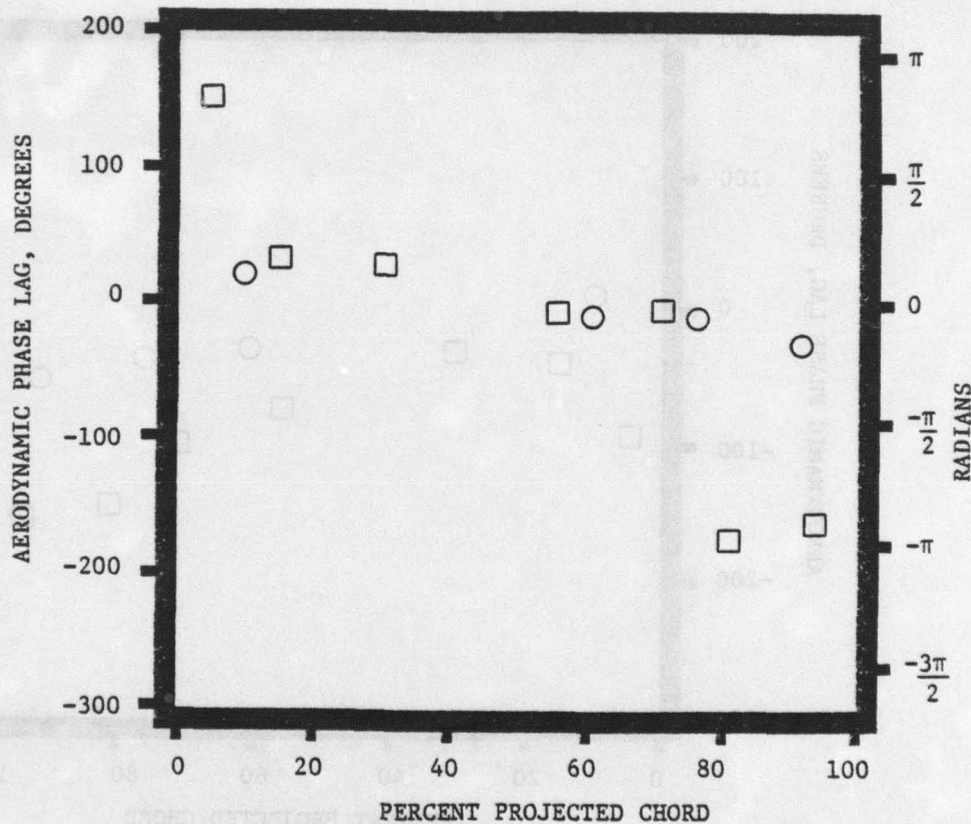


TORSION CASCADE

SURFACE PRESSURE PHASE LAGS

2.3 TOTAL TO STATIC EXPANSION RATIO  
0° INTERBLADE PHASE ANGLE

○ PRESSURE SURFACE  
□ SUCTION SURFACE



TORSION CASCADE

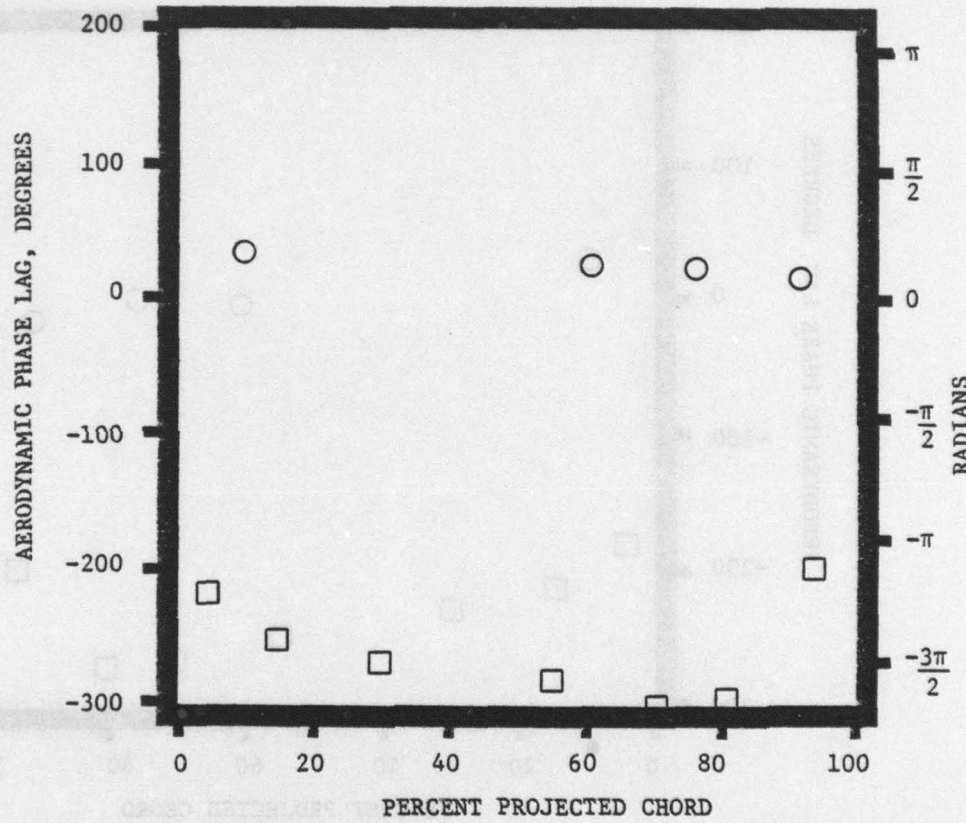
SURFACE PRESSURE PHASE LAGS

2.3 TOTAL TO STATIC EXPANSION RATIO

-45° INTERBLADE PHASE ANGLE

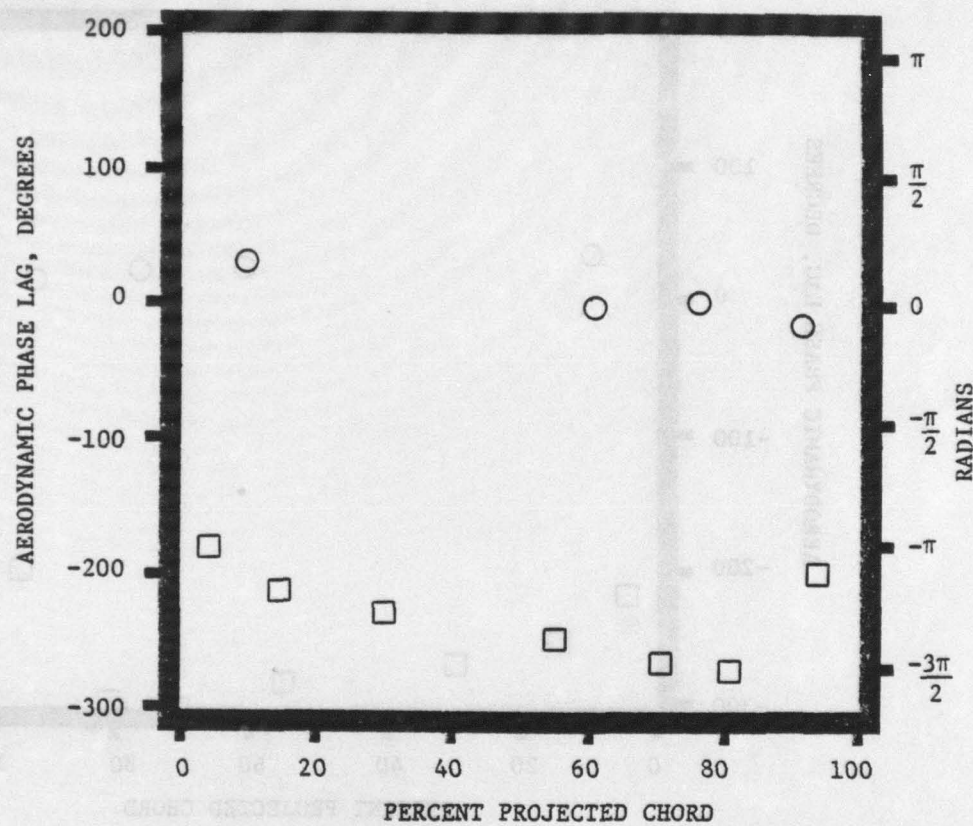
○ PRESSURE SURFACE

□ SUCTION SURFACE

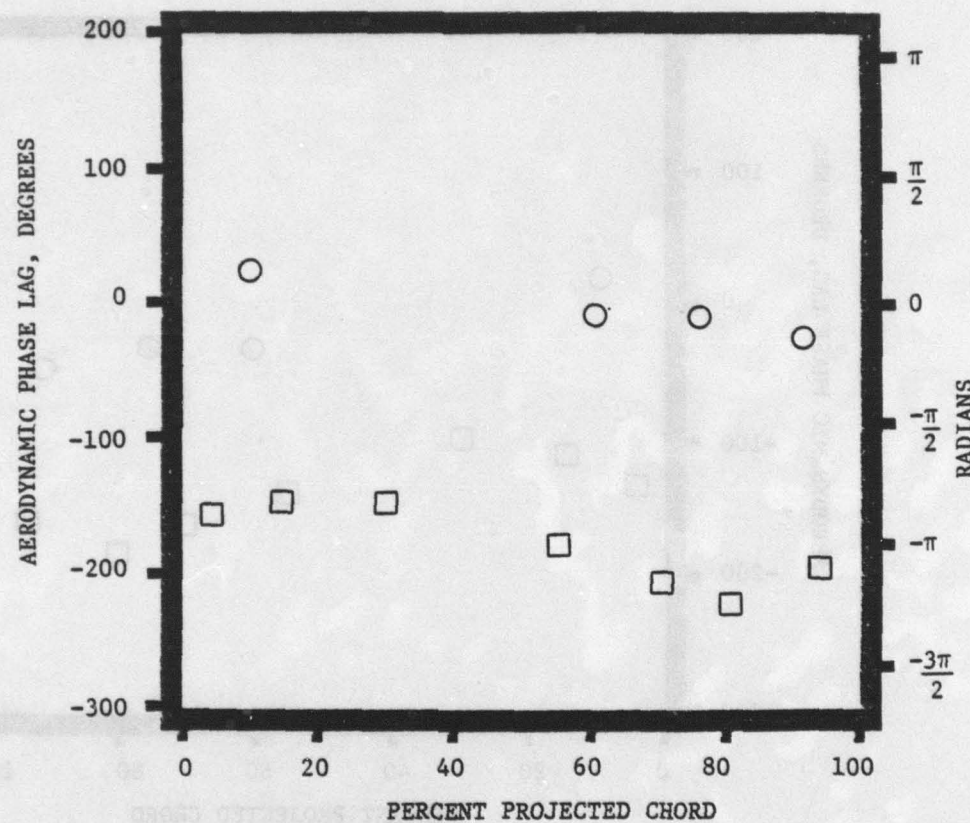


2.3 TOTAL TO STATIC EXPANSION RATIO  
-90° INTERBLADE PHASE ANGLE

○ PRESSURE SURFACE  
□ SUCTION SURFACE

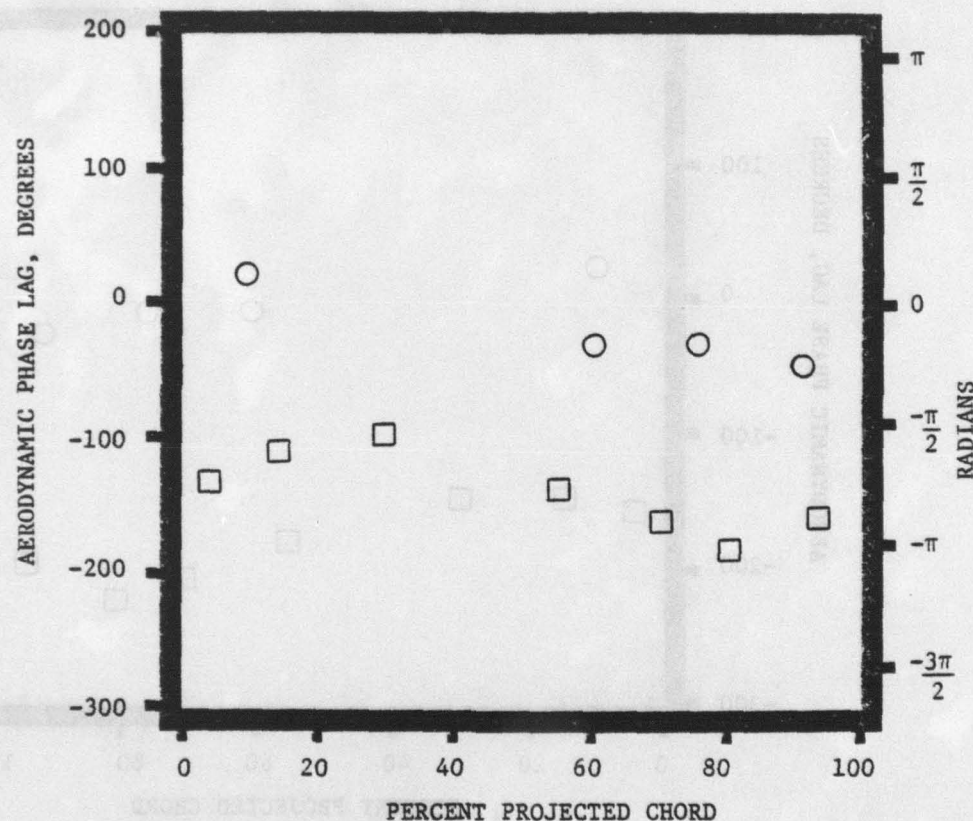


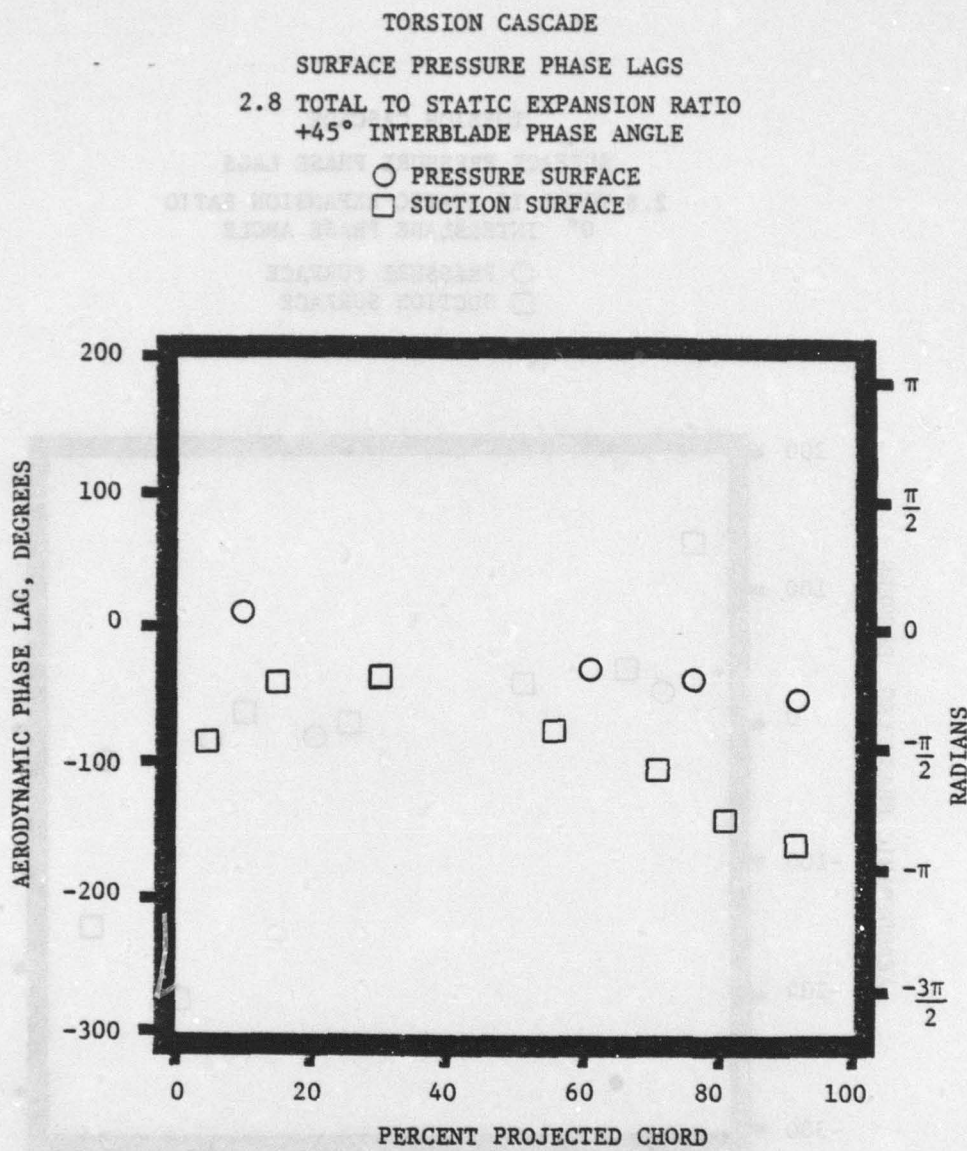
REYNOLDS NUMBER TORSION CASCADE  
SURFACE PRESSURE PHASE LAGS  
2.3 TOTAL TO STATIC EXPANSION RATIO  
180° INTERBLADE PHASE ANGLE  
○ PRESSURE SURFACE  
□ SUCTION SURFACE

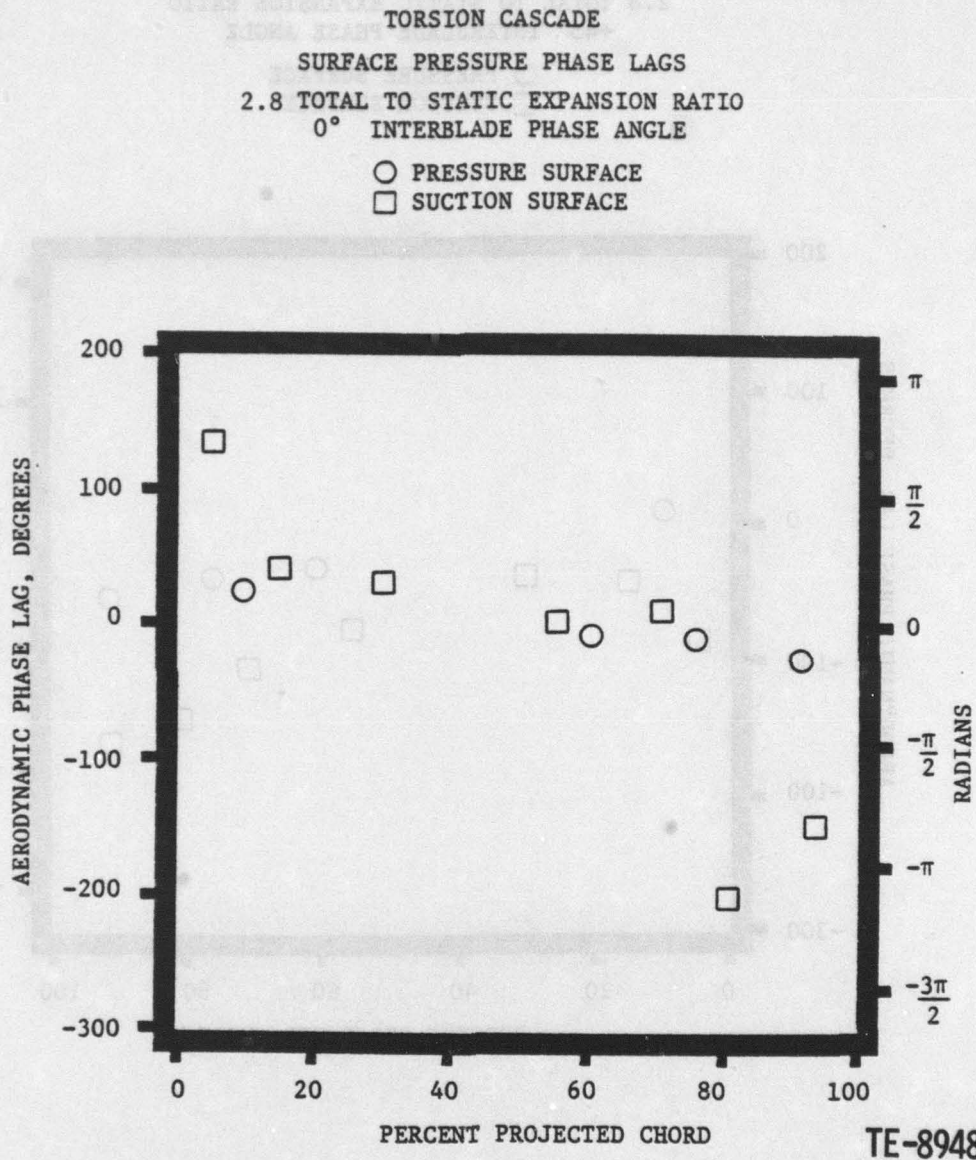


HEADMAN  
TORSION CASCADE  
SURFACE PRESSURE PHASE LAGS  
2.8 TOTAL TO STATIC EXPANSION RATIO  
+90° INTERBLADE PHASE ANGLE

○ PRESSURE SURFACE  
□ SUCTION SURFACE





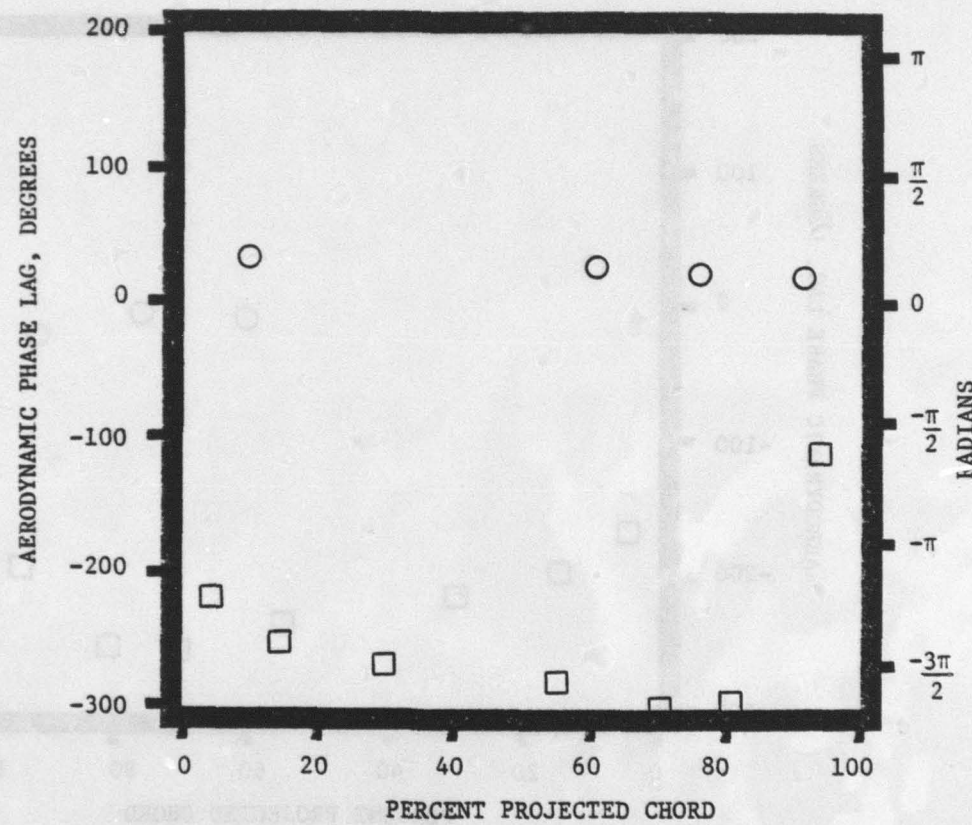


TORSION CASCADE

SURFACE PRESSURE PHASE LAGS

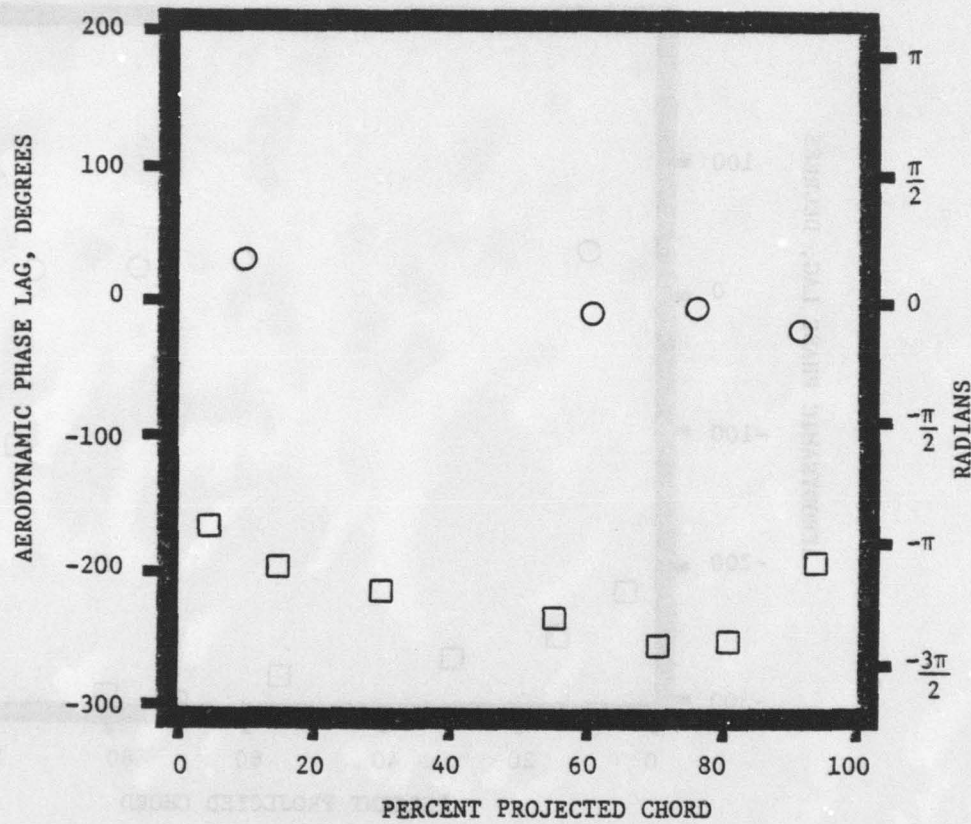
2.8 TOTAL TO STATIC EXPANSION RATIO  
 $-45^\circ$  INTERBLADE PHASE ANGLE

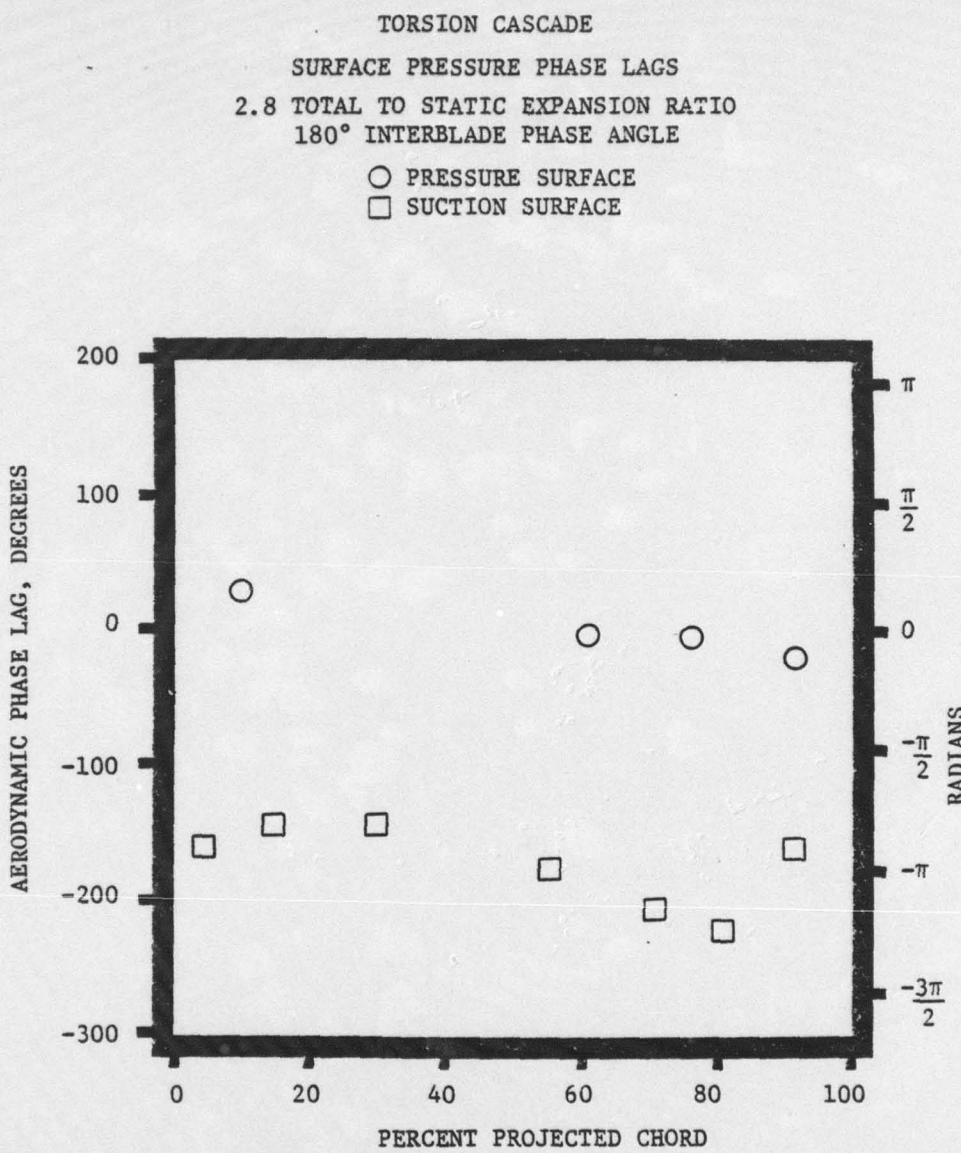
○ PRESSURE SURFACE  
□ SUCTION SURFACE



BLADED TORSION CASCADE  
SURFACE PRESSURE PHASE LAGS  
2.8 TOTAL TO STATIC EXPANSION RATIO  
-90° INTERBLADE PHASE ANGLE

○ PRESSURE SURFACE  
□ SUCTION SURFACE





**MED**  
**8**